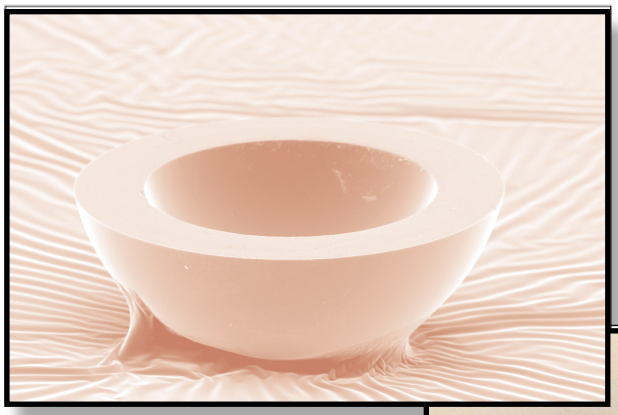

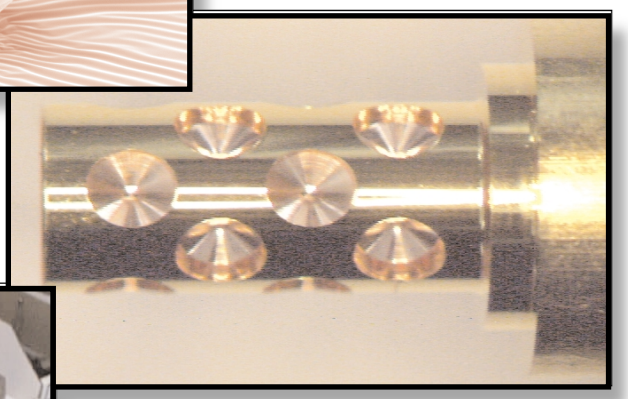

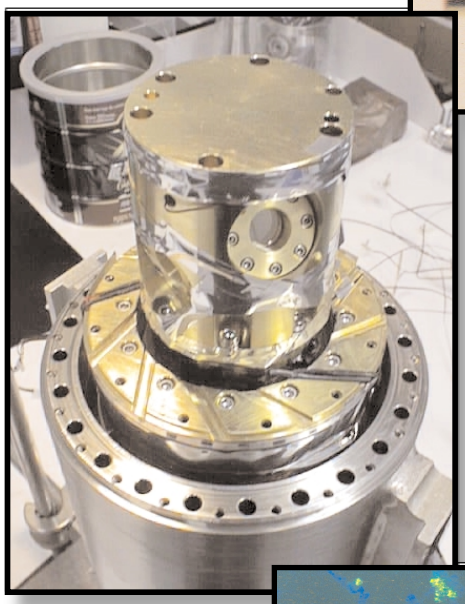

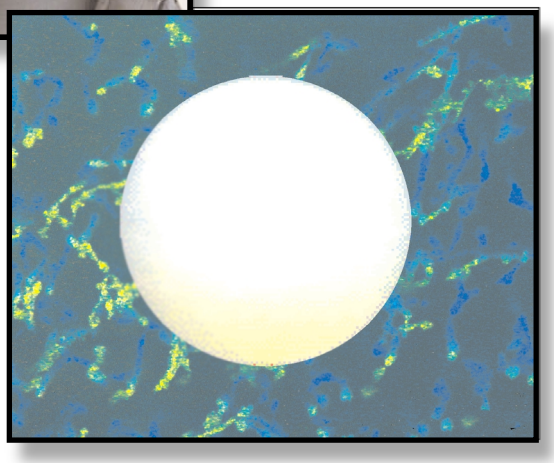

Inertial Confinement Fusion

ANNUAL REPORT

OCTOBER 1, 1998
THROUGH
SEPTEMBER 30, 1999

Schafer

GENERAL ATOMICS

THE FY99 TARGET FABRICATION AND TARGET TECHNOLOGY DEVELOPMENT TEAM

Dr. Kenneth Schultz
Program Manager

General Atomics
San Diego, California

Neil Alexander, Wes Baugh, Chandu Baxi, Chuck Beal, Gottfried Besenbruch, Karl Boline, Lloyd Brown, Erwin Castillo, Chuck Charman, Sharon Considine, Don Czechowicz, Vic Delbene, Fred Elsner, Chuck Gibson, Jane Gibson, Kett Gifford, Dan Goodin, Steve Grant, Annette Greenwood, Martin Hoppe, Dave Husband, Jim Kaae, Jim Kulchar, Barry McQuillan, Wayne Miller, Abbas Nikroo, Sally Paguio, Joe Pontelandolfo, Elmer Reis, John Ruppe, Chuck Schneidmuller, Clyde Shearer, John Sheliak, Joe Smith, Dave Steinman, Bob Stemke, Rich Stephens, John Vanderzanden, Don Wall, Jason Wall, David Woodhouse

Schafer Corporation
Livermore, California

Thom Bahrs, Don Bittner, Christina Bostick, John Burmann, Frank Carey, Sue Carter, Derek Coker, Pat Collins, Steve Dropinski, Illges Faron, Scott Faulk, Ying Lee, Chuck Hendricks, Ed Hsieh, Ephraim Hipolito, Earl Hodges, Lisa MacGregor, Derrick Mathews, Michael Monsler, Brian Motta, Ron Perea, Louis Rhodes, Craig Rivers, Jim Sater, Diana Schroen-Carey, Keith Shillito, Cheryl Spencer, Katie Strube, Alicia Thomas, Tom Walsh, Kelly Youngblood

ABSTRACT

General Atomics (GA) has served as the Inertial Confinement Fusion (ICF) Target Component Fabrication and Technology Development Support contractor for the U.S. Department of Energy since December 30, 1990. This report documents the technical activities of the period October 1, 1998 through September 30, 1999.

During this period, GA and our partner Schafer Corporation were assigned 17 formal tasks in support of the ICF program and its five laboratories. A portion of the effort on these tasks included providing direct "Onsite Support" at Lawrence Livermore National Laboratory (LLNL), Los Alamos National Laboratory (LANL), and Sandia National Laboratory (SNL). We fabricated and delivered over 1790 hohlraum mandrels and numerous other micromachined components to LLNL, LANL, and SNL. We produced more than 1380 glass and plastic target capsules over a wide range of sizes and designs (plus over 300 near target-quality capsules) for LLNL, LANL, SNL, and University of Rochester/Laboratory for Laser Energetics (UR/LLE). We also delivered various target foils and films for Naval Research Lab (NRL) and UR/LLE in FY99. We fabricated a device to polish NIF-sized beryllium shells and prepared a laboratory for the safe operation of beryllium polishing activities. This report describes these target fabrication activities and the target fabrication and characterization development activities that made the deliveries possible.

During FY99, the GA/Schafer portion of the GA/Schafer-UR/LLE-LANL team effort for design, procurement, installation, and testing of the OMEGA Cryogenic Target System (OCTS) that will field cryogenic targets on OMEGA was completed. All components of the OCTS were procured, fabricated, assembled, tested, and shipped to UR/LLE. Only minor documentation tasks remain to be done in FY00.

The ICF program is anticipating experiments at the OMEGA laser and the National Ignition Facility (NIF) which will require targets containing cryogenic layered D_2 or deuterium-tritium (DT) fuel. We are part of the National Cryogenic Target Program and support experiments at LLNL and LANL to generate and characterize cryogenic layers for these targets. We also contributed cryogenic engineering support and developed concepts for NIF cryogenic targets. This report summarizes and documents the technical progress made on these tasks.

ACRONYMS

AFM	atomic force microscope
Al	aluminum
AR	antireflection
CL	chain locker
CPL	cryogenic pressure loader
CTM	cryogenic target mount
CTPS	cryogenic target positioning system
Cu	copper
D_2TS	deuterium test system
DT	deuterium-tritium
EDM	electrical discharge machining
EOS	equation of state
Fe	iron
FTS	fill/transfer station
GDP	glow discharge polymer
GA	General Atomics
HDP	higher deposition pressures
HEPA	high efficiency particulates air (filter)
ICF	Inertial Confinement Fusion
i.d.	inner diameter
IR	infrared
LANL	Los Alamos National Laboratory
LEH	laser entrance hole
LDP	lower deposition pressures
LLNL	Lawrence Livermore National Laboratory
LP	lower pylon
MC	moving cryostat

MCTC	moving cryostat transport cart
NC	nonconcentricity
NCTS	NIF cryogenic target system
NIF	National Ignition Facility
NRL	Naval Research Laboratory
o.d.	outer diameter
OOR	out-of-round (difference in major and minor radius of a best fit ellipse)
OCTS	OMEGA Cryogenic Target System
ORNL	Oak Ridge National Laboratory
PAMS	poly(α-methylstyrene)
PCPR	permeation cell plug remover
PCSCS	permeation cell support and cooling system
PCHMS	permeation cell housing and motion system
P-V	peak to valley (amplitude)
PVA	poly(vinylalcohol)
RF	resorcinol-formaldehyde
SEM	scanning electron microscope
SiCH	silicon-doped polystyrene
Sn	tin
SNL	Sandia National Laboratory
ST	surrogate tank
TPX	commercial designation of the polymer produced by the polymerization of 1-methyl-4-pentene
TWA	time weighted average
UP	upper pylon
UR/LLE	University of Rochester/Laboratory for Laser Energetics
XRF	x-ray fluorescence

TABLE OF CONTENTS

LIST OF FIGURES

LIST OF TABLES

1. TARGET FABRICATION PROGRAM OVERVIEW

General Atomics (GA) has served as the Inertial Confinement Fusion (ICF) Target Component Fabrication and Technology Development Support contractor for the U.S. Department of Energy since December 30, 1990. This report documents the technical activities of the period October 1, 1998 through September 30, 1999. GA was assisted by Schafer Corporation and we have carried out the ICF Target Fabrication tasks as a fully integrated team effort.

During FY99, the GA/Schafer team was assigned 17 formal tasks as shown in Table 1–1. These tasks are described briefly here (Section 1). Additional technical detail on selected topics is given in Sections 2 through 6 of this report.

TABLE 1–1
FY99 TARGET FABRICATION TASKS

Task No.	Task Title Description	Total $K	Task Leader
LL01	On-Site Support for LLNL	598	Miller
LL02	Micromachined Target Components	1,401	Kaae
LL03	Composite Polymer Capsules for LLNL	505	Miller
LL04	NIF Target Development and Support	828[(a)]	Shillito/Alexander/Miller
LA01	On-Site Support for LANL	316	Miller
LA02	Composite Polymer Capsules for LANL	417	Miller
LA03	Beryllium Shell Support for LANL	100	Miller
NR01	NRL Target Deliveries	1,082	Walsh
SL01	Target Components and Capsules for SNL	585	Kaae
SL02	Target Fabrication for SNL	667	Schroen-Carey
UR01	Target Production and Delivery for LLE	1,405	Miller
UR02	Cryogenic Capsule Development	200	Miller
UR03	Flat Foils	150	Walsh
CR/LL1	Enhanced Cryo. Target Fielding Development	693	Sater
CR/LL2	NIF Cryogenic Target System Development	289	Alexander
CR/LA1	Beta Layering Support at LANL	216	Sheliak
CR/UR1	OMEGA Cryo. Target System Engineering	955	Besenbruch
	Total	$10,407	

[(a)]Additional support provided by the Lab.

1.1. LL01 ON-SITE SUPPORT FOR LAWRENCE LIVERMORE NATIONAL LABORATORY (LLNL)

Our on-site team at LLNL was composed of Derek Coker, Derrick Mathews, Craig Rivers, and John Ruppe. They provided support in micromachining of target components, assembling target components into complete targets, and characterizing target components and capsules for use in NOVA and OMEGA ICF experiments.

1.2. LL02 MICROMACHINED TARGET COMPONENTS

This year we fabricated 1510 micromachined components of various types in this task for both LLNL and Los Alamos National Laboratory (LANL). Nine hundred and fifty (950) of these components were gold-plated hohlraum mandrels of numerous different types. Included were 325 thin-walled hohlraum mandrels of different configurations where the coating consisted of 2–4 μm of gold and 100 μm of epoxy, and 30 double-walled hohlraum mandrels where the gold coatings were double layered. Unusual components also produced were 57 trapezoidal-shaped 25 μm thick gold shields. The other components produced were plates of various types including conventional aluminum witness plates, aluminum hat-shaped plugs, stepped witness plate profiles in polyimide, sine wave profiles in copper, bimetallic witness plates, and gold circular disks with a conical indentation coated with iron. The latter two components are unique, not having been produced previously (at least at GA), and the techniques used to produce them are described in Section 3.

1.3. LL03/LA02/UR01/UR02 COMPOSITE POLYMER CAPSULES

The number of target-quality capsules requested and delivered for ICF experiments increased by 30% over the previous year (see Table 1–2). Quality, flexibility, and rapid response remained excellent. We shipped 120 target-quality capsule orders, an average of one order every two days, and most orders were small, consisting of 7 or fewer targets. However, the complexity of the capsules remained high; most consisted of multiple layers doped with deuterium, silicon, chlorine, titanium, or germanium. About 6% were glass or coated glass shells.

TABLE 1–2
TARGET-QUALITY CAPSULE DELIVERIES

Laboratory	FY98		FY99		Change	
	Capsules	Orders	Capsules	Orders	Capsules	Orders
LLNL	124	7	292	19	135%	171%
LANL	60	3	120	8	100%	167%
UR/LLE	878	82	969	93	10%	13%
Total	1062	92	1381	120	30%	30%

In addition, we supplied over 300 near target-quality capsules, mostly to support developmental activities at the national laboratories. We also supplied over 900 sample shells of a large variety of types and over 200 g of silicon-doped polymer.

Orders for four target types required expanding our capabilities this year. The first was for much larger capsules, 2 and 3-mm diameters. Previously, we had delivered capsules made by the glow discharge polymer/poly(α-methylstyrene) (GDP/PAMS) process between 0.9 and 1.6 mm in diameter. We had not expected the ICF program to require production of 2 mm and larger capsules until National Ignition Facility (NIF) was operational, although GA has supported LLNL's experimental program for developing NIF capsules. Thus, we put large PAMS shells development on fast track to make mandrels of sufficient quality for the larger capsules. At the 2-mm size, concentricity, sphericity, internal debris, and reproducibility had been significant problems. We found that the quality has improved by making thinner-walled PAMS shells. The atomic force microscope (AFM) spheremapper spectra of the best 2 mm GDP capsules made from the PAMS shells approached the NIF standard.

The second new type of target request was for NOVA-type capsules with much smaller diameters, 220 μm. These "half standard-size capsules" are similar to full-size NOVA-type capsules: they have a polystyrene (CH) inner layer coated with poly (vinylalcohol) (PVA) and an outer layer of doped GDP. We made modifications to our equipment and processes to make the PAMS shells. We were pleased to find that the PVA and GDP coating processes worked as well as for the standard-size capsules.

The third new target type was the hemishell. GDP was deposited on PAMS shells. The coated shells were potted in Crystal Bond® and ground down to their equators. The hemishells were freed by dissolving away the Crystal Bond® with acetone. The PAMS mandrels were then dissolved away with toluene. The final product is shown in Fig. 1–1.

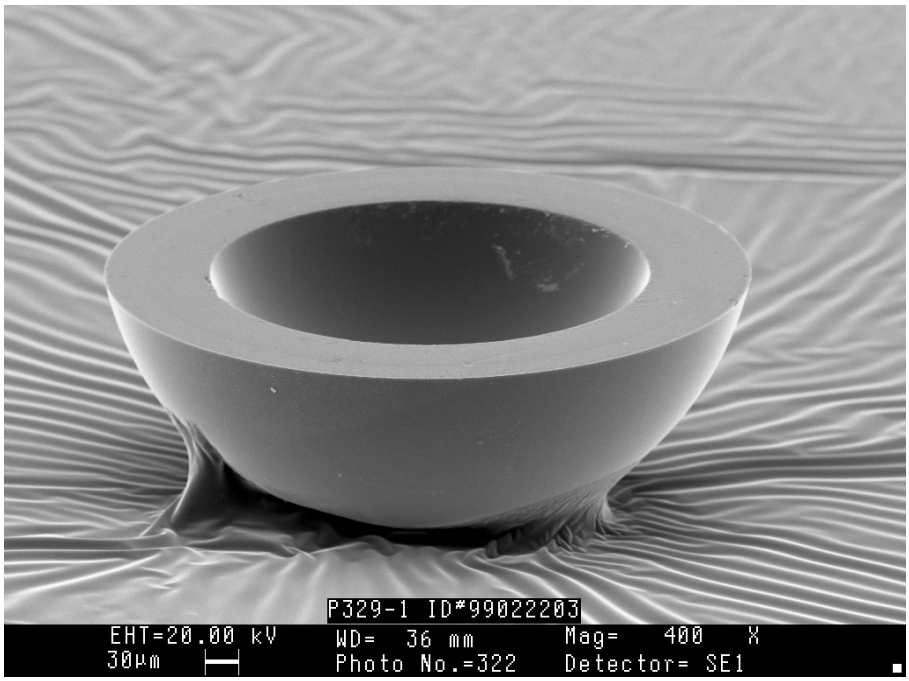

Fig. 1–1. A scanning electron microscope photomicrograph of a hemishell sitting on sticky tape.

The final new target type was very large, thick-walled glass shells. We discovered last year that it is possible to make high-quality glass shells from shells made of GDP doped with a suitable oxide such as silicon or titanium. The technique seems to be adaptable to making any diameter for which PAMS shells are available. Previously by using the drop tower furnace process for making glass shells, we were limited to diameters below 1.8 mm and wall thickness below 5 µm for diameters above 1.4 mm. The new technique can make much larger diameters with the wall thickness considerably greater than 5 µm. Large, strong glass shells with excellent concentricity and surface finish would be of great advantage for deuterium-tritium (DT) layering experiments since they could be handled at room temperature and would not require a fill tube. We developed the process to make the shells desired for the DT layering experiments.

We also made a number of improvements that significantly reduce the amount of labor required for some capsules (by using PAMS rather than GDP for the innermost layer of a NOVA-type capsule); these techniques improve the PVA layer on large capsules, and improve the surface finish of GDP on large capsules. In characterization, we continued to develop the spheremapper/wallmapper combination for determining the power spectra of the inner and outer surface finish on transparent capsules as well as the power spectra of wall thickness variations. In addition, we improved our technique for determining the leak rate of deuterium from large capsules.

We assisted the ICF laboratories to solve the problem of inadequate gas pressure in a polymer capsule at shot time. Leakage of fill gas from polymer capsules shipped from

one laboratory to another was a significant problem. The initial solution was to keep the filled capsules cooled with dry ice. In practice, we found that the capsules were not always kept at dry ice temperature by the shipping companies so the pressure at shot time was not well known. We suggested keeping capsules, with a predetermined leak rate, in a pressure vessel filled with the desired gas pressure. By knowing the leak rate and the time between removing the capsule from the pressure vessel and shot time, the pressure at shot time can be reliably calculated. We fabricated shipping/storage pressure vessels to do just that as part of task SL01 (see Section 1.8).

Our major developmental activity was to make thin-walled polymer shells for OMEGA cryogenic laser experiments. The capsules need to be as thin as possible while having enough strength to be filled with DT as quickly as possible to about 1000 atm.This places stringent strength requirements on the material from which the shell is made. We investigated how to increase the strength of the GDP films by exploring the coating parameter space of the helical resonator system used for depositing such films. We found that by depositing GDP on the PAMS shell mandrel under a much lower system pressure, the strength of the resulting pyrolyzed GDP shell was doubled.

1.4. LL04 TARGET DEVELOPMENT FOR NIF

LLNL requested additional support in several areas and provided additional funds for this work which is summarized here.

1.4.1. D_2 Test System Design (Task A) and Engineering Support for the NIF Cryogenic Target Planning Documents (Task B)

Under Subtask A, the deuterium test system (D_2TS) design was nearly completed and the procurement process was started for the majority of the capital equipment. The conceptual design and draft documents produced in Task CR/LL2 for the D_2TS were the starting point for final implementation of the D_2TS design (see Section 1.11).

The D_2TS consists of eight main subsystems (Fig. 1–2): the main cryostat, the cryogenic target gripper, the permeation cell, the permeation cell housing and motion system (PCHMS), the permeation cell support and cooling system (PCSCS), the permeation cell plug remover (PCPR), the cryostat sliding mount, and the gate valves. Drawings for the cryogenic target gripper have been released for fabrication. Parts for the gripper are in-house and assembly has begun. A test fixture for verification of its performance is in preparation. The specifications have been released and quotes from vendors have been received for the main cryostat and the gate valves. The PCHMS and the PCPR's vacuum chamber specifications have been released and requests-for-quote issued to vendors. The permeation cell, the PCSCS, and the cryostat sliding mount drawings are in the signature

cycle. Draft drawings for the remaining items of the PCPR are being checked by our drawing checker. We expect to complete the assembly, testing, and installation of the D_2TS at LLNL next year.

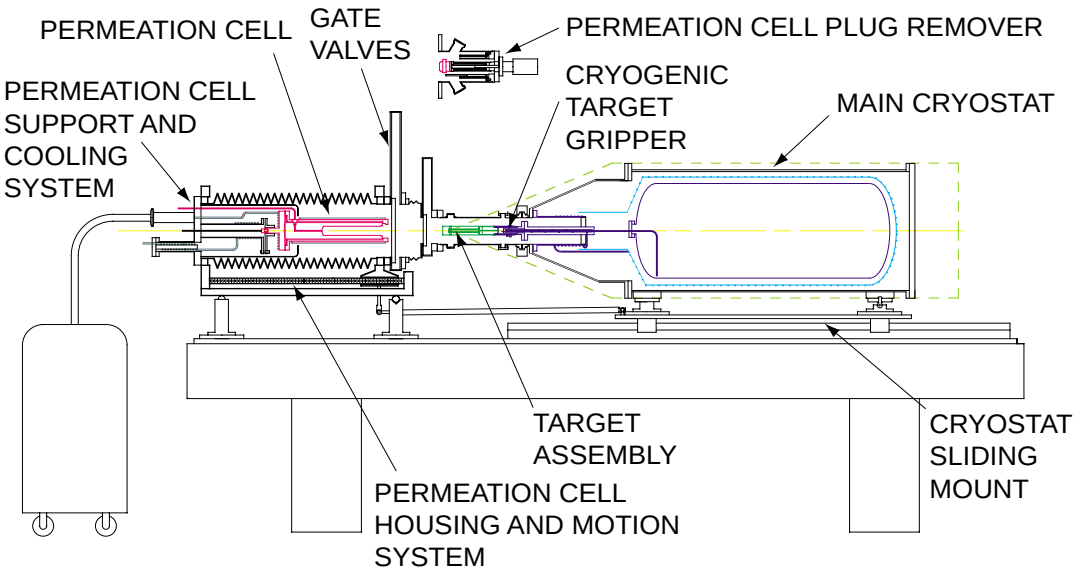

Fig. 1–2. The main cryostat of the D_2TS retrieves a target assembly from the permeation cell once the target has been filled and cooled.

A new NIF cryogenic target system (NCTS) planning document was prepared up to the level of a final draft under Subtask B. The new document is "Design Concepts for Fielding of NIF Cryogenic Ignition Targets." It updates the previous document, "Development of Concepts for Fielding NIF Targets and Planning for the Development of Fielding Subsystems," General Atomics Report GA–C22757 (1997). The latest draft of the new document was printed, bound, and sent to program managers and concerned individuals throughout the U.S. and French ICF programs as instructed by the technical contact. This draft is complete except for cost estimates, which are still under review at LLNL. It contains updated design concepts for fielding targets and updated schedules.

1.4.2. Polishing Beryllium Capsules (Task C)

We fabricated a device to polish NIF-sized beryllium shells by either mechanical polishing or electrochemical polishing. The device is very flexible, allowing for control of many parameters so that we will find optimal polishing conditions to obtain a surface finish with an rms roughness of better than 20 nm. Among the controllable variables are capsule diameter (1.5–3.0 mm), independent rotation and positioning of the top and bottom polishing plates, lap materials, groove size, and the force on the capsules. The device is easy to operate, yet limits the potential spread of beryllium contamination while

allowing a simple and quick disassembly of the device for cleanup. Initial testing of the device is underway.

We also prepared a laboratory for the safe operation of beryllium polishing activities. Access to the laboratory will be restricted to trained personnel during beryllium operations. The beryllium operations will take place in a hood with a HEPA filter that will trap any airborne beryllium dust. Our airborne beryllium concentration will be well below the current standard of 2 $\mu g/m^3$ and the proposed 0.2 $\mu g/m^3$ [8-h time weighted average (TWA)].

1.4.3. Modeling and Support (Tasks D and E)

Under Subtask D, work was performed augmenting the analytic and laboratory support to develop and implement infrared (IR) illumination schemes for NIF scale hohlraums for Task 99LL/CR1 summarized below in Section 1.10, and discussed in great detail in Section 5.1. Subtask E provided for on-site Nova Target Task Co-ordination developing target definitions; identifying and resolving target problems both from a material, as well as the fabrication/assembly viewpoint; developing detailed target drawings and specifications; and scheduling/coordinating appropriate levels of effort from within the Target Area Technology groups and outside resources to produce the targets. Additional work in this task provided for development and evaluation of new thin-film coating techniques. Of particular note was the successful delivery of a cryogenic Scale 1.25 gasbag target simulating NIF conditions that helped keep the cryo experiments on schedule. The upgrade and implementation of a 5-gun sputter coating system led to successful Be/Be+ doping operations providing coating thickness uniformity of better than 2% within a 2-in. diameter area.

1.5. LA01 ON-SITE SUPPORT FOR LANL

We provided two technicians to give on-site support for LANL under this task. At LLNL, Kett Gifford assembled and characterized numerous LANL targets and provided some micromachining support to the target fabrication effort. At LANL, Steve Dropinski provided on-site support for target machining, assembly, and characterization of targets that were shot at NOVA, Trident, Z, and OMEGA. When Dropinski was transferred to Sandia National Laboratory (SNL), this role was filled by Ron Perea. All three technicians provided assistance during LANL target campaigns at the University of Rochester/ Laboratory for Laser Energetics (UR/LLE) when required.

1.6. LA03 BERYLLIUM SHELL SUPPORT FOR LANL

LANL has taken the lead in developing the capability to manufacture beryllium capsules based on the machining of diffusion-bonded beryllium cylinders. We provided characterization support after key steps so that LANL could assess the quality of each step in the process. LANL sent diffusion-bonded beryllium cylinders and asked that we determine if a copper compositional gradient existed at the seal, how well the joints had turned into a seal, and whether the sphericity of the cavity was affected by the heat and pressure. After making modifications to our radiography procedures, we were able to provide the answers. This task was carried out in cooperation with the LLNL support activities described in Section 1.4.2.

1.7. NR01/UR03 NIKE TARGET PRODUCTION AND OMEGA FLAT FOIL FABRICATION

The NR01 and UR03 tasks are, as in past years, closely related. The production of flat films for both the NIKE laser program at the Naval Research Laboratory (NRL) and the OMEGA laser program at UR/LLE utilizes many of the same techniques. However, there are also significant differences in film compositions and configurations and in the products delivered to the two laboratories. Both programs require polymeric films which are flat and very smooth as well as films which are flat but have prescribed patterns on at least one of the surfaces. The patterns may be sinusoidal, step functions, and in some cases are sinusoidal in two perpendicular directions. There are requirements for films which are 1.5-μm thick but which are composed of 20 interleaved layers: 10 layers of polyimide and 10 layers of gold. In Section 4 of this report, we discuss in more detail the varieties of targets produced and delivered and the techniques by which the targets are produced.

The quality specifications and requirements for both LLE and NRL targets are dictated by particular experiments, laser beam quality, and the diagnostics to be used for the experiments. Ideally, in all cases, there should only be deliberately applied patterns on the targets — not random irregularities, dust, or other unwanted perturbations. The general target specifications and limitations for the two tasks include film curvature, surface smoothness, material purity, and volume inclusions such as bubbles or particulates.

We produce several types of multilayered targets for the laser programs. LLE targets include layered films of CH and silicon-doped polystyrene (SiCH), some with both surfaces smooth and some with applied perturbations such as sinusoids and orthogonal sinusoids. NRL targets include multilayer films, stepped aluminum layers, gold layers, and metal layers which have various step functions imposed on their surfaces.

A major emphasis during the past year has been the reduction of dust and imperfections on targets. As LLE and NRL laser uniformity and diagnostic instrumentation become increasingly precise, the requirements for target quality increase accordingly.

1.8. SL01 COMPONENTS AND CAPSULES FOR SNL

We fabricated 281 micromachined components of 42 different types for SNL this year on this task. Of these components, 110 were hohlraum-type cylinders of 26 different kinds. Many had relatively thin (~2 μm) walls of copper, but others had walls of GDP plastic or gold. One hundred and sixty four (164) of the components were break-out plates of 15 different kinds. The break-out plates were all made from aluminum although some were made from 1100 grade (commercially pure) aluminum while others were made from 6061–T6 aluminum (a precipitation-hardened aluminum in the fully hardened state). An unusual request received this year was for 5-mm diameter spheres machined from CH foam with a density of 50 mg/cc. This is an extremely friable material that is difficult to handle, but we were able to produce the requested spheres in our first series of machining trials. Machining spheres was something we had never attempted before. The method we used to machine the spheres is described in Section 3.4.

In capsule activities, we improved the PVA dip-coating process for Z-pinch capsules enabling the capsules to hold hydrogen, deuterium, and argon for a time (over 24 h) sufficient for the capsules to be mounted and shot on Z without losing a significant amount of gas. At the same time, we improved the quality of the surface finish and the uniformity of the PVA layer. The net result of the improvements was that the newest SNL capsules now have a deuterium retention half-life of two weeks.

In addition, we also helped solve the problem of determining the gas pressure inside the capsules at shot time. In order to maintain the fill gas pressure in polymer capsules, we formerly shipped them from one laboratory to another packed in dry ice. In practice, however, the fill gas pressures at shot time were varied since they were not always maintained at the dry ice temperature by the shipping companies. We suggested keeping capsules, with a predetermined leak rate, in a pressure vessel filled with the desired gas pressure. We fabricated shipping/storage pressure vessels to ensure that capsules contain the correct pressure upon removal. Each vessel holds a single capsule and has an attached pressure gauge to determine leakage (Fig. 1–3). The Department of Transportation approved use of the vessel for shipment by air. A trial shipment of a vessel was successful.

Fig. 1–3. This vessel can be safely used to ship and store a capsule under pressure until the capsule is removed just before shot time. The pressure vessel is more reliable and easier to use than the previous technique of keeping the capsule cooled by dry ice.

1.9. SL02 FOAM TARGETS FOR SNL

In FY99 this task was divided into two subtasks: (1) on-site support, and (2) fabrication and machining of low-density foams.

On-site support was supplied by Steve Dropinski. Mr. Dropinski had previously been assigned to LANL. His experience there and on other ICF projects has proven to be very valuable in the assembly of SNL's increasingly more complex target designs. His daily tasks were not limited to just assembly but also included working with experimenters to help design targets that were feasible. He was also responsible for installing and maintaining the laboratory equipment used in the target fabrication laboratory.

FY99 was the third year that SNL had specifically requested a subtask for producing foams. While the budget has increased each year, so has the complexity and number of foam components requested. SNL is now using foams as targets, as dampeners to prevent premature closing of diagnostic holes, and as blockers to prevent early radiation

transport. As many as 22 foam components have been used in a single target shot. To meet this need, we delivered 480 foam components in FY99. This represents almost twice the number for foams expected in the task statement. This is the second year in which the foam task has greatly exceeded the task statement. Our ability to streamline the process and produce batch quantities of components has produced significant savings while also improving quality in areas such as density uniformity and dimensional tolerances.

This year we also made a rather extraordinary change in the task to try to meet SNL's needs. The Task Leader of the foam task was relocated to SNL. With SNL's heavy dependency upon foams, it became imperative for the person developing the procedures and designing the production techniques be available to the SNL experimenters to explain the possibilities and limitations of foam in the various designs. Thus, Diana Schroen-Carey was relocated to Albuquerque, New Mexico, in June of this year. She is responsible for interfacing with the experimenters and developing foams to meet their future needs. Kelly Youngblood, Pat Collins, and Scott Faulk remain in Livermore to produce the foam components.

1.10. CR/LL1 ENHANCED CRYOGENIC TARGET FIELDING DEVELOPMENT

Cryogenic targets for OMEGA and the point design for NIF both require methods for making and characterizing smooth layers of DT ice inside of spherical plastic capsules. Current designs call for saturated vapor densities of 0.3 mg/cc over the DT solid corresponding to a temperature of 18.3 K. The required roughness of the inner layer is less than 1.4 μm rms. During the past year, we have supplied three scientists and one technician to LLNL and UR/LLE to support the development of these cryogenic targets and target systems.

OMEGA is scheduled to begin a cryogenic campaign on D_2 filled capsules during the first quarter of FY00. We have provided them with necessary information to implement IR heating on the cryogenic target positioning system (CTPS). This has included assistance in vendor selection for an IR laser and IR fiber, suggestions for modifications to the CTPS to allow routing of an IR fiber to illuminate the layering shroud, and a working prototype of a spring-loaded optical fiber connector. The connector is designed to allow remote assembly of the fiber connector between the base of the CTPS and the removable shroud.

We provided a skilled technician to produce assemblies of complex cryogenic targets as well as general support. This past year, a major advance has been made to improve shell durability and quality through improvements in assembly techniques. We now have the capability of gluing small (~30-μm o.d.) quartz tubes into drilled plastic shells. Shell survival after exposure to DT has risen from about 8 days with integral fill tube shells to

at least 6 weeks. Wall uniformity has improved sufficiently to allow us to begin investigation of joule heating with spherical plastic shells.

A substantial effort has been devoted to modeling the details of the shadowgraphic technique used to characterize the ice layer surface roughness. This study provided information on the relationship between bumps and holes of different sizes and the resulting shadowgraph as well as helping to establish limits on the ultimate measurement resolution achievable.

Emphasis this year with beta-layering has been to try to achieve a smooth DT layer at 18.3 K via slow cooling from the triple point. We have not been able to achieve our goal and have consistently observed increased surface roughness below 19.2 K. We are currently investigating the possibility of expanding this lower temperature limit through the use of enhanced layering techniques.

The IR smoothing project has continued to explore the available phase space for generating smooth layers. Engineering modifications have been made to the layering apparatus as well. IR light was formerly injected into the layering shroud/integrating sphere with lenses and mirrors. This has been replaced by an IR fiber running from the laser source directly into the layering sphere. Coupling efficiency for the fiber is about the same as it was previously with lenses and mirrors. Ray trace analysis of various IR illumination schemes has been carried out in order to help us optimize the layer uniformity. This modeling effort has also been expanded to include illumination schemes inside hohlraums in order to prepare for NIF.

1.11. CR/LL2 NIF CRYOGENIC TARGET SYSTEM (NCTS) DEVELOPMENT

The conceptual design of the deuterium test system (D_2TS) and initial design documents were produced under this task. They formed the basis for the final designs produced under task LL04 (see Section 1.4.1). Investigations of some of the implications of fielding NIF ignition targets utilizing a cryogenic system based on the D_2TS concept were also conducted. These investigations indicated that the original concept, Concept I, for the D_2TS would not be suitable for upgrading to a NCTS. A second concept was developed for the D_2TS, Concept IA, that overcame these difficulties. The latest version of Concept IA is shown in Fig. 1–2 (Section 1.4.1).

1.12. CR/LA1 BETA-LAYERING SUPPORT AT LANL

Beta-layering work at LANL during FY99 included the completion of the design, fabrication, and testing of all components of the cryogenic pressure loader (CPL) data acquisition and control systems; as well as the completion of the upgrade and testing of

the cryostat motion sync system electronics used for synchronization of DT layer image acquisition to cryostat motion. FY99 work also included the completion of setup and testing of the beta-layering experimental apparatus in preparation for upcoming solid DT layering experiments in a newly designed beryllium torus.

The CPL apparatus consists of a cryostat with integrated permeation cell, layering sphere, and target insertion mechanism. This apparatus will be used to test DT target filling and solid layering operations as well as measuring the amount of DT release from the target filling permeation cell to the cryostat volume. The apparatus will demonstrate the ability to produce β-layered targets as well as perform optical target characterization. The CPL apparatus also includes an optical system external to the cryostat, which functions as an image acquisition system and monitor for the target capsule once it has been filled in the permeation cell and lowered to the DT layering sphere position. The CPL control system will control target insertion and layering sphere positioning mechanisms as well as the x-y-z stage positioning mechanisms for the image acquisition and real-time monitoring cameras and optics. The image acquisition and monitoring systems will acquire and save images of the solid layering process as well as provide on-going monitoring of the process in real-time. The design, fabrication/purchasing, and testing of all essential components of the acquisition and control systems were completed this fiscal year.

The motion sync system uses a triaxial (x-y-z) accelerometer to monitor the mechanical motion of the cryostat due to cryogenic refrigerator vibration during beta-layering experiments. This motion occurs within the solid layer image plane as well as along the optical axis (image focus). The complex vibration and motion signal is reduced to a simple harmonic motion signal by the signal processing electronics. The motion signal is then used to produce a trigger pulse that synchronizes solid layer image acquisition to the motion of the beta-layering cell mounted inside the cryostat. The system electronics were upgraded to permit the extraction of the simple harmonic motion signal imbedded within the complex acceleration signal, which included a large noise signal.

Solid layering experiments are continuing with solid DT aging experiments. These experiments will be performed inside a newly designed beryllium torus, for which the surface-to-volume ratio has been closely matched to that of a sphere. These experiments will examine the effects of DT aging on the solid layer surface. The layering apparatus and image acquisition and analysis systems have been set up and tested and are now ready for experiments once the DT sample arrives.

1.13. CR/UR1 OMEGA CRYOGENIC TARGET SYSTEM (OCTS) ENGINEERING

During the past year, the team of UR/LLE, GA, LANL, and Schafer made great progress toward completion of the OCTS. All equipment was delivered to UR/LLE. Instal-

lation and system integration work is in progress. The following major achievements took place during FY99:

1. Procurement of all remaining components was completed.
2. The fill/transfer station (FTS) cryostat was shipped to UR/LLE November 1998.
3. GA personnel supported the first FTS cryostat cooldown at UR/LLE and performed thermal analyses in support of the FTS cryogenic testing.
4. The gloveboxes for the FTS and DT high pressure system were shipped to UR/LLE January 1999. (This work was performed by LANL.)
5. The DT high-pressure compressor was shipped to UR/LLE February 1999.
6. The lower pylon, surrogate tank, chain locker, and moving cryostat transport cart (MCTC) #2 were installed at GA's Bldg. 35 test facility and successfully used with the upper pylon in target placement and moving cryostat (MC) shroud removal tests. The equipment was returned to UR/LLE May 1999.
7. MC and MCTC #1 assembly work and cryogenic testing were completed successfully. The equipment was shipped to UR/LLE June 1999.

GA's remaining task consists of providing services as requested by UR/LLE to support the system installation and integration effort. These services will include consulting support and preparation of project closeout documentation.

Scheduling problems resulting from late delivery and rework of some MC shroud components forced technical compromises to maintain the overall schedule of shooting cryotargets in early FY00. The primary compromise was to reduce the degree to which integrated system testing was performed at GA with the MC/MCTC and the shroud pulling system. Specifically, no shroud pulling tests were performed with the shrouds at cryogenic temperatures. However, to the extent that subsystem testing and system integration work was performed at GA, it was very successful. UR/LLE will complete the system integration work with consulting support from GA.

2. CAPSULE DEVELOPMENT AND PRODUCTION

Orders for current Inertial Confinement Fusion (ICF) experiments required us to develop larger and smaller poly(α-methylstyrene) (PAMS) shells. We significantly improved our PAMS shells at the larger diameters, between 2 and 3 mm by making them with thinner walls. At the other end, we developed PAMS shells with 220 μm diameters for use in NOVA-type capsules [capsules with a dopant-free inner layer, a poly (vinylalcohol) (PVA) middle layer, and a (frequently doped) glow discharge polymer (GDP) outer layer]. We also continued the development of making large, thick glass shells from doped GDP shells and made significant improvements to the strength of thin GDP shells for OMEGA cryogenic experiments.

We made a number of improvements in quality and efficiency. A significant improvement to cost and quality was to use a PAMS shell, rather than a GDP shell, as the inner layer in NOVA-type capsules. We also improved the deposition of PVA on small shells (< 500 μm diameter) and large shells (near 1.6 mm diameter). In addition, we improved the surface finish of GDP-coated large shells by using a tapper mechanism during coating.

In characterization, we made several unique innovations at providing more complete characterization to assist Los Alamos National Laboratory (LANL) in the development of sealing beryllium hemispheres to make beryllium capsules. We showed improvements in atomic force microscope (AFM) spheremapping the outer surface of a capsule. We also demonstrated the "wallmapper" for determining the power modal variations in the wall thickness of a transparent capsule. By combining the wallmapper with the spheremapper, we are now able to determine the power modes of the outside surface, the inside surface, and the variations in wall thickness.

2.1. PAMS SHELL DEVELOPMENT

At the end of FY98, we had determined optimal conditions for making 1-mm PAMS shells. However, at the 2 mm size, concentricity, sphericity, internal debris, and reproducibility remained significant problems. This year, we fabricated 2 to 3 mm shells with good out-of-round (OOR), nonconcentricity (NC), and surface finish. In addition, we developed techniques for making much smaller shells for ICF experiments requiring targets with 250 μm diameters.

2.1.1. Large PAMS Shells

The ICF program required large shells for experiments during the year, somewhat of a surprise since we had not expected 2 mm shells would be required before National Ignition Facility (NIF) was operational. We found a number of new problems when we converted large PAMS shells into GDP shells. We observed the following problems:

- During the GDP coating process, agitation of these large, heavy PAMS shells led to abrasion. The abraded particles subsequently deposited onto the coating surface creating a number of domes on the capsule (see Section 2.3).
- Poor NC PAMS shells gave GDP capsules with poor NC.
- OOR and NC for PAMS shells varied considerably from batch to batch.
- The use of PAMS beads, which had good OOR, required careful and lengthy pyrolysis which often left behind excessive residue.

We decided to pursue relatively thin-walled PAMS shells in the hope that the reduction in wall thickness and total mass could help to resolve many of these problems.

Thinning the Walls. Initially, thinning the shell walls proved rather difficult. The following problems were encountered and resolved:

- The wet shells were fragile and broke during the curing process. This was resolved by using a higher PAMS concentration which made the oil phase more viscous and able to withstand the forces of agitation.
- Thin-walled shells broke (developed star cracks) during washing and sieving. This problem was avoided by eliminating the sieving, gently washing the shells, and removing the supernatant with gentle suction.
- Thin-walled shells broke (were blasted to bits) during the ultrasonication step used to nucleate an internal bubble. Microsonication at 170 kHz was much more gentle than ultrasonication at 40 kHz, which allowed the shells to be nucleated without destruction.
- The OOR of the thin-walled shells was very poor due to rapid curing. Addition of excess O1 solvent (fluorobenzene) to extend the cure time dramatically improved the OOR.

Table 2–1 shows data from our early batches of a number of representative large-diameter PAMS shells. The data shows that under similar curing conditions, the thinner walled shells have improved OOR and NC.

In addition to the improved OOR and NC of the 2 mm shells, the thinner walls also aided in the reduction of domes, and the low NC yielded a more uniform coating of GDP. The pyrolysis process was also less problematic using thin-walled shells than when beads

were used. The thin-walled shells required one day of pyrolysis whereas the beads required two full days and left significant residue behind.

TABLE 2–1
LARGE PAMS SHELL PRODUCTION

o.d.		Thickness		avg 4π	Radius	
o.d. (μm)	St Dev	Wall (μm)	St Dev	NC	OOR	Comments
3276	55	27.6	0.6	large	41	Shells cracked during aggressive drying
3171	41	26.2	1.3	large	21	Shells cracked during aggressive drying
3206	14	12.4	0.4	large	3	Shells cracked during aggressive drying
3171	10	12.7	0.7	large	5	Shells cracked during aggressive drying
2572	43	16.0	4.0	10%	6	
2009	18	14.9	0.8	20%	5	
2054	9	14.9	0.3	20%	4	
2044	8	14.8	0.4	20%	5	
2052	9	11.4	0.3	~5%	3	
2072	7	11.8	0.2	~5%	3	
2105	6	12.2	0.5	~5%	3	

Figure 2–1 shows typical AFM power spectra of 2 mm GDP shells delivered for ICF experiments. Some, but not all, of the capsules approach the NIF standard. We do not understand why two capsules from the same batch have such different spectra; this issue is currently under investigation.

2.1.2. Small PAMS Shells

ICF experiments in FY99 required fabrication of 250-μm diameter capsules. This was much smaller than capsules made previously by the GDP/PAMS technique. Modifications to the droplet generator system were necessary to make the required PAMS shells.

To make small diameter shells, we fabricated smaller needles for delivering the W1 and O1 phases, since the lower limit of the wet shell outer diameter is approximately the diameter of the O1 nozzle tip. In addition, the collection tube had to be restricted so that reasonable W2 flows could be used to strip off the shells. The result of these modifications was that shells were hard to see using a stroboscope due to heavy turbulence experienced by the shells upon leaving the needle tips. (The diameter of the shells just after formation is determined from the flow rate of O1 and the number of shells formed per second. The strobe is used to determine the number of shells formed per second.) With-

out the ability to strobe the shells, it was extremely difficult to accurately produce the desired diameter. This problem was solved by increasing the viscosity of the W2 fluid, thus decreasing the Reynolds number and eliminating the turbulence problem. In this way, PAMS shells of the correct diameter were produced at 300 to 400 shells/s.

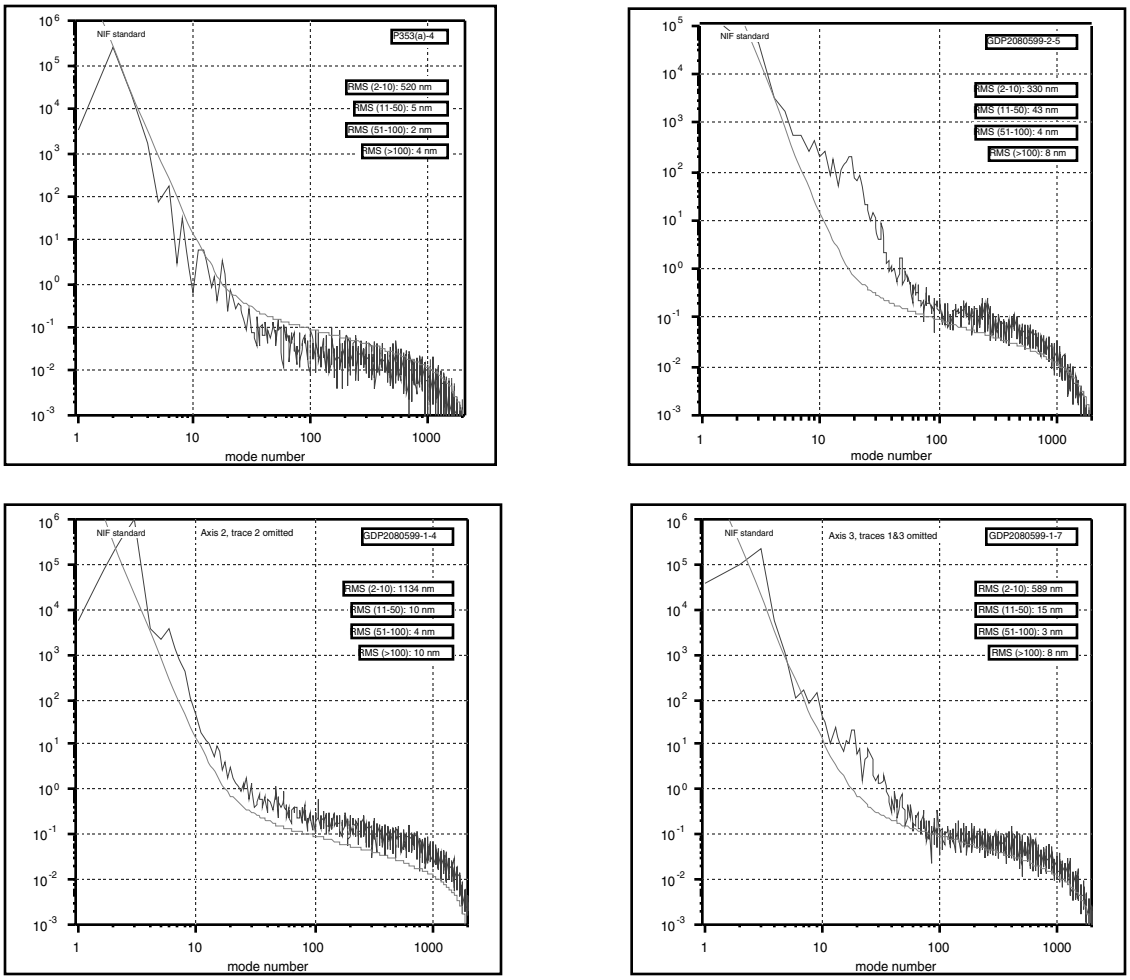

Fig. 2–1. The AFM power spectra from four typical GDP shells delivered to LLNL shows the overall surface finish for the very best shells approach the NIF standard.

Initially, the shell OOR was within specification (1 μm), but still higher than anticipated. Adding excess fluorobenzene to the curing beaker of shells extended the curing time and improved the OOR to a more expected value of 0.1 to 0.2 μm.

Another problem encountered with these smaller shells was that the high surface-to-volume ratio and thin walls (3 to 5 μm) lead to implosion of the shells during extraction of the interior water phase. By using a lower ethanol concentration during extraction to slow the rate of water extraction from the shell interior and frequent sonication, we were

able to nucleate interior bubbles in a more controlled fashion and prevent the implosion problem.

For further information, please contact Dr. B. McQuillan or D. Czechowicz (GA).

2.2. GLASS SHELLS FROM DOPED GDP

We discovered last year that it was possible to make high-quality glass shells by adding another step to the GDP/PAMS process. The procedure is shown in Fig. 2–2. In step one, doped GDP is deposited on PAMS shells. The dopant needs to be one that forms a suitable oxide such as silicon or titanium. In step two, the shell is pyrolyzed at about 300°C in an inert gas, such as nitrogen, to remove the PAMS. In the final step, the doped GDP shell is pyrolyzed in an oxygen-containing atmosphere to convert it into a glass shell.

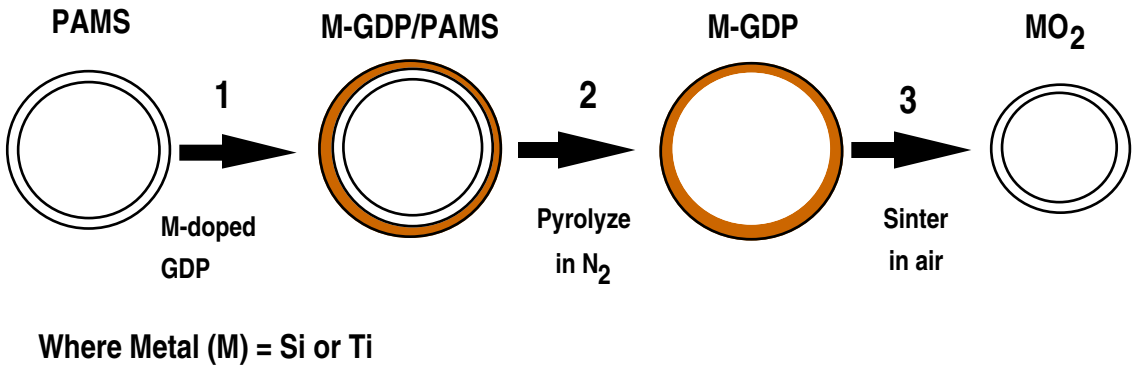

Fig. 2–2. Doped GDP shells are converted to glass shells.

Following the discovery that we could convert silicon-doped GDP into high-quality glass shells (Fig. 2–3), an order was placed by LLNL to manufacture glass shells large enough and strong enough for cryogenic experiments. Large, strong glass shells with excellent concentricity and surface finish would be of great advantage for deuterium-tritium (DT) layering experiments since they could be handled at room temperature and would not require a fill tube. The wall thickness and diameter requirements (i.d. ≥ 1400 μm; wall ≥ 12 μm) for the shells requested were outside of the range which could be made using the drop-tower method. These specifications also exceeded the diameter and thickness of any glass shells made by the newly discovered GDP process; but we were confident that with some optimization of our technique and suitable PAMS mandrels, we could manufacture them.

The largest high-quality PAMS mandrels we had available for this project were near 2100 μm in o.d. with ~12 μm walls. However, the substantial shrinkage (~30% in o.d.

and wall) that occurs in the sintering step of the process meant that even if we were successful in optimizing the process, we would only be able to make glass shells near the low end (1400 μm o.d.) of the desired specification.

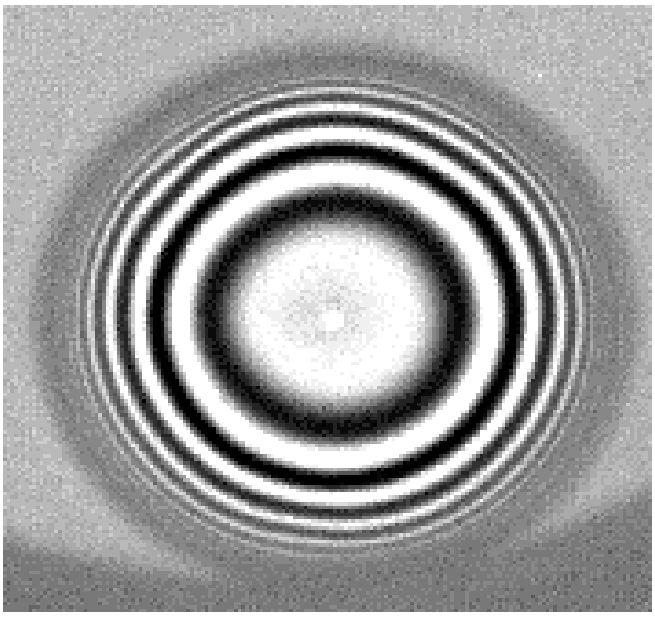

Fig. 2–3. An interferometric image of an SiO_2 shell resulting from the pyrolysis of **Si**-GDP confirms this process is capable of producing highly uniform shells.

Three substantial difficulties had to be overcome in order to obtain glass shells starting from the ~2100 μm PAMS mandrels we had available: preventing the **Si**-GDP mandrel from collapsing or shattering during the PAMS removal step, preventing the **Si**-GDP mandrel from turning black and becoming opaque during the air pyrolysis step, and preventing the mandrel from fracturing during the conversion of **Si**-GDP to glass. Utilizing the limited amount of resources available for this task, we were able to solve the first two difficulties and made substantial progress on the third.

Resolution of the problems encountered during PAMS removal were accomplished by adjusting the silicon concentration in the silicon-doped GDP and optimizing pyrolysis conditions. Control of silicon concentration proved to be crucial. High silicon concentration minimizes shrinkage and adds rigidity to the mandrel helping to eliminate deformation or collapse of the shell during PAMS removal. However, too high a concentration of silicon leads to a brittle shell which shatters during the PAMS removal step. A compromise concentration was found to be about 8 at. % silicon in **Si**-GDP. In addition to controlling the silicon concentration, utilizing PAMS mandrels with as thin a wall as possible and slowing the PAMS removal process to a two-day procedure also proved beneficial. Figure 2–4 illustrates the quality of the **Si**-GDP mandrels which can be made

by this process. The AFM spectrum of the free-standing silicon-doped GDP mandrel is essentially identical to that of the PAMS mandrel.

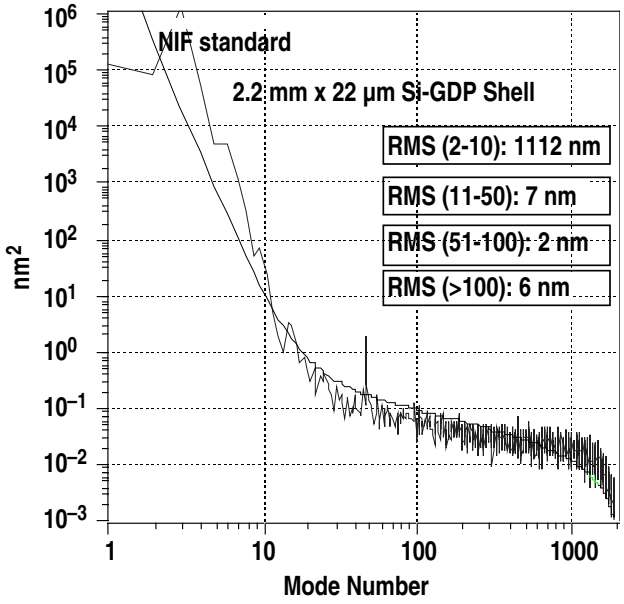

Fig. 2–4. AFM power spectrum of a **Si**-GDP shell confirms that no significant deformation occurred during removal of the PAMS mandrel.

Once PAMS-free **Si**-GDP mandrels of suitable size and wall thickness were made, the key to making clear and colorless glass shells was optimizing the pyrolysis conditions (Fig. 2–5). If the temperature in the oven is raised to 600˚C before all of the hydrocarbon has burned away, formation of carbides and/or graphite results and the resulting shell is black [Fig. 2–5(a)]. If instead the temperature is maintained at 550˚C in air for a sufficient length of time, the resulting glass shell is clear and colorless [Fig. 2–5(b)]. Since C-H bonds generally are not stable in excess of 600˚C, this result is not entirely surprising.

The final problem, that of shell fracturing during air pyrolysis, has not been fully resolved. This failure mode frequently results in the formation of hemishells (Fig. 2–6). The yield of this air pyrolysis step currently is around 30% for glass shells ~1400 µm o.d. with walls ~13 µm thick.

The **Si**-GDP shells that survive the conversion to fully dense SiO_2 shells can be made with very low geometrical deformation as illustrated by the AFM spheremap of a 1350 µm o.d. × 13 µm wall glass shell shown in Fig. 2–7.

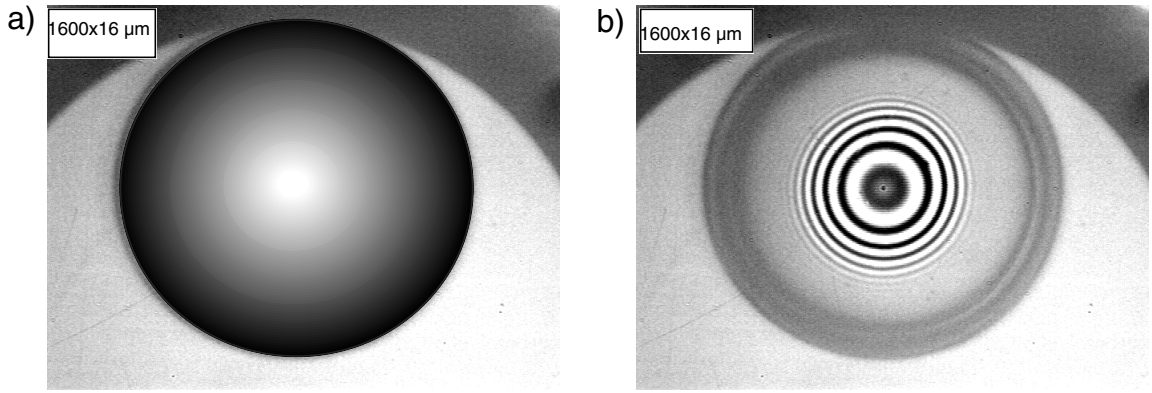

Fig. 2–5. Pyrolysis conditions can determine whether the resulting shell is opaque or transparent.

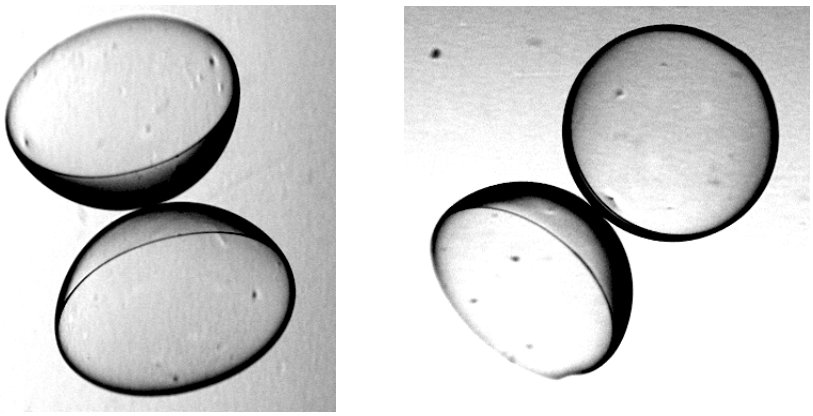

Fig. 2–6. Hemishell formation is a common failure mode during conversion of thick-walled **Si**-GDP shells into glass shells.

Strength and permeability measurements on glass shells made from silicon-doped GDP show very interesting properties. Glass shells resulting from **Si**-GDP pyrolyzed to 600˚C in air are not yet fully dense. Helium permeation through these glass shells at room temperature has a half-life of seconds and deuterium only a few minutes. However, these shells are essentially impermeable to oxygen and water as is confirmed by the formation of water droplets inside a shell during an attempt to fill one such shell with deuterium at 360˚C. After sintering at 1000˚C for an extended period of time, the resulting fully dense shells exhibited permeation properties expected of pure silica glass shells. Strength tests (compression and burst) utilizing helium gas on a few fully densified shells

made by this process confirmed they were as strong as expected in compression mode, but had burst strengths at only about 70% as was expected of typical glass shells. The reason for this disparity is not clear but could be related to the inclusion of small, scattered defects within the wall of the glass.

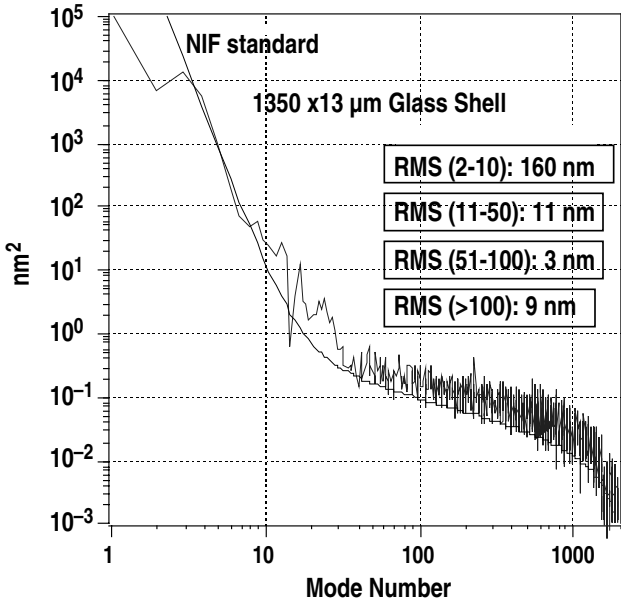

Fig. 2–7. AFM spheremap demonstrates the high quality of SiO_2 shells which can be made from **Si**-GDP.

For further information, please contact Dr. M. Hoppe (GA).

2.3. GDP COATING IMPROVEMENTS

Our major developmental effort in GDP coatings was to determine the effects between the parameters of the coating system and the strength of the resulting layer. Strong, thin-walled capsules will be needed for cryogenic experiments on OMEGA. University of Rochester/Laboratory for Laser Energetics (UR/LLE) is developing techniques for making the capsules from polyimide; GA is tasked to determine if acceptable capsules can be made from GDP. We found conditions that doubled the strength of thin-walled GDP capsules.

Another improvement is to the surface finish of GDP-coated capsules greater than 2 mm diameter. We discovered that a tapper mechanism, which jarred stationary shells at intervals during the GDP deposition, resulted in excellent surface finishes and allowed many more shells to be coated together without decreasing the surface quality.

2.3.1. Fabrication of Stronger Thin Wall Capsules for UR/LLE

Thin-walled polymer shells are needed for OMEGA cryogenic laser experiments. The capsules need to be as thin as possible while having enough strength to be filled with DT as fast as possible to about 1000 atm. This places stringent strength requirements on the material from which the shell is made. We investigated how to increase the strength of the GDP films by exploring the coating parameter space of the helical resonator system used for depositing such films.

We built an apparatus to measure the buckle and burst strength of our shells. A simplified schematic of the apparatus is shown in Fig. 2–8. Shells were placed in a grid inside the main chamber, which had windows for direct optical inspection of shells. The main chamber was connected to a gas supply and a vacuum pump. Buckle testing was performed by pressurizing the chamber suddenly (<1 s) with nitrogen or sulfur hexafluoride which have very low permeability through GDP (half-lives > 3 minutes for 900 μm × 1 μm shells). The pressure was increased in small steps until the shells buckled. The chamber was vented immediately after each step to avoid filling shells with the test gas. A pressure regulator with 7 psi range and 0.2 psi resolution was used.

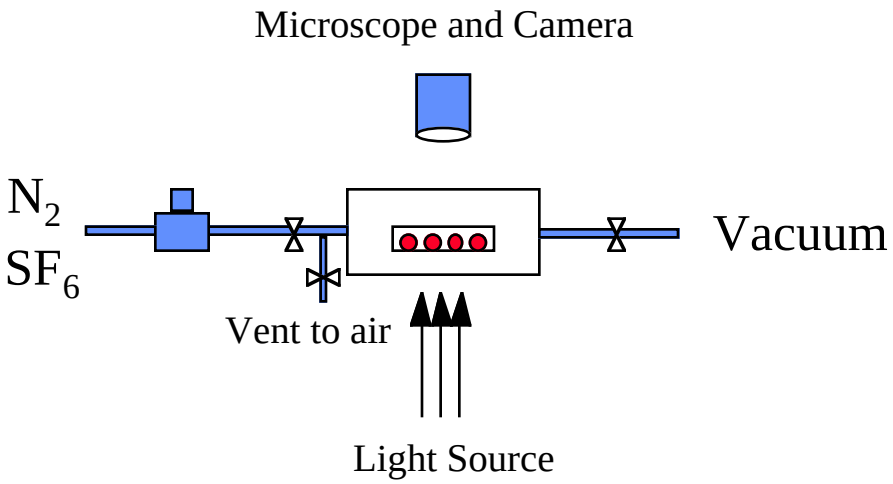

Fig. 2–8. Schematic of the apparatus made for buckle and burst testing thin-walled shells. The pressure regulator had a resolution of better than 0.2 psi.

Burst testing was carried out by first evacuating the test chamber, then slowly filling the shells to the desired pressure with helium, and finally evacuating the chamber suddenly.

For defect-free shells, the buckle strength is:

$$P_B = \frac{8E}{\sqrt{3\left(1-\nu^2\right)}}\left(\frac{t}{d}\right)^2 \quad , \tag{1}$$

where P_B is the pressure where shell failure occurs, E is Young's modulus, ν is Poisson's ratio, t is the thickness, and d is the diameter of the shell [2–1]. Therefore, to perform a comparison of buckle strength of shells made under different conditions, any difference in the aspect ratio (d/t) needs to be properly accounted for. To do this, we normalized all measured buckle strengths of shells of varying aspect ratios to that of a 900 μm diameter, 1-μm thick shell.

Making a GDP shell involves a number of steps and a number of parameters that can be varied in each step. We decided to vary only the GDP deposition parameters in our initial study reported here to reduce the parameter space as much as possible. Therefore, all thin-walled shells tested were made by depositing GDP on PAMS mandrels from the same batch. After deposition, they were stored under vacuum until pyrolysis. They were pyrolyzed using the same furnace and the same pyrolysis conditions. They were all tested shortly after the pyrolysis step to avoid prolonged exposure to air.

We varied our deposition conditions as follows. Coating pressure was varied between 10 and 200 mtorr. The H_2 flow rate was varied between 0 and 10 sccm at a constant trans-2-butene flow. The input radio-frequency power was varied between 3 and 30 W. These parameters were not all independent. For example, as the H_2 flow was increased, the minimum system pressure also increased. Therefore, it was not possible to perform a coating run at high H_2 flows and low system pressures. In addition, the PAMS shells disintegrated during the coatings at low pressures and high powers. Therefore, this also limited the usable parameter space. In a number of cases, multiple runs using the same coating conditions were performed to verify the reproducibility of the coatings. Shell thickness was measured by interferometry and verified in a number of cases by scanning electron microscope (SEM) measurements.

To summarize our results so far, coatings performed at the lowest pressures obtainable in our system (10 to 25 mtorr) resulted in the strongest shells. We made numerous runs under these conditions in various coaters in our lab, all resulting in shells that had normalized buckle strengths of about 1.5 psi. A number of these shells were sent to LLE for measurements that confirmed our measurements at GA. In contrast, shells made using deposition parameters usually used for deliveries (75 mtorr) only had a normalized buckle strength of ≈0.7 psi. In general, coatings performed at higher pressures (75 mtorr and higher), yielded shells that were not as strong.

The stronger shells made using lower deposition pressures (LDP) have a number of features that are very different from shells made using our usual higher deposition pressures (HDP). The LDP shells are much more robust in handling. They can be easily spheremapped (Fig. 2–9). They are also noticeably darker in color. Their buckling behavior is also very different. The LDP shells shatter or tear when they buckle as shown in Fig. 2–10. HDP shells are more elastic. Figure 2–11(a) shows an HDP shell buckled under 2 psi over pressure. Figure 2–11(b) shows the same shell, after the over pressure is removed. The HDP shell has bounced back. They can be cycled in this fashion many times. This behavior may imply a higher Young's modulus for the LDP shells and the resulting higher buckle strength.

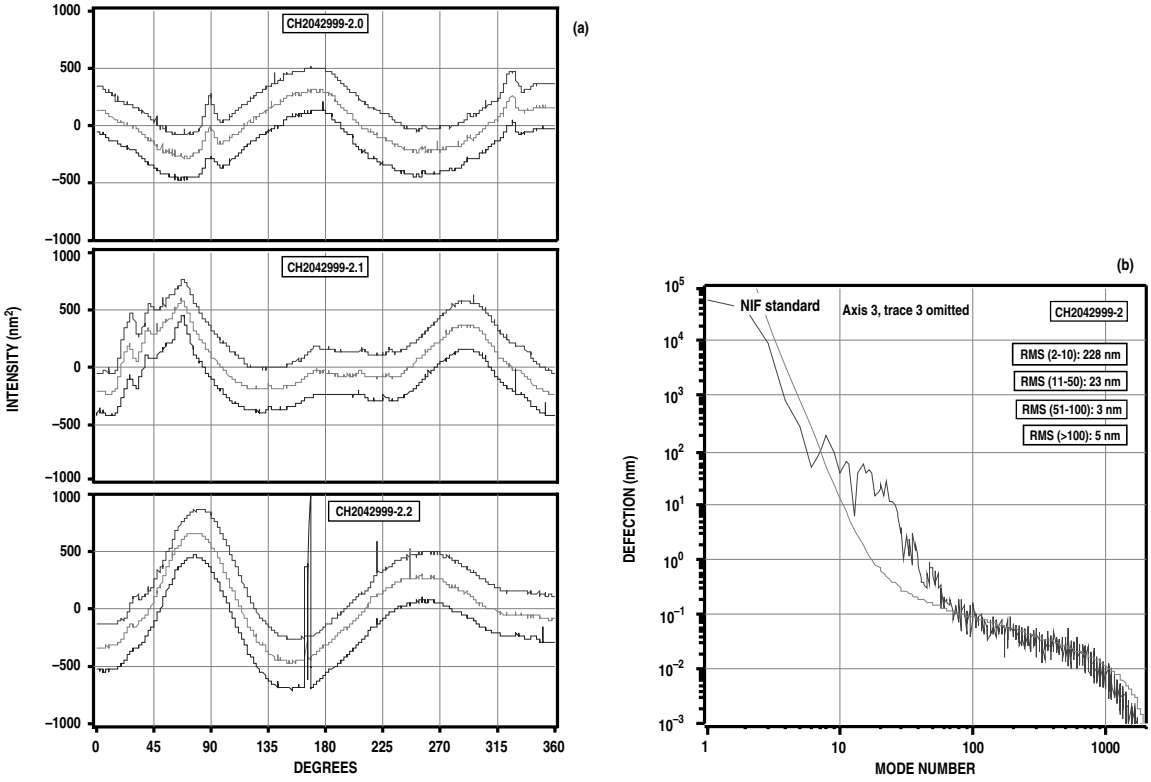

Fig. 2–9. AFM spheremap traces (a) and power spectrum (b) of a 930 μm diameter, 0.9-μm thick LDP shell. These shells are robust enough to be routinely spheremapped.

We also investigated how well Eq. (1) applies to our process. We started with 60 shells and performed 3 consecutive runs of the same duration and conditions, removing 20 shells at each break point. This resulted in ≈0.5, 1.2, and 2.4 μm shells, all at about 930 μm diameter. The strongest shells from each thickness group buckled at 0.4, 3.25, and 12.5 psi, respectively. This result is rather consistent with the theoretical aspect ratio dependence of buckle strength for a fixed Young's modulus.

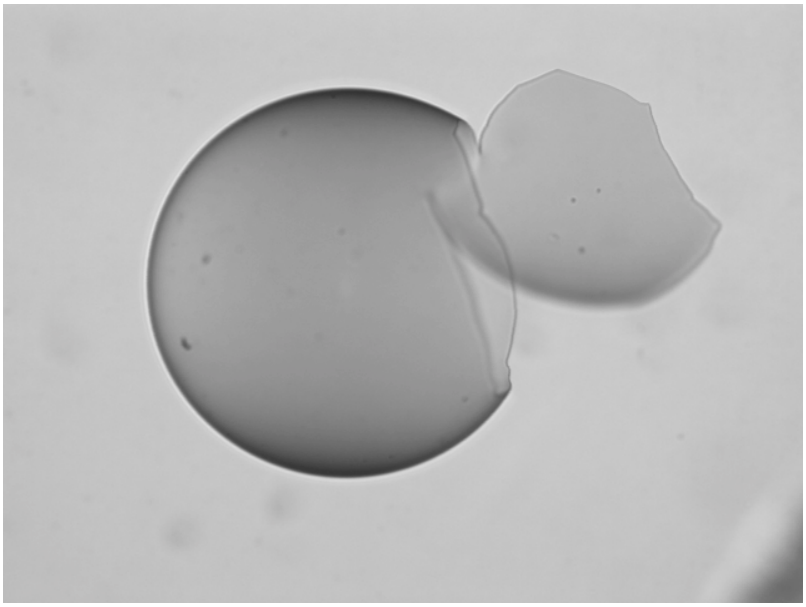

Fig. 2–10. An LDP shell ≈0.9-μm thick after application of over 2 psi of over pressure. Buckling of LDP shells is catastrophic and irreversible.

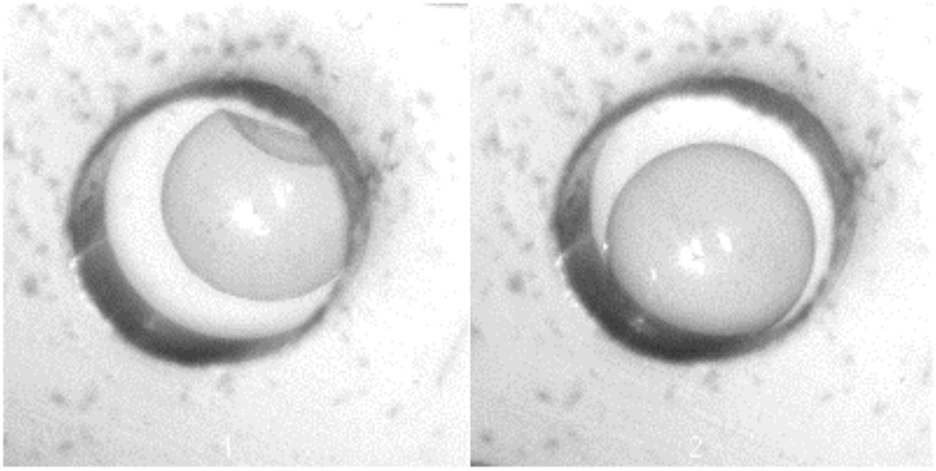

(a) (b)

Fig. 2–11. (a) An HDP shell, 880 μm in diameter and 1.3-μm thick, under 2 psi of over pressure. (b) Shell in (a) has bounced back after removal of the over pressure. The HDP shells are more elastic.

It is interesting to note that the above shells did not survive our fixed pyrolysis protocol. A modified extended protocol was used and most shells survived. This points out that failure of shells in pyrolysis does not necessarily indicate weakness of the coating.

We hope to continue this work to find out why LDP shells are stronger, and how we can change our process to make these shells even stronger.

2.3.2. Tapping Agitation for Coating Large Capsules

We showed previously that GDP coating large numbers of shells together using the bouncing agitation of the piezo shaker leads to dome-filled coatings [2–2]. The number of shells which may be bounce-coated together smoothly depends on the diameter and thickness (*i.e.*, mass) of the shells. The problem became severe when NIF size shells, 2 mm or greater in diameter were coated. We also showed that by using a modified, gentler agitation technique, many 2-mm shells could be coated together with virtually dome-free surface finish. This technique involved rolling the shells in a tilted spinning pan to avoid frequent head-on collisions between shells while providing ample agitation for uniformly coating the shells. While this method does produce very smooth GDP coatings on shells 2 mm or greater in diameter, it is rather problematic and unreliable to use as a production technique. The main problem involves the degree of the tilt of the pan. If the pan is tilted too much, some of the shells may fall out of the pan and be lost during coating. If the pan is not tilted enough, then the shells do not roll enough to receive a uniform coating. The proper amount of tilt changes as the shells are coated and become heavier. The pan tilt also affects the coating rate because the more the pan is tilted, the further away it is from the plasma and the less coating it receives. The larger numbers of deliveries involving 2 mm shells inspired us to devise a new agitation mechanism. This technique is based on the fact that tapping the pan during coating can knock loose an otherwise stuck shell when using the piezo bounce pan agitation.

In the tapping agitation technique, a small rod is attached to the end of an electronically actuated solenoid. When the solenoid is actuated, the rod jumps forward suddenly and taps the coating pan. Solenoid power is provided by a digital pulse generator output amplified by an audio amplifier. The pan is tapped once every one or two minutes. Since the GDP coating rate in our system is low (0.3 μm/h), the shells receive only tens of angstroms of coating between each tap and do not stick to each other. The shells are essentially stationary during most of the coating and do not collide with each other. This agitation scheme provides sufficient agitation to produce uniform coatings on concentric shells. Nonconcentric shells, however, receive a nonuniform GDP coating compensating for the initial nonuniformity of the mandrel. In the PAMS-GDP process, this leads to nonuniform GDP shells after pyrolysis. Such shells may be over coated with more GDP using the tapping agitation to obtain uniform final shells. Figure 2–12 shows a SEM photomicrograph of the surface of a 2-mm PAMS shell that was GDP-coated along with several other similar shells with 70 μm of germanium-doped GDP using the tapping agitation technique. The surface is virtually dome free. We have used this technique for coating over fifty 2-mm shells together in the same coating run with smooth, dome-free surface finishes. This method is currently used on a routine basis to make 2-mm shells for deliveries.

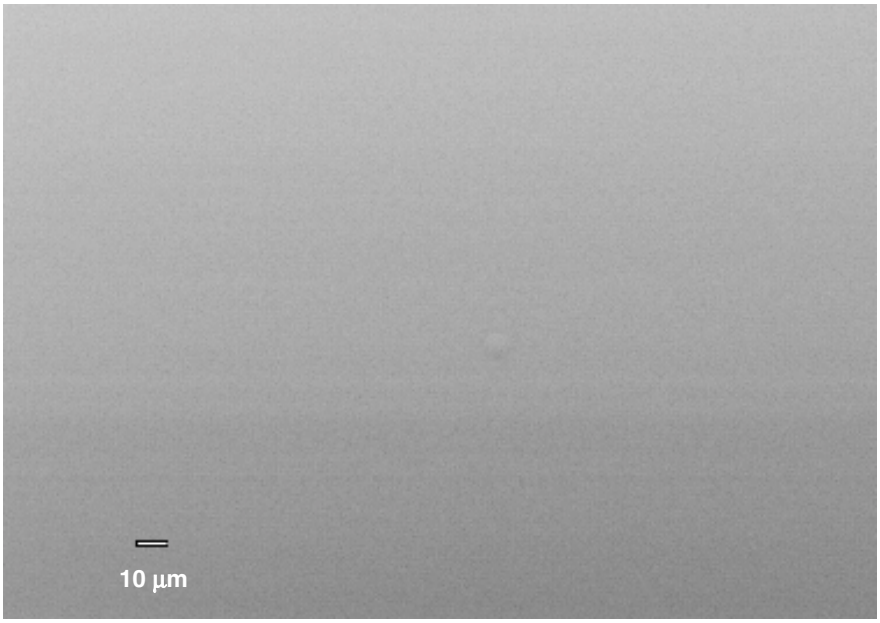

Fig. 2–12. SEM photomicrograph of the surface of a 12 µm × 2 mm PAMS mandrel coated with 70 µm of Ge-GDP. The shell surface is virtually dome free.

For further information, please contact Dr. A. Nikroo (GA)

2.4. TARGET PRODUCTION IMPROVEMENTS

We made substantial improvements to an assortment of target production processes. NOVA capsules were made using PAMS as the inner mandrel, a process improvement that saves hundreds of labor hours compared to the previous process. Better control over the NOVA capsule drop-tower PVA coating process was gained from a series of experiments on the interaction of key processing parameters. PVA coating of 1.6 mm Sandia National Laboratory (SNL) capsules was refined to give better surface finish, PVA thickness uniformity, and longer capsule gas-fill retention.

2.4.1. NOVA Capsules Made Using PAMS as the Inner Mandrel

NOVA capsules typically have an inner diameter of 440 µm and consist of an inner CH mandrel, about 4-µm thick, overcoated with about 3-µm of PVA, which in turn is overcoated with 10 to 50 µm of GDP. The final diameter, dopants used in the GDP wall, and fill gas(es) are all defined by the requesting experimentalist. Originally, NOVA capsules were fabricated using polystyrene shells, made using drop tower technology, as the inner CH mandrels. These polystyrene shells were satisfactory; however, they had wall

thickness nonuniformities of Modes 2 and higher which may have adversely affected target performance.

We eliminated the inner layer nonuniformity issue in 1997, by substituting GDP shells as the inner CH mandrel in place of polystyrene shells. GDP mandrels, made by the depolymerizable mandrel technique, have excellent wall uniformity in all modes, resulting in NOVA capsules with improved wall thickness uniformity. Unfortunately, these GDP mandrels typically had a surface deformity, that appeared as a "lens", where the thin-walled shell touched the surface during pyrolysis to remove the PAMS mandrel. In addition, thousands of GDP shells were required for the low yield PVA-coating process necessitating numerous GDP coating runs, pyrolysis runs, and hundreds of hours of labor. The use of PAMS shells remedied these problems.

PAMS shells are made via the microencapsulation technique, wherein thousands of shells are made in each batch. The wall uniformity of NOVA-sized PAMS shells in Modes 2 and higher is excellent. However, PAMS shells made to date have about a 7-μm wall thickness; previous capsule requirements restricted the inner mandrel to 3 ± 1-μm wall thickness. We are working on producing thinner NOVA-sized PAMS mandrels. No further processing of PAMS shells is needed prior to PVA coating, a great time and labor savings. We found that drop-tower PVA-coating of PAMS shells was similar to that of polystyrene and GDP shells. Interferometric measurements of the completed NOVA capsules confirmed that they had excellent wall uniformity in all modes.

These shells may also have an improved AFM surface finish power spectra. Figure 2–13 below shows the AFM spheremapped outer surface power spectra of a typical NOVA capsule made using a PAMS inner mandrel as compared to a typical NOVA capsule made using a GDP mandrel. In the crucial low-order modes around 10, the capsule made using the PAMS inner mandrel is better than the capsule made using the GDP inner mandrel.

2.4.2. PVA Coating Development

In FY99, we performed a series of NOVA capsule PVA coating experiments that gave us a better understanding of, and thereby, control over the PVA coating process. Drop-tower PVA coating of 0.5 mm plastic NOVA capsules is a very low-yield process. Typically, only 2% or 3% of the shells injected down the PVA drop tower are of target quality. The reasons for this low yield include shell losses in the tower (only ~25% of the shells are recovered), incomplete coverage of the shell with PVA, too thin or thick a PVA layer, and/or a PVA layer that contains particulates, bubbles, or is excessively nonuniform in thickness.

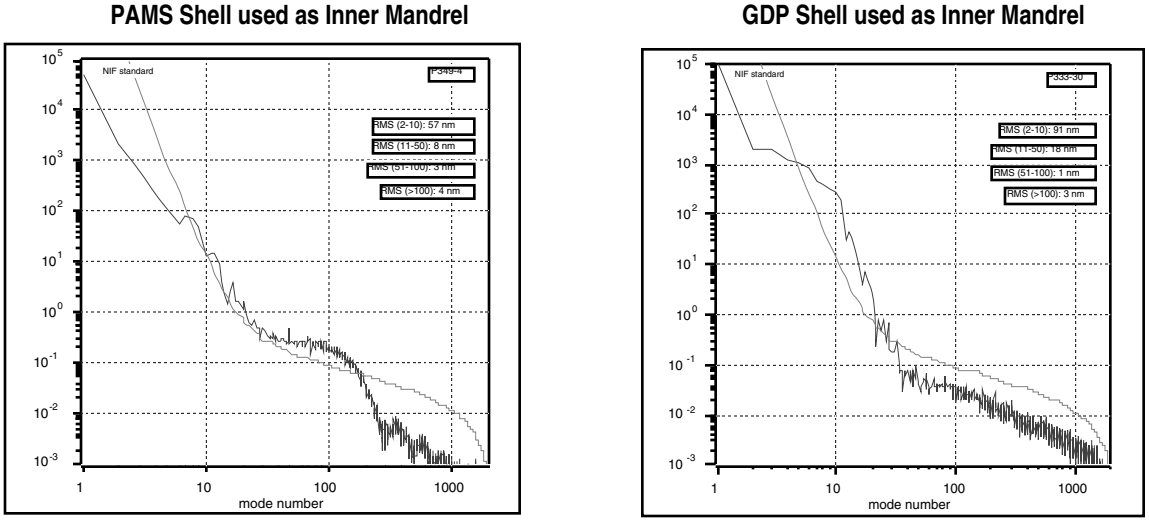

Fig. 2–13. Power spectra of typical NOVA capsules. The spectrum on the left is of a capsule made using a PAMS shell as the inner mandrel. The spectrum on the right is of a capsule made using a GDP shell as the inner mandrel. Note that in the important modes around 10, the PAMS mandrel capsule is better than the GDP mandrel capsule.

Of the many parameters affecting the PVA drop-tower coating process, we chose to examine the interaction of the stripping gas flow rate, the PVA solution concentration, and the injection nozzle temperature. For our initial experiments, we kept the solution concentration and stripping gas flow constant and varied the nozzle temperature of the shell injector. We injected the shells into the tower at a constant rate of about three shells per second. We found that the nozzle temperature had no significant effect on the resulting PVA coating as long as it was set below 30°C. Above 30°C, the PVA dried onto the end of the nozzle forming a tube, thereby causing shells to flow out of the tube in an uncontrollable fashion. We therefore eliminated the nozzle temperature variable and set it to 20°C for all our remaining experiments.

In our subsequent PVA coating runs, we found that by varying the stripping gas flow rate we could control the thickness of the resulting PVA coating for any given solution concentration. Indeed, the same coating thickness could be achieved with solutions of different concentrations as shown in Fig. 2–14 below. For example, a 2-μm thick PVA coating can be achieved either by using a 9.5% solution with a stripping gas flow rate of 6 ℓ/min or by using a 7.0% solution and a flow rate of 3 ℓ/min.

We also learned that the PVA solution concentration had a strong effect on product yield and quality. If the PVA solution was too concentrated (over 11%), the syrupy solution produced shells having excessive PVA thickness nonuniformity. If the PVA solution was too dilute, the maximum coating thickness was limited by the time it took the correspondingly larger droplet of solution covering the shell to dry as it fell through the drop tower. For example, in Fig. 2–14, note that the shells coated with a 7.5% PVA solution

and a stripping gas flow of 2.0 ℓ/min failed to dry completely and stuck to the collection plate.

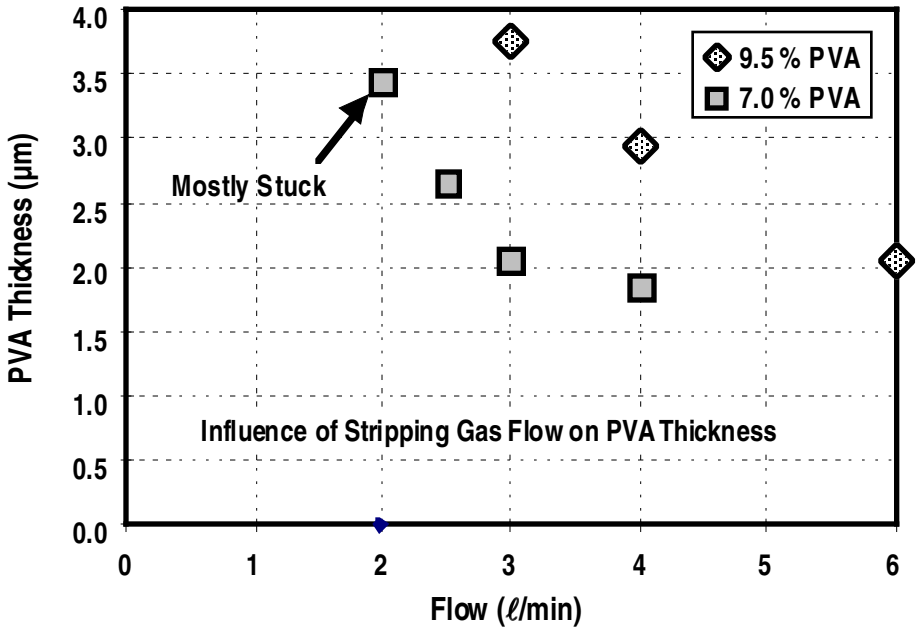

Fig. 2–14. Graph showing the influence of the stripping gas flow on PVA thickness for two concentrations of PVA in water solutions. Note that equivalent thicknesses of PVA can be attained with both solutions by controlling the stripping gas flow.

The knowledge we gained from these experiments, especially that of the importance of the stripping gas flow rate and the concentration of the PVA solution, will help us to further optimize NOVA capsule yield and quality in the coming years.

2.4.3. PVA Coating of Capsules for SNL's Z-pinch Machine

We improved the PVA dip-coating process for Z-pinch capsules enabling the capsules to hold hydrogen, deuterium, and argon for a time sufficient (over 24 h) for the capsules to be mounted and shot on Z without losing significant amounts of gas. At the same time, we improved the quality of the surface finish and the uniformity of the PVA layer.

Our initial attempts to PVA-coat Z-pinch capsules via the drop-tower technique were futile. Due to their large size, 1650 µm o.d. and 30 µm wall thickness, the shells fell so fast that the solution of PVA covering the shell was still liquid at the collection plate at the bottom of the tower. Increasing the tower temperature to its maximum (140°C) did not remedy the problem. Rather than redesigning the drop tower to be longer and hotter, we developed a dip-coating process for PVA-coating millimeter or larger capsules. This process consists of holding the shell with a vacuum chuck and dipping it into a PVA

solution resulting in coating approximately two-thirds of the shell. The shell is immediately inverted, so that the PVA solution will not form a hanging droplet on the coated side, and allowed to dry for about 10 minutes under a fiber optic light (heat) source. After the shell is dried, it is transferred to a second vacuum chuck that holds the shell at the pole initially dipped in the PVA solution. The shell is then dipped into the PVA solution a second time, the bare half of the shell coated, and allowed to dry under the fiber optic light source.

There were two problems with this PVA dip-coating technique: a vacuum chuck mark on the first PVA coating and a "roughened patch" at each pole of the coated capsule. The vacuum chuck mark on the PVA was left by the second vacuum chuck to which the shell was transferred after the first dip. We examined this vacuum chuck at high magnification and found that it had a roughened edge where it contacted the shell. We smoothed this edge using fine (600 grit) sandpaper. At the same time, we reduced the vacuum chuck suction to the bare minimum, just enough to hold onto the shell when it was dipped into and out of the PVA solution. Lastly, instead of transferring the shell to a second vacuum chuck after drying under the fiber optic light source, we dried the half-coated shell in a glass petri dish in an oven at 70°C overnight. We guessed that a more thoroughly dried PVA coating would be harder and less prone to deformation. To apply the second PVA coating, we oriented the shell on a plastic petri dish (static held the shell in place) with its PVA-coated side up, and picked it up at its top with the original vacuum chuck for the second dip. After applying these new measures, subsequent PVA-coated shells did not have the vacuum chuck mark.

The second problem we addressed was the roughened patches, about 200 μm in size (see Fig. 2–15), at each pole where the shell was dipped into the PVA solution. The patches only appeared after the shells were permeation-filled with hydrogen, deuterium, or diagnostic gases at temperatures ranging from 110° to 145°C. We conjectured that the patches were caused by water still in the thickest PVA coatings, found at the poles of the shell. To test this theory, we baked PVA-coated shells at 70°C for 20 h before we filled them at higher temperatures. The roughened patches no longer formed on the shells. Apparently, water in the PVA caused the surface of the PVA to roughen at the higher temperatures of the gas fills.

We also improved the argon technique for determining deuterium fill half-lives for SNL capsules. In this technique, a capsule's deuterium half-life at room temperature is determined by measuring its half-life for argon at an elevated temperature using our XRF system. The capsule's argon half-life is determined quickly by performing an overnight argon fill at 113°C and measuring the partial fill pressure achieved via XRF. The argon half-life is then correlated to the capsule's deuterium half-life at room temperature by using a factor previously derived from interferometric pressure measurements of

out-gassing NOVA capsules, that is, 3.2 × Argon half-life at 113°C ≈ deuterium half-life at 22°C.

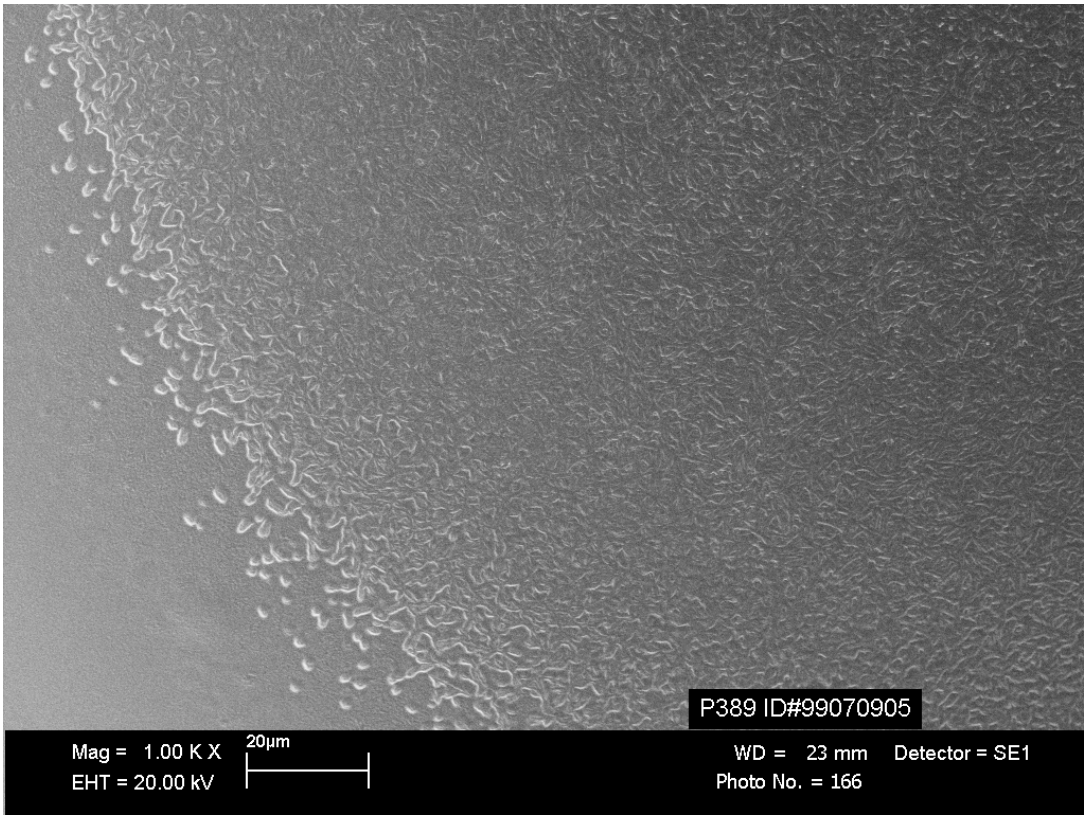

Fig. 2–15. SEM photomicrograph of the edge of the ~200 µm roughened patch found on a PVA dip-coated shell. The patch appears after the capsule is heated to 110° to 145°C for its gas fill. Drying the shell overnight at 70°C prior to the gas fill alleviates the problem.

In the case of large 1.6 mm SNL capsules, we found that due to the large size of the shell relative to the diameter of the XRF x-ray beam, the XRF counting error was high, on the order of 20%. This had a corresponding adverse affect on the calculation of a capsule's deuterium half-life. Rather than spending time and effort rectifying this XRF problem, we found a simpler solution. As the density of argon is almost an order of magnitude higher than that of deuterium, and because SNL capsules are so "large," the option of weighing the argon gas fill to determine a capsule's half-life became viable. To test this option, we filled some SNL capsules with 5 atm of argon at 145°C for 18 h. The weight gain was measured using our Cahn electrobalance that has a resolution of ±0.2 µg. Each capsule gained about 15 µg which is consistent with the predicted weight gain for the argon fill. The capsules were then emptied for 68 h at 113°C and weighed again. The calculated half-life of each capsule for argon at 113°C was then correlated to the deuterium half-life at room temperature using the NOVA multiplication factor of 3.2. The

results of the argon-weighing technique and its good agreement with capsule deuterium half-life measurements made by interferometry are displayed in Table 2–2.

TABLE 2–2
DETERMINATION OF SNL CAPSULES' DEUTERIUM HALF-LIVES AT ROOM TEMPERATURE USING A WEIGHING TECHNIQUE

Shell No.	Argon Fill Weight After 18 h At 145°C	Ar Weight After 68 h Vacuum Bake At 113°C	Calculated Ar Half-Life at 113°C	Calculated D2 Half-Life at 22°C	D2 Half-Life at 22°C (by Interferometry)
P401-1	15.3 µg	10.2 µg	4.8 days	15 days	14 days
P401-2	15.0 µg	10.3 µg	5.2 days	17 days	16 days
P401-8	13.1 µg	8.8 µg	4.8 days	15 days	14 days
P401-14	13.3 µg	8.9 µg	4.8 days	15 days	15 days

For further information, please contact D. Steinman (GA).

2.5. RADIOGRAPHY OF BERYLLIUM SEALS

LANL has taken the lead in developing the capability to manufacture beryllium capsules based on the machining of diffusion-bonded beryllium cylinders. We assisted LANL assess the quality of each step in the process. LANL machined a hemisphere into the end of a beryllium cylinder and mated it to another cylinder with a hemisphere machined at its end. To ensure better mating, a groove was machined near the edge of one of the cylinders and a mating ridge was machined in the other. The mating joint between the cylinders was coated with copper. The joint turned into a seal after applying heat and pressure.

LANL sent sealed cylinders and asked that we determine if a copper compositional gradient existed at the seal, how well the joints had turned into a seal, and whether the sphericity of the cavity was affected by the heat and pressure. Utilizing x-radiography and the National Institute of Health (NIH) image analysis program, we determined that a copper compositional gradient was present (Fig. 2–16) but becomes less pronounced after extended heat and pressure treatment, and that the joints were sealed near the edge of the cavity (Fig. 2–17).

To determine whether the sphericity of the cavity was affected by the heat and pressure, we modified our existing radiographic methods. The digitized x-ray image of a typical diffusion-bonded Be cylinder is shown in Fig. 2–18. Unfortunately, attempts to utilize the standard x-ray image analysis program routinely used on NOVA composite capsules were unsuccessful. The edge-finding routines which work so eloquently on the NOVA capsules fail on these images. Apparently the nonspherical asymmetry in the x-ray image caused by the presence of the joint and the cylindrical shape of the overall

component leads the edge-finding routine of the image analysis program astray. Instead of modifying the image analysis software program so that it would work on the digitized x-ray image, the digitized x-ray image of the cylindrical part with the internal spherical cavity was modified to work with the analysis program as written. This modification consisted of acquiring a digital image of a 2.000 mm sapphire ball (less than 0.5 µm OOR). The microscope setup and lighting conditions were then held constant and a digital image of the beryllium sample was acquired. Utilizing the NIH image analysis program, the image of the spherical cavity was electronically superimposed onto the image of the sapphire ball as shown in Fig. 2–19.

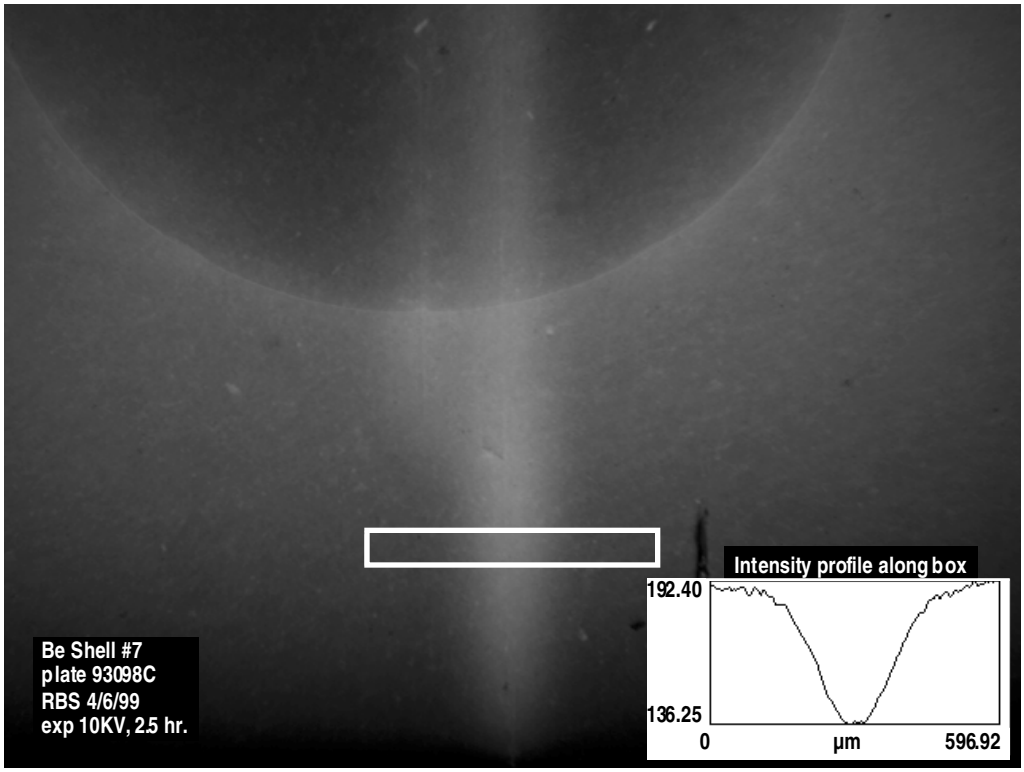

Fig. 2–16. The white streak in this radiograph is due to copper deposited on the joints before heat and pressure treatment. The densitometry trace in the lower right corner shows a more quantitative measure of the compositional gradient.

The radiography analysis program can easily locate and trace the edge of the sapphire ball. Since the sapphire ball is known to be round to less than 0.5 µm, a second derivative plot profile of a radial slice of the image allows analysis of the sphericity of the cavity to be made with ease. In the second derivative plot, the two lighter, humped peaks in the middle are an artifact of the image superimposition process and are a measure of how well the two images were superimposed upon one another.

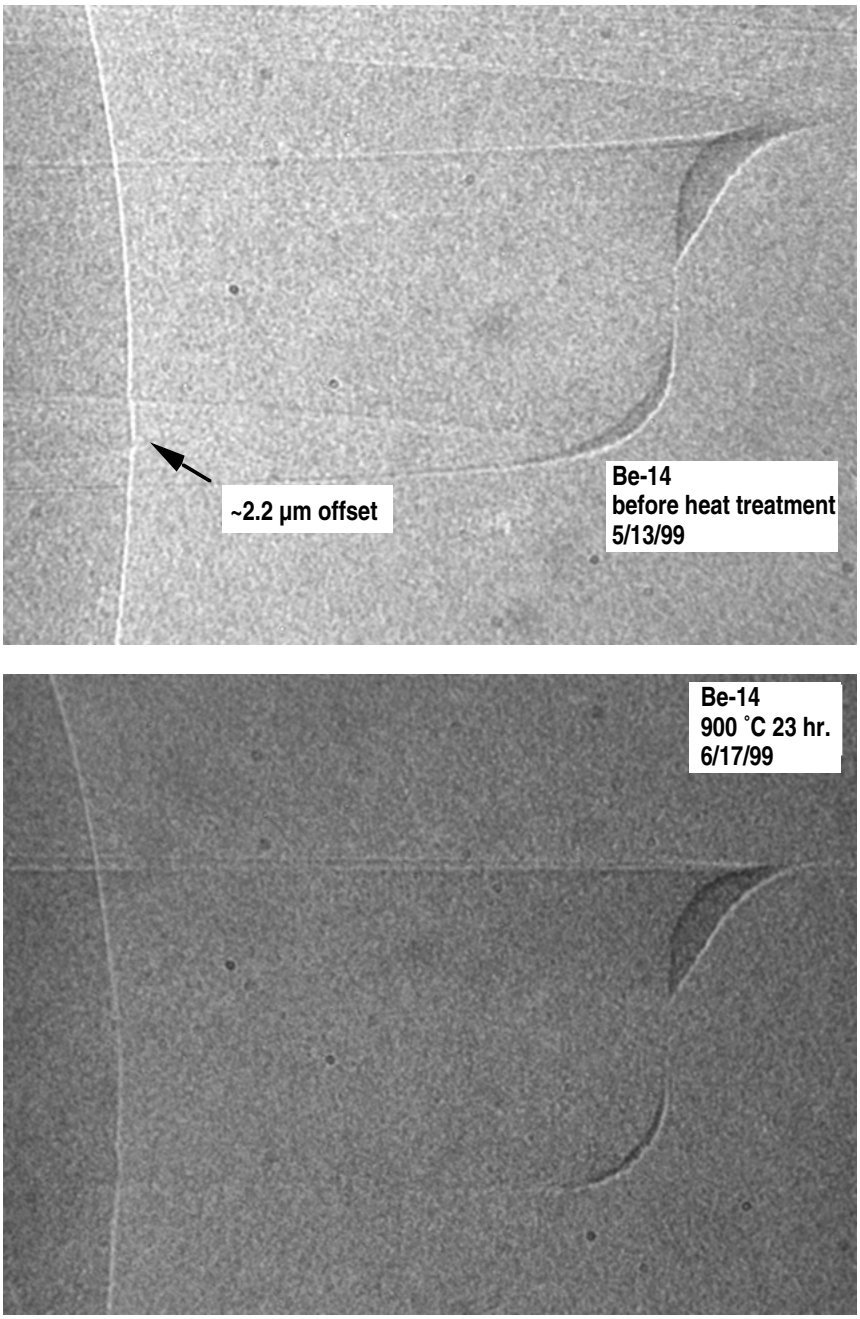

Fig. 2–17. These before (above) and after (below) radiographs show the effect of heat and pressure treatment on the mating joints. Although the groove and ridge did not mate well at the far edge away from the cavity, a seal was formed near the edge of the cavity. In practice, the poorly mated edge will be machined away to make a capsule.

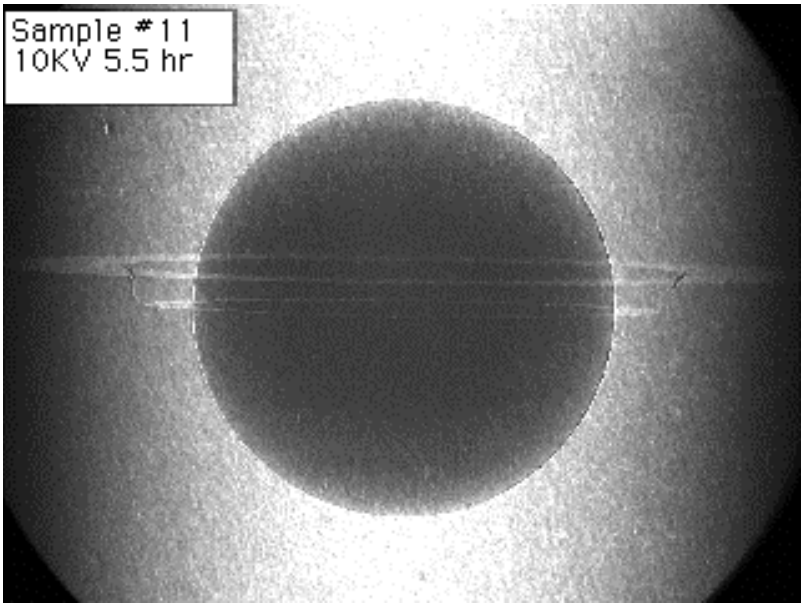

Fig. 2–18. The digitized x-ray image of a beryllium cylinder with a spherical cavity is not easily analyzed with our radiography analysis program without modifications.

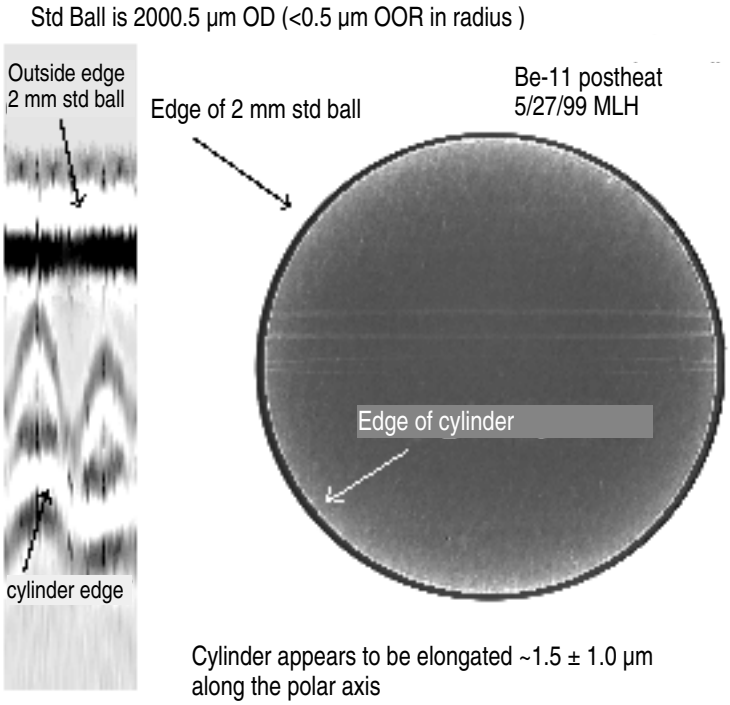

Fig. 2–19. The image of the spherical cavity is superimposed onto the image of the sapphire ball. The radiography analysis program easily finds the edge of the sapphire ball.

For additional information, please contact Dr. R. Stephens or Dr. M. Hoppe (GA).

2.6. POLYMER TARGET CHARACTERIZATION

Controlling surface fluctuations has been a continuing problem in shell production. This year we have substantially improved our ability to characterize those fluctuations, both on the surface and in the wall of the shell. We have added an optical wallmapper to our AFM spheremapper, and we have improved the routines with which we can visualize the spheremapper output.

2.6.1. Wallmapper

We introduced the technique of spectroscopic thickness determination of shell layers in last year's annual report [2–3]. In this report, we showed that an optical device produced by Filmetrics [2–4] could accurately measure shell thicknesses and described a fiber-optic/lens configuration which allowed it to be used on the AFM spheremapper without interfering with the operation of the AFM. In the intervening year, we turned it into a usable tool, and dubbed it a "Wallmapper." This required writing a routine, *Automeasure*, which linked the Wallmapper measurements to the shaft rotation angle, and a data analysis routine to pair up the surface profile and thickness data from each path in a meaningful way. The present Wallmapper system is still somewhat clunky in operation, but is good enough to give useful information and new insights that are not available from any other source.

Wallmapper Setup. The wallmapper is a slightly modified Filmetrics device. It runs from a laptop PC, which drives a separate light source and spectrometer through an interface card. We have added a digital IO card (INES i403) to the laptop to pick up the 0.1° pulses from the spheremapper's shaft encoder. The controlling software, *Automeasure*, uses a macro language built into Filmetrics' *Filmeasure* software to run the data collection process. It displays data as it is taken on an auto-ranging graph.

Wallmapper Data Collection. Thickness measurements are made immediately after an AFM trace is completed. It is only necessary to turn off the AFM, slow the rotation speed to 1/4 rpm, and start up *Automeasure*. Our current computer can only take one point every ~4 s, primarily for data analysis. To get sufficient data points, we collect 145 points over 3 rotations. After *Automeasure* has been started, it must be put into the background and *Filmeasure* brought to the front to minimize the analysis time.

Wallmapper Data Analysis. The data needs some massaging before it can be analyzed; data points are irregularly spaced and occasionally offset by a fixed amount (~250 nm for a typical 20-μm thick shell). After shifting and interpolation to correct those problems, it is smoothed to have a resolution of ~6°. On a good 2-mm diameter shell, the thickness resolution is ~20 nm.

Inner Surface Profile. The wallmapper data can be combined with surface profiles to give an inner surface profile. The AFM data must be smoothed to ~6° and interpolated to give data matching the wall thickness to enable subtraction. A typical set of data, taken from a bare PAMS mandrel on three orthogonal paths, is shown in Fig. 2–20(a), (b) and (c) and shows the outer surface profile, wall thickness variation, and inner surface profiles, respectively. For the surface profiles, Modes 0 and 1 (corresponding to average surface radius and center offset) have been zeroed. You can see that Mode 1 (surface NC) is the dominant mode for the wall thickness. The average power spectra for each of those sets of curves are shown in Fig. 2–20(d). The power spectra are not meaningful past ~30 since the resolution of the wallmap is ~ 6°.

2.6.2. Improved Spheremaps

We have utilized the capabilities of *Igor Pro* [2–5] to generate displays which give a better idea of the two-dimensional nature of shell surface perturbations. It can be done with our standard set of three mutually orthogonal paths (Fig. 2–21), but is more effective if we take a set of eight profiles rotated around a single point (Fig. 2–22). Within the program, these images can be set to rotate around any axis, and the magnification of the distortion can be changed to help understand the nature of the surface distortions.

For further information, please contact Dr. R. Stephens (GA)

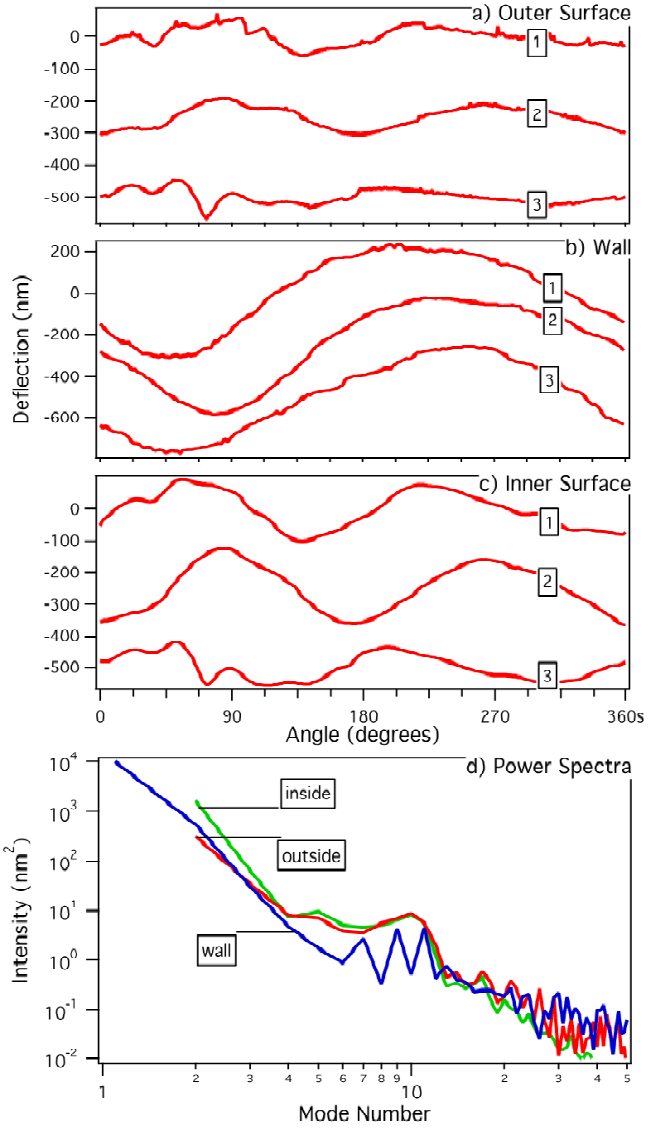

Fig. 2—20. Characterization of (a) outer surface profile, (b) wall thickness variation, and (c) (calculated) inner surface profile of a bare PAMS mandrel along three mutually orthogonal paths. Modes 0 and 1 have been zeroed in the profile curves and Mode 0 for the thickness variation. The average power spectra for each of the sets of curves are shown in (d). The power spectra are not meaningful past ~30 because the resolution of the wallmap is ~ 6°.

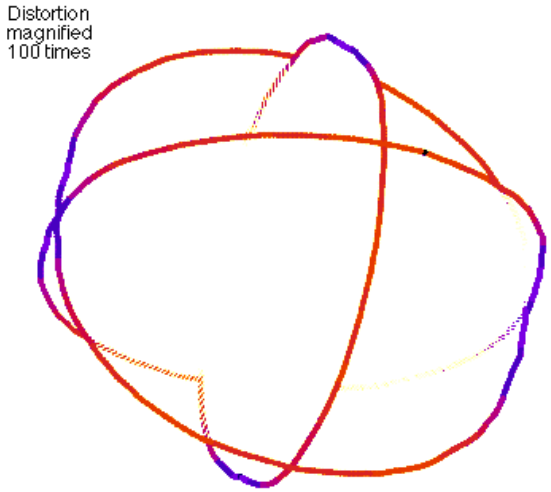

Fig. 2–21. Sphere plot of SiN ball with a flattened track on the surface. The distortion is magnified 100 times relative to the sphere size.

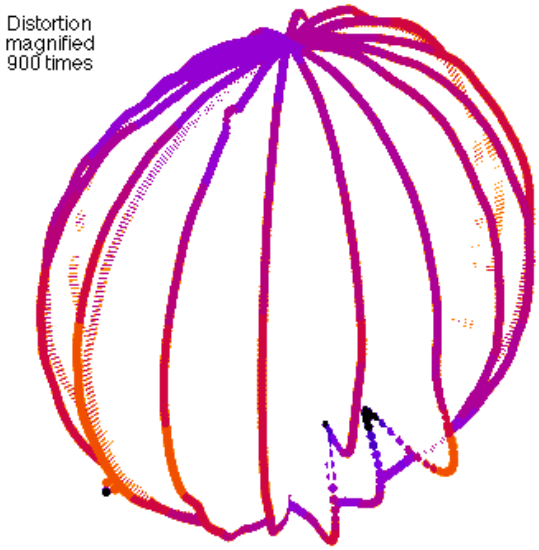

Fig. 2–22. Sphere plot of PAMS shell which was sheared during curing. The distortion is magnified 900 times relative to the 2-mm shell diameter.

2.7. REFERENCES FOR SECTION 2

[2–1] Raymond J. Roark and Warren C. Young, *Formulas for Stress and Strain* (McGraw-Hill Book Company, New York, 1975) 5th edition, p. 557.

[2–2] Project Staff, "Inertial Confinement Fusion Target Component Fabrication and Technology Development Support, Annual Report to the U.S. Department of Energy, October 1, 1996 through September 30, 1997," General Atomics Report GA–A22816 (1998) pp. 2-15 through 2-17.

[2–3] Project Staff, "Inertial Confinement Fusion Target Component Fabrication and Technology Development Support, Annual Report to the U.S. Department of Energy, October 1, 1997 through September 30, 1998," General Atomics Report GA–A22995 (1998), p. 2-16.

[2–4] Filmetrics F20 from Filmetrics, Inc., 7675 Dagget St., Suite 140, San Diego, California 92111, info@filmetrics.com.

[2–5] Igor Pro Version 3.0 by Wavemetrics, Inc., P.O. Box 2088, Lake Oswego, Oregon 97035.

3. MICROMACHINED TARGET COMPONENTS

During the present reporting period, numerous mandrels and flat target components were made as outlined in Sections 1.2 and 1.8. In addition to this work, three new types of components were machined: bimetallic witness plates, foam spheres, and plates with a conical cavity. Lastly, two modifications of the Rocky Flats Machine No. 3 were made. Only the new work and the machine modifications will be discussed in this section.

3.1. IMPROVEMENTS IN MICROMACHINING CAPABILITIES

The Rocky Flats No. 3 diamond-turning machine underwent two modifications during the past fiscal year that were designed to increase its productivity. The first of these improvements was the addition of an air turbine-driven milling attachment that is employed to make dicing cuts in the production of witness plates. The other improvement was the installation of a shaft encoder on the spindle axis to allow measurement and control of the spindle rotational speed. The installation of both the mill and the encoder required the design and construction of appropriate mounting brackets. The mill is fully operational at this time but the encoder is only useful as a tachometer; the spindle motor, which is an integral part of the blockhead spindle slide, is not amenable to the pulse-width modulation scheme employed by the control system. Either the motor or the feedback system will have to be replaced or modified before programmed speed control can be utilized.

3.2. BIMETALLIC WITNESS PLATES

Bimetallic witness plates are used to study the equation of state (EOS) of various materials at ultra-high pressure. These materials are applied as coatings to a portion of a stepped witness plate fabricated of material for which the EOS is well known. A shock wave is initiated in the witness plate by radiation incident upon the opposite side. By observing the arrival of the shock wave at the two steps and coating surface and using the known EOS for the underlying material, in conjunction with standard impedance matching techniques, it is possible to map out the ultra-high pressure Hugoniot of the material comprising the coating. During the past year, a number of bimetallic witness plates were fabricated and delivered to Lawrence Livermore National Laboratory (LLNL) for use in determining the EOS of iron (Fe) and tin (Sn). In the first case, a witness plate of aluminum (Al) supported a thin layer of Fe covering one-half of the lower tread as depicted in

Fig. 3–1. In the second case, the underlying witness plate was made of copper (Cu) and the coating was Sn.

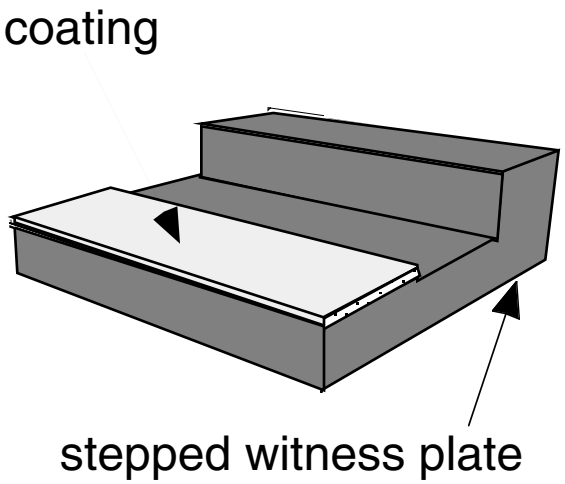

Fig. 3–1. Schematic for stepped witness plates used for EOS studies.

The various steps in the fabrication of these plates are depicted in Fig. 3–2, which shows the cross section through an annular region of a 64-mm diameter disc in which the profile of the witness plates is machined. This generic approach is described in previous annual reports [3–1,3–2]. The first step involves diamond-turning both faces of a 2-mm thick disc of Al or Cu and then attaching it to a mounting block with cyanoacrylate "super" glue as depicted in Fig. 3–2(a). The composite part is then remounted in the diamond-turning machine and after successive facing cuts have removed most of the unwanted thickness of the disc, equally spaced annular grooves are machined to a depth from the interface corresponding to the finished thickness of the lower step [Fig. 3–2(b)]. The composite part is then removed from the diamond-turning machine and mounted in the vacuum system of a sputter coater, which is operated to produce an 11 to 20-μm thick coating of either Fe or Sn on the entire surface as in Fig. 3–2(c).

After the coating procedure, the part is reinstalled in the diamond-turning machine and the unwanted portion of the coating is removed during the final machining of the witness plate profile [Fig. 3–2(d)]. These profiles are then diced in the plane of the figure and the resultant completed witness plates are released from the mounting block by dissolving the glue in nitromethane. Examples of Fe/Al bimetallic witness plates resting on a Roosevelt dime are shown in Fig. 3–3.

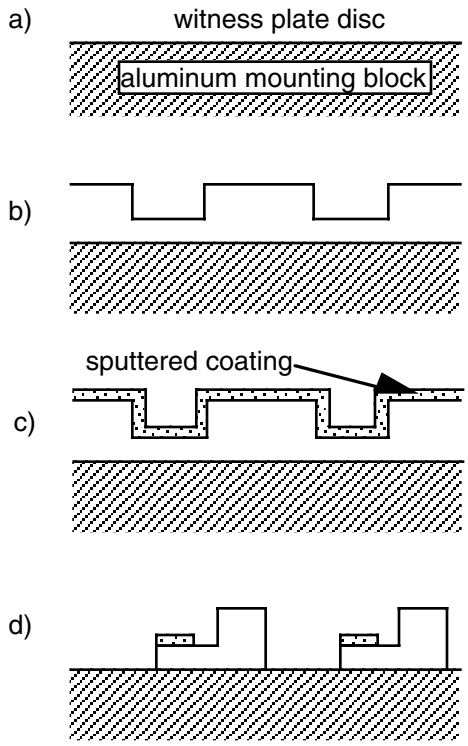

Fig. 3–2. The four fabrication steps used in the production of EOS witness plates.

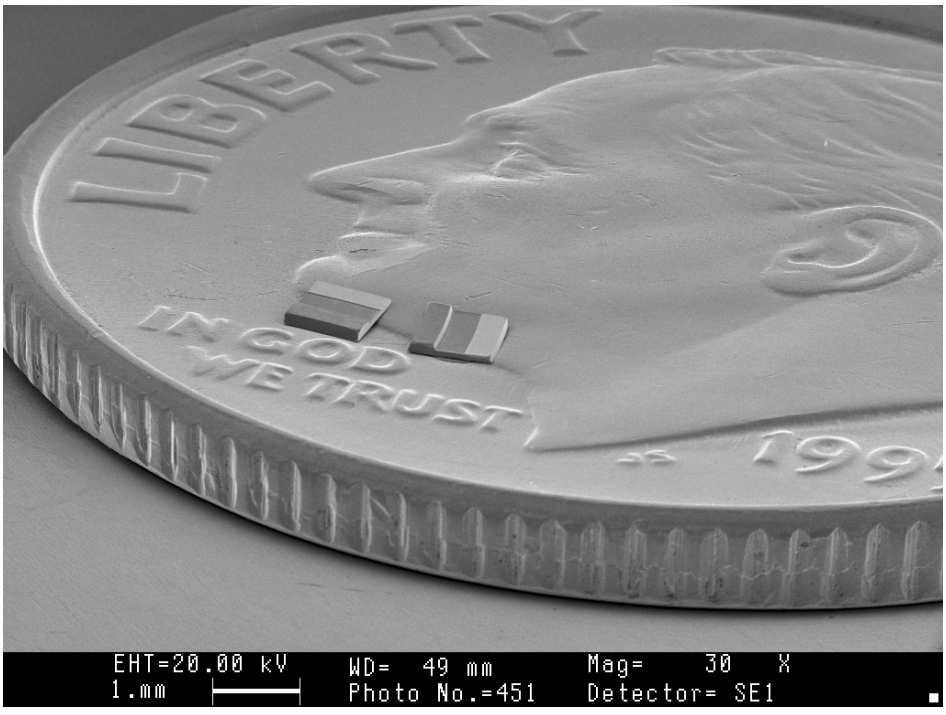

Fig. 3–3. An SEM photomicrograph of bimetal witness plates resting upon a coin.

3.3. SPECIALIZED COMPONENTS

The machining of conical cavities presents a special problem if the conical surface in the vicinity of the apex is of concern. Our diamond-tipped cutting tools are made with side relief angles varying from about 12˚ to 16˚, measured with respect to the symmetry axis of the tool point, in the horizontal plane. At first glance, it would seem that such a tool could be employed to cut a conical cavity provided that the included apex angle of the cone is greater than twice this value — or 24˚ to 32˚. However the end relief of the diamond tool is much less than this: it is 10˚ to 12˚, measured from the vertical, which means that it will interfere with the conical surface if the included cone angle is less than about 155˚ [or 180° – (2 × 12°)]. During the present reporting period, LLNL ordered a coin-shaped Fe component with a 120˚ conical cavity in one of the flat faces, which cannot be machined directly with our standard diamond tools due to this interference. We could, however, machine the complimentary (mirror-image) surface in a sacrificial mandrel upon which we could subsequently deposit Fe.

The first step in the fabrication of this part was to machine a Cu mandrel with a 120˚-included-angle cone protruding from its end surface as depicted in Fig. 3–4(a). The subsequent steps in the process were predicated upon three facts:

1. The thickness of the overall coin-shaped part was necessarily about 400 µm to accommodate the eventual conical depression.
2. Producing an Fe deposit 400-µm thick was not feasible with either sputter coating or electroplating.
3. The customer (LLNL) informed us that a 3-µm thick Fe coating upon any substrate would serve their purpose.

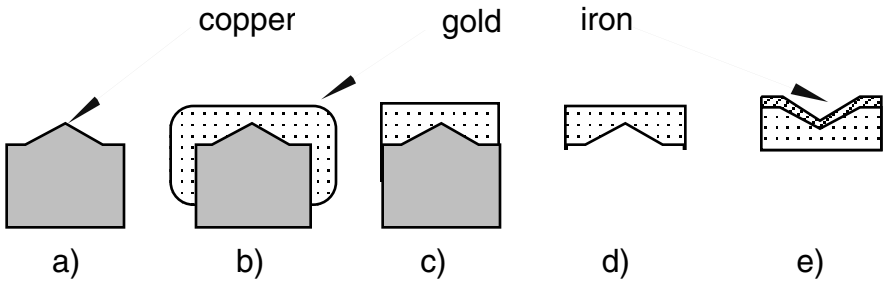

Fig. 3–4. Sequence of fabrication steps for producing conical Fe buttons.

With these facts in mind, the Cu mandrel was subsequently electroplated with gold to a thickness exceeding 400 µm [Fig. 3–4(b)], then reinstalled in the diamond-turning machine for finish machining on the outside diameter and end [Fig. 3–4(c)]. The finish on these surfaces is unimportant. In the next step, the Cu was etched away [Fig. 3–4(d)],

and a 3-μm thick Fe coating was sputtered upon the surface of the gold button containing the conical depression [Fig. 3–4(e)].

3.4. FOAM SPHERES

Spheres micromachined from polystyrene foam were ordered by Sandia National Laboratory (SNL) during this reporting period to be used to study, among other things, the partitioning of x-ray heating in the Z-pinch. The bulk polystyrene foams were made by Diana Schroen-Carey. The process for making the SNL foams is similar to the published LLNL and Los Alamos National Laboratory (LANL) techniques, but with three adaptations that tailor the foams to SNL's specific needs. First is the elimination of the sodium persulfate as the radical initiator because it adds oxygen to the polymer structure, which interferes with some of the SNL diagnostics. Next, a higher percentage of organic material is incorporated in the emulsion, which softens it and makes it easier to cast into the required cylindrical shape. Finally, the processing techniques were modified to accommodate the more viscous solution. Approximately 125 ml of foam was mixed and cast in each batch, then weighed and radiographed to confirm density and uniformity.

Although this polystyrene foam is very machinable, it is also very friable, meaning that it cannot be handled in the usual manner. This foam has connected porosity, which suggests that it could not be mounted in a vacuum chuck; this preliminary conclusion was incorrect as initial trials proved. In fact the limiting pressure that could be utilized was not determined by the conductance of the pores but by the structural integrity of the bulk foam. Indeed, unless the pumping speed of the port leading to the vacuum chuck was limited, a "divot" was produced in the surface of the sphere. Even with less suction, an impression of the chuck was left in the foam material; this "ghost" gradually healed over a period of an hour or so after completion as did a similar ghost left by the rubber-tipped vacuum tweezers used in handling the foam parts.

A brass vacuum chuck adapter was made for the purpose of holding the foam during the machining of the sphere as is shown schematically in Fig. 3–5. This adapter was made on a standard machine lathe then mounted on the vacuum faceplate of one of our diamond-turning machines where the outside diameter, end, and reentrant conical surface were turned; these surfaces are indicated by the arrows in the figure. Since these three surfaces are turned in the same setup, they are assured to be concentric and perpendicular with the spindle axis of the turning machine and can be used as reference surfaces for subsequent tool touch-off. The included angle of the reentrant conical cavity on the end of the adapter is 90°, a value which must be accurate to allow precise calculation of the location of the equator of the sphere with respect to the end of the adapter. It is important that the diameter of the base of the conical surface not exceed the diameter of the sphere that will be machined from the foam blank.

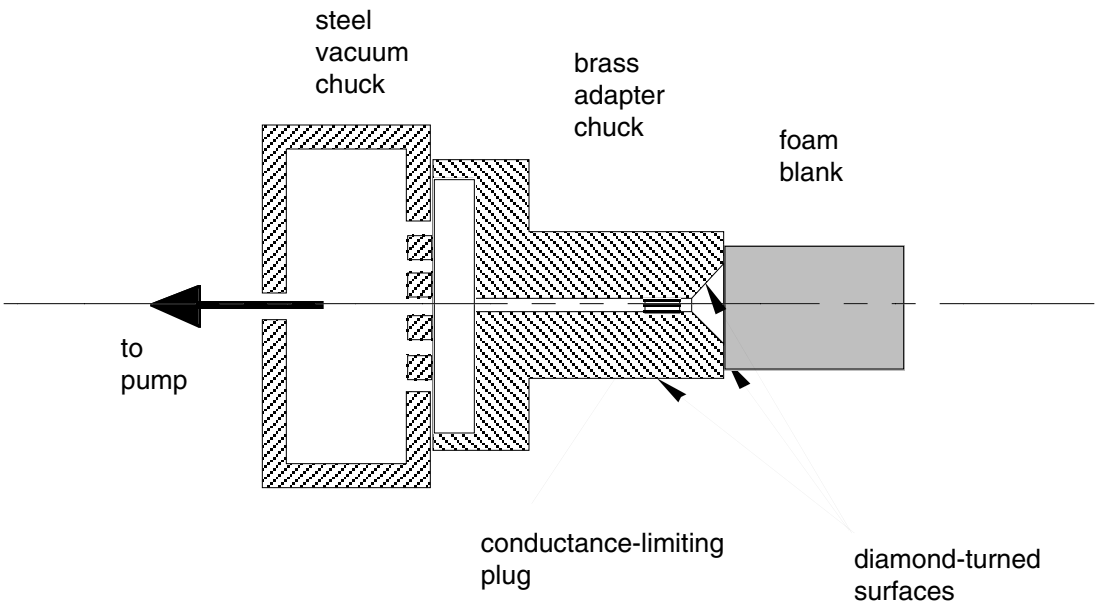

Fig. 3–5. Schematic of vacuum adapter chuck for holding foam pellets during machining.

The machining process has four steps as indicated in Fig. 3–6. In the first of these steps [Fig. 3–6(a)] the foam blank is mounted upon the vacuum adapter which is accurately located on the spindle centerline. The outside diameter of the blank is machined along with a hemisphere on the end [Fig. 3–6(b)]. Great care must be given to the next step in which the blank is flipped end-for-end and repositioned in the vacuum adapter [Fig. 3–6(c)]. Not only must it seat accurately in the micromachined conical cavity, but also the axis of the foam cylinder must coincide with the spindle axis, *i.e.*, the cylinder must not be cocked. These assurances are necessary to place the equator of the first hemisphere perpendicular to the axis of the spindle. The axial position of the equator can be easily calculated from the geometry of the hemisphere and the conical cavity, allowing the second hemisphere to be machined as indicated in Fig. 3–6(d). A completed 5-mm diameter polystyrene sphere is shown in Fig. 3–7. This is one of the original seven micromachined foam spheres shipped to SNL during this reporting period.

For further information, please contact Dr. J. Smith, Jr. (GA)

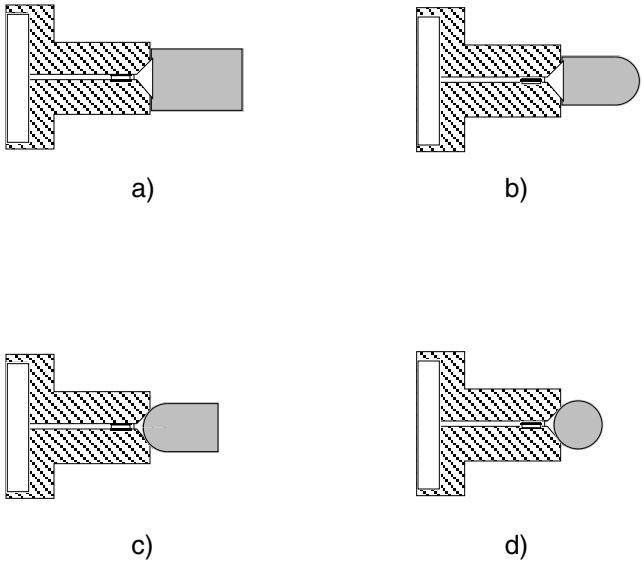

Fig. 3–6. Four-step process for machining foam spheres. A cylindrical foam blank is held on the front of the vacuum adapter for machining of the o.d. in (a). In (b) a hemisphere is machined on one end. In (c) the blank has been reversed in the adapter and the final hemisphere is machined in (d).

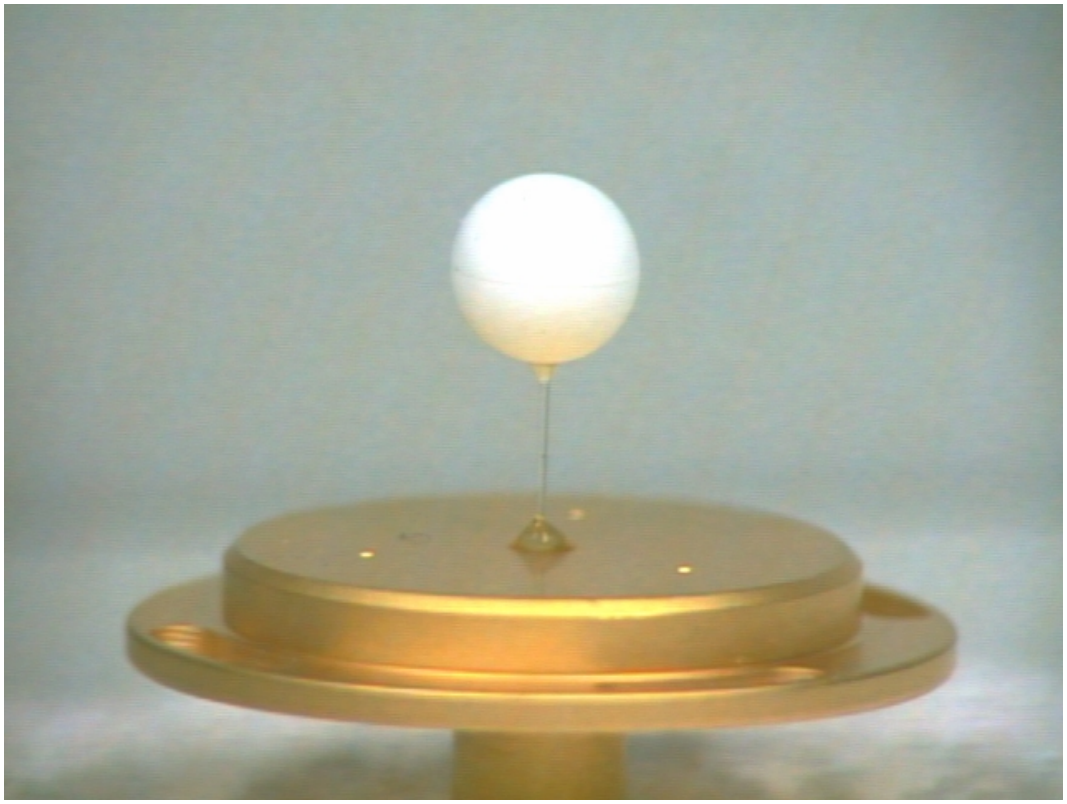

Fig. 3–7. A completed foam sphere supported on a fiber attached to the flange.

3.5. LOW-DENSITY FOAMS PRODUCTION

The production of low-density foams was one of two subtasks of 99SL02. (The other subtask, On-Site Support for Target Fabrication, is reported in Section 1.9.) FY99 is the third consecutive year that SNL has requested a subtask designated solely to produce low-density foams. The task statement specified "foams will be of various geometries, densities, and polymer. About two hundred fifty (250) target components will be required." This task statement reflected the increasing number of uses for low-density foams on the Z-machine. Previous task statements had specified only cylinders and annuli, typical target component geometry. The FY99 statement was broadened to include foam geometries that could be used to prevent premature closure of diagnostic holes or improve pinch uniformity by filling holes in the current return can. These foams tend to be 1 mm or less in thickness, can be squares, circles or ovals, and tend to be 15 mg/cm^3 or less in density. The large number of foam components requested in the task statement anticipated that many targets would contain several foam components of the various types. That anticipation was correct but the number required was severely underestimated due, in part, to SNL's fielding of a number of target designs that contained in excess of 20 foam components. In total, we delivered 480 foams for the year. This marked the second year in a row that we were asked to significantly exceed the task statement (see Fig. 3–8).

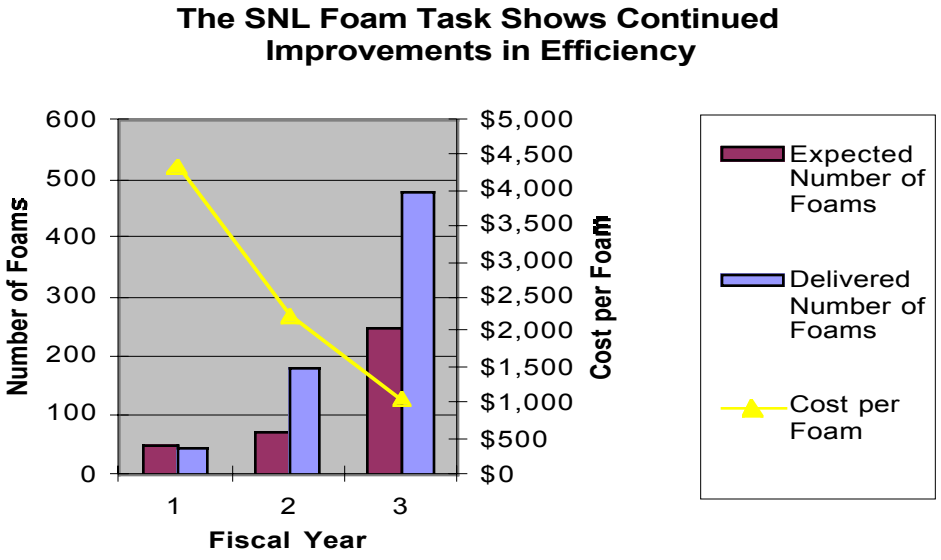

Fig. 3–8. In its third fiscal year, the SNL foam task continues to increase the number of foams produced and decrease the cost per foam. The cost per foam indicated is obviously an average. The actual cost can vary significantly depending upon geometry, dimensional tolerances, and density.

SNL recognized that their expectations clearly exceeded the standard production techniques and required development and, subsequently, funded developmental purchase

orders in FY97 and FY98. Without those purchase orders, the progress in productivity and quality could not have been made. We are not going to report in detail upon the developmental work in this report, but the foams produced under the Inertical Confinement Fusion contract are all being made by the processes developed under those purchase orders.

In spite of the increased number of delivered foams, we were able to significantly improve the quality of the foams produced. SNL assisted in the quality control by radiographing the foam components prior to assembly. We replaced all foams that showed any discernable nonuniformity. In addition to monitoring density uniformity, the dimensional tolerances were often tightened from previous years. For example, we delivered one order of 22 foam cylinders 6-mm tall, 6-mm o.d., and with a density of 10 mg/cm^3. The most difficult tolerance was an average parallelism of the two ends to within 60 μm. Another quality control improvement was the use of a confocal microscope obtained in FY99 with capital equipment funds. The confocal is often useful in determining flatness and parallelism of a component and allows us to make inferences about density uniformity. While we are not able to see bulk densities with this microscope, we can determine cell size and scan various areas to confirm consistent cell size. We can also gain important morphology information.

The confocal microscope has not been routinely used for determining cell size, so the first step in making it a useable tool was to understand how its images compared to the more routinely used scanning electron microscope (SEM) images. The most notable distinction between the two types of images is the depth of field. The SEM has a very deep depth of field, thus SEM images tend to understate the cell sizes when the eye is fooled into seeing all visible polymer as being at the same approximate depth. The confocal depth of field is designed to be short, approximately 2 μm for our microscope (see Fig. 3–9). This turns out to be an advantage when trying to determine cell size since only a thin layer of the foam is visible. The confocal images give a much more defined 3–D representation.

Having defined the depth of field, we examined TPX (commercial designation of the polymer produced by the polymerization of 1-methyl-4-pentene) foam made from the new procedure (shown on the left in Fig. 3–10) versus TPX made by Oak Ridge National Laboratory (ORNL) (shown on the right). The foam on the left shows a net-like structure filling the entire area. The foam on the right has a plate-like structure that tends to cover some areas more completely than others. We believe that it is this net-like structure that is responsible for the improvement in density uniformity.

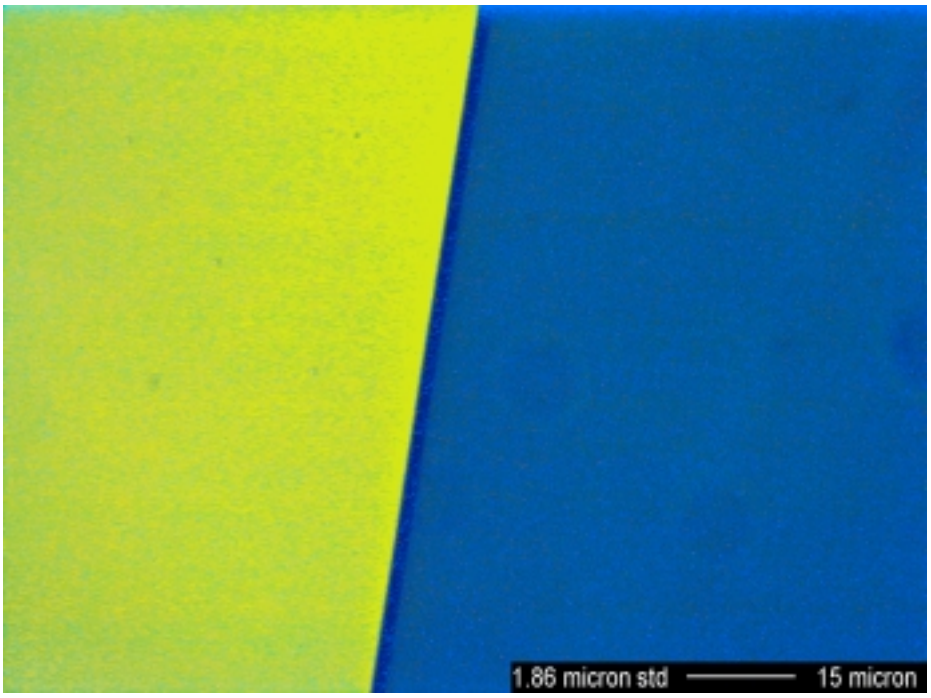

Fig. 3–9. This is an image of a 1.86 μm step standard. The light area is 1.86 μm taller than the dark. This photograph demonstrates the useable depth of field for our microscope is just slightly greater than 1.86 μm.

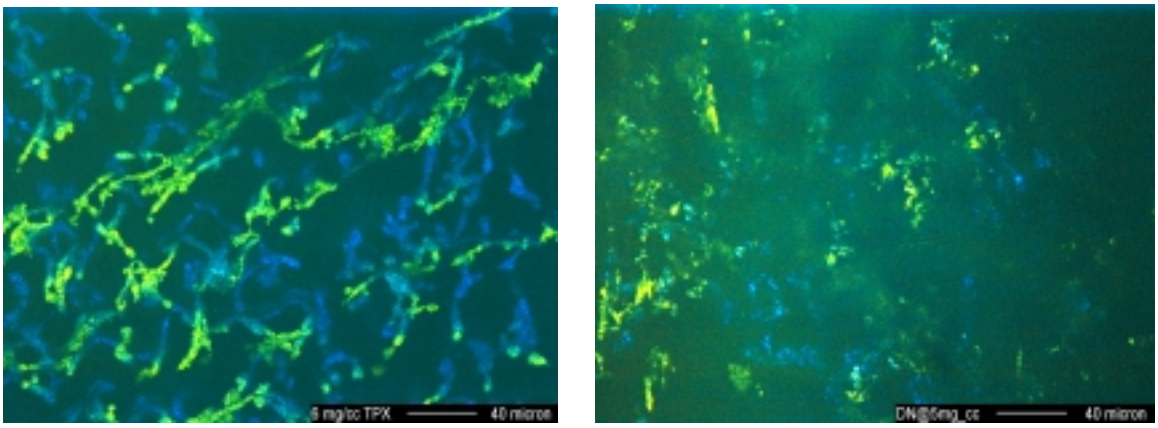

Fig. 3–10. The foam on the left was produced using the current procedure developed specifically for SNL's needs. The foam on the right was produced by ORNL. There is a slight difference in density between the two foams, but the difference in morphology between foam types is seen for other densities as well. The net-like structure on the left appears to cover the entire volume more evenly and both ion microtomography and radiography have confirmed higher density uniformity for this type of foam as compared to the ORNL type.

The majority of foams made for SNL are TPX, but polystyrene is also very important. We have modified the process for making polystyrene foams from the published LLNL and LANL techniques to tailor the foams to SNL's specific needs. For example, we do not use sodium persulfate as the radical initiator, which adds oxygen to the polymer

structure. (Oxygen causes an opacity problem with some of SNL's diagnostics.) The replacement radical initiator is a low temperature, oxygen-free, Azo initiator.

One particularly challenging target component was a 5-mm sphere. We began production by trying to cast the foams into spherical shapes, using both polystyrene and TPX systems. After repeated casting failures, we asked General Atomics (GA) to attempt to machine spheres out of bulk foam specimens. They were successful as described in Section 3.4 above.

For further information, please contact D. Schroen-Carey (Schafer Corporation).

3.6. REFERENCES FOR SECTION 3

[3–1] Project Staff, "Inertial Confinement Fusion Target Component Fabrication and Technology Development Support, Annual Report to the U.S. Department of Energy, October 1, 1996 through September 30, 1997," General Atomics Report GA–A22816 (1998) p. 3–3.

[3–2] Project Staff, "Inertial Confinement Fusion Target Component Fabrication and Technology Development Support, Annual Report to the U.S. Department of Energy, October 1, 1997 through September 30, 1998," General Atomics Report GA–A22995 (1998), p. 3–1.

4. PLANAR TARGET DEVELOPMENT

During this year, the task descriptions and requests for targets for the NIKE and OMEGA laser programs have been similar to those of previous years except for the increased emphasis on foam targets for the Naval Research Laboratory (NRL). Throughout the year, both NRL and the University of Rochester/Laboratory for Laser Energetics (UR/LLE) have refined their target requirements and have requested new types of targets that require rapid development of production techniques.

4.1. NIKE LASER TARGETS

NIKE target requirements have increasingly shifted toward cryogenic targets. During FY99, over half of the targets we shipped to NRL have been mounted on cryogenic target mounts (CTMs) rather than polymer NIKE target frames. The targets have also become more and more complex. More of the targets have patterns imposed on one surface, multiple layers of polymer and metal, and complex geometries.

Many of the targets we have delivered to NRL have been classic flat-film polymer targets mounted on polycarbonate frames (Fig. 4–1). Nearly all flat-film polymer targets are made with polystyrene that we cast to precise specifications. Target thickness is usually required to be within 1 μm of a nominal thickness that can range from 10 μm to well over 100 μm. The thickness of each target must be uniform over the entire area of interest and must be reported with a precision of one-tenth of a micron. The surface must be smooth with no inadvertent perturbations greater than 25 Å measured peak to valley (P-V). The films must also be very flat when mounted with maximum allowable curvature of 1 μm over 1 mm laterally. We are able to consistently produce flat, smooth films by casting polystyrene on a flat substrate, usually a silicon wafer. After the polystyrene dries into a stiff film, it is annealed at 100°C for about 2 days to remove stresses in the film.

Flat film targets have been delivered with sinusoidal and step-ramp patterns impressed on one side of the film. We make these patterned films by casting the polystyrene on a patterned mold, usually made of silica. Molds with a range of patterns are available and will be discussed in Section 4.1.3.

We have used one or the other of two primary methods for adding metallic coatings to polymer films if the specifications dictate. For thicker coatings (above about 100 Å) of aluminum or gold, we use evaporative coating. Our evaporative coater uses a resistively heated tungsten filament that consists of several strands of wire. We load the coater by

melting the appropriate metal into the filament. The film that is to be coated is placed inside the vacuum chamber behind a shutter to protect it from the heat of the filament. After the chamber is evacuated, the filament is heated with a predetermined level of electrical current. When the filament reaches the proper temperature, the shutter is opened for a time that corresponds to the thickness of the metal that is to be deposited. Coated layer thickness is characterized by using an interferometer or a profilometer to measure the thickness of film deposited on a witness plate. The other method we use for coating films with metal, particularly for thin layers, is a sputter coater. With the sputter coater, the thickness of the film can be monitored as the film is deposited. After deposition, we confirm the thickness of the deposited layer using the same techniques as we use for characterizing evaporated films.

Fig. 4–1. NIKE target frame with a polymer film target.

Most of the targets NRL requires are designed to work in a cryogenic environment. The targets have various configurations, but usually have certain things in common. All the cryogenic targets we made for NRL during FY99 consisted of an aluminum CTM (Fig. 4–2) and most had a covering of polyimide film.

The simple polyimide films for the NRL targets have been obtained commercially or spin-cast in our Schafer Corporation laboratory. The films ranged in thickness from 50 nm to more than 70 µm. Multilayer films have also been produced and assembled into NIKE targets. Films of three layers of polyimide (each 0.5-µm thick), interleaved with three layers of gold (each 20-nm thick), and films of ten layers of polyimide (each 0.15-µm thick) interleaved with ten layers of gold (each 6-nm thick) were developed for NIKE targets (Fig. 4–3). The polyimide layers were formed by spincasting enough

monomer onto a 10-cm diameter silicon wafer to produce a layer of the polymerized material 0.15-µm thick. After the first layer was cured in an oven following spin-casting, a 6-nm layer of gold was sputtered onto the polyimide. The process was then repeated over and over until all 20 layers were deposited. We have regularly deposited four layers, two polyimide and two gold per day. However, sometimes other tasks interfered and we only managed one pair of layers per day. Thus, it required between one and two weeks of elapsed time to produce one 20-layer film, 1.5 µm total of polyimide and 60 nm total of gold. It should be noted, however, that the film-making processes proceeded in batches so that as many as ten or more wafers were in the process at a time so that the long-term average was several completed films per day.

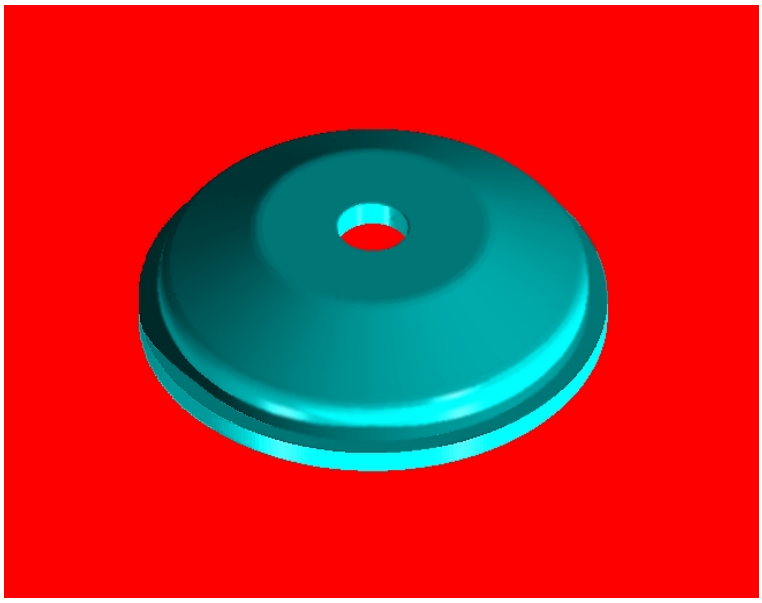

Fig. 4–2. Aluminum CTM.

The multilayer films as well as uniform polyimide single-layer films 1.5-µm thick were stretched over the conical surfaces of the CTMs to serve as NIKE targets. Many of the 1.5 µm polyimide films were coated, after mounting on the CTMs, with layers of gold or aluminum a few tens of nanometers thick.

We have made significant improvements to the quality of the polyimide we spin-cast at Schafer. By enclosing our spin-casting equipment in a laminar flow clean room, the amount of dust has been reduced greatly. Refinement of the temperature profile for curing the polyimide and utilization of prime grade silicon wafers has improved the homogeneity and quality of the film as well, particularly for films with around 1.5 µm thickness.

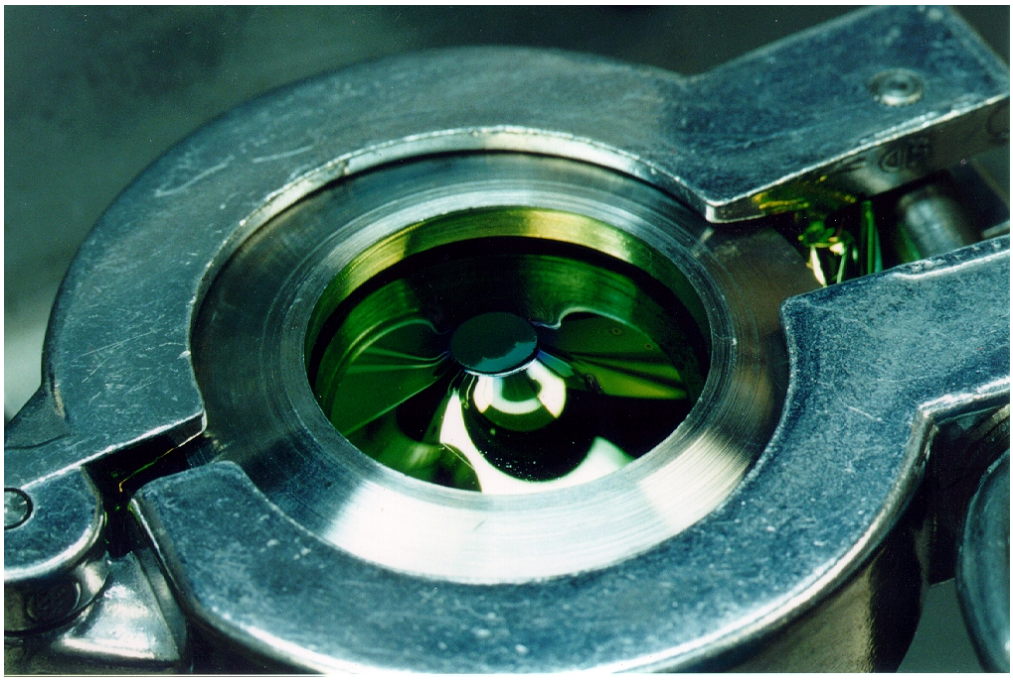

Fig. 4–3. Twenty-layer gold polyimide film being stretched over a CTM.

During FY99, NRL requested polyimide films with a sine wave pattern impressed on them. We tried several methods for making polyimide films with patterns. Less successful were attempts to impress a pattern on partially polymerized film that had been cast on a flat substrate. This method was unpredictable because the depth of the resulting pattern could not be controlled. We were more successful spin-casting the polyimide directly on a patterned mold. This method has disadvantages — the patterned molds are small (2 in. diameter compared to 4 in. diameter for flat wafers) and the molds are very difficult to clean after the casting is removed. Spinning the polyimide on patterned molds does, however, result in film with a reliable replication of the desired pattern. The films are not flat on the top as are polystyrene films cast on patterned molds; they have approximately the same pattern replicated on the side of the film that is away from the mold. This results in a corrugated film that is useful for making foam targets with patterned surfaces. This technique will be discussed more thoroughly in Section 4.1.4.

4.1.1. Equation-of-State (EOS) Targets

This year, we continued to produce equation-of-state (EOS) targets for NRL. EOS targets consist of parallel machined aluminum plates accurately separated by spacers. The assemblies are mounted on a polymer film attached to a CTM. Typically, the aluminum plates are 2.5-mm squares machined to provide diagnostic ports in one plate, integral spacers along two edges to assure proper spacing and parallelism, and a central groove on one plate (see Fig. 4–4). The spacers are machined into the base plate to make

assembly easier and more precise. Of the three diagnostic ports (oval holes approximately 75-µm wide by 150-µm long) in the witness plate, two are open all the way through so that the base plate can be observed. The third port is covered on the bottom with an opaque material. We have developed techniques and procedures for making covered holes that fit NRL's rigid requirements for flatness.

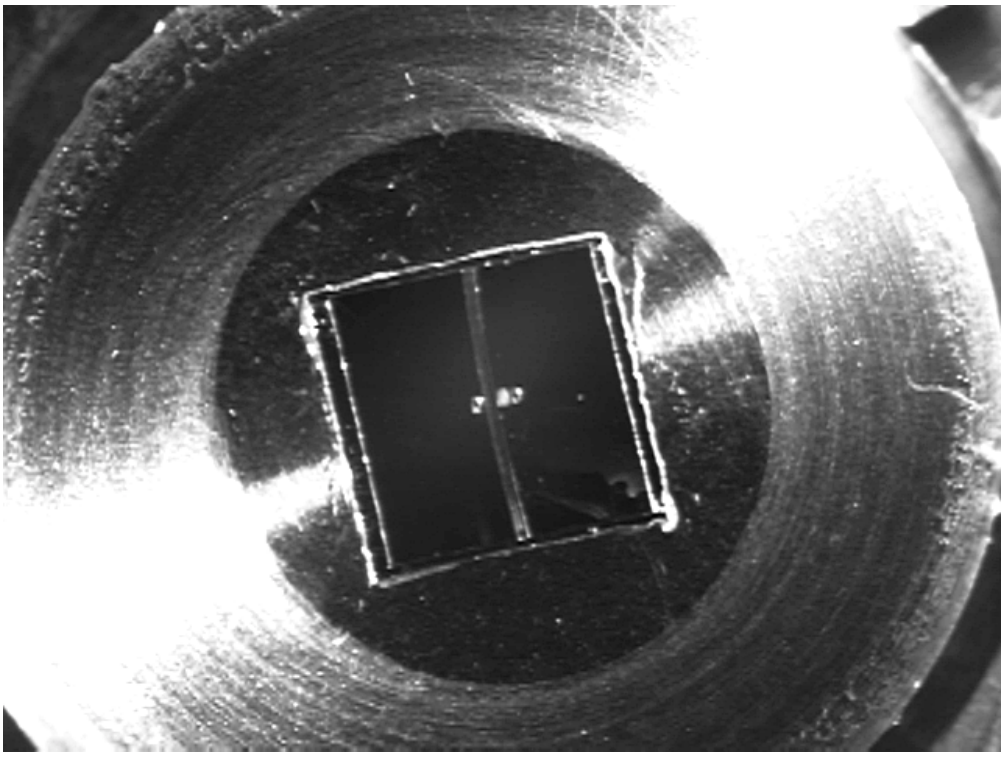

Fig. 4–4. EOS target viewed from the top (back side from the laser's point of view). This top plate is mounted 60 µm above another aluminum plate. Notice the 20-µm deep groove down the center of the plate and the three holes for diagnostics.

The EOS targets that we delivered to NRL this year were manufactured with a technique that was developed through close cooperation and collaboration between Schafer and NRL. We machined the witness plate blank (there are about 36 witness plates on one machined disk) and marked the position of the groove on the disk, but the groove was not machined into the piece until later. Three holes were drilled in each witness plate and the center hole for each plate was filled with a clear polymer. When the polymer hardened, the back face of the disk was machined to make the polymer surface even with the aluminum surface of the disk. The disk was then coated with 200 Å of aluminum to serve as an optical barrier. This covered the filled hole but left the other two holes open. The disk was then turned over and excess material removed from the front side and the groove was machined into the surface. The top plates were then cut apart, characterized and mounted onto the spacers above bottom plates. This procedure worked fairly well,

but sometimes, the polymer surface did not stay even with the aluminum surface. The requirement for multiple machinings and coating reduced the reliability of the process. We have worked on a technique for applying thin foil to cover the proper hole on the witness plates. We believe that this technique will result in better consistency of quality and will reduce manufacturing time.

The specifications for EOS targets were similar to those for the year before. Diagnostic holes were slotted (nominally 75-μm wide by 150-μm long). Surface finish specifications limit P-V roughness to be less than 10 nm. The plates and their surfaces were specified to be parallel to 1 milliradians or better. Plate curvatures less than 0.1 μm/mm were required.

Diamond-turning techniques were utilized to produce the very smooth surfaces of the upper and lower plates. A method of drilling the diagnostic hole was needed which did not work harden the surrounding metal, deform the plate, or leave burrs around the holes. Since mechanical drilling and milling operations tend to both deform the material and leave entry and exit burrs, we utilized an electrical discharge machining (EDM) capability.

4.1.2. Micro Electrical Discharge Machining Apparatus

Conventional mechanical microdrilling and milling techniques tend to leave defects at hole edges in the planar parts used as witness plates in the EOS targets. The defects are extremely difficult to remove without inducing additional distortion or altering the grain structure of the material. To minimize the likelihood of producing target parts that did not meet specifications because of burrs and/or material deformation, we developed, entirely with on-hand Schafer Corporation materials, an EDM apparatus for producing the diagnostic holes consistent with design specifications [4–1]. The apparatus we assembled not only allowed us to produce the necessary holes, but has provided us with other capabilities as well.

Among our micro-EDM capabilities, all of which are of use in producing the NIKE EOS target witness plates, are:

1. Drilling — Round holes through materials susceptible to EDM. Minimum diameters are limited by the size of tool (wire) obtainable and our abilities for aligning it in its mount. Maximum diameters are limited by the strength and size of the machine.
2. Drilling — Irregular (nonround) holes through materials susceptible to EDM. Subject to the same limitations and those associated with producing the shaped tool and the need for a few microns clearance between the side of the tool and the material being machined.

3. Slotting — The production of holes of predetermined length and consistent width. This capability is used to accurately cut the plates for the EOS targets to their final dimensions (2.5-mm square).

4. End milling — As a special case for those operations described above. Micro-EDM end milling is performed with our machine to remove material from the lower plates of the EOS targets to produce the four integral spacers at the corners of the plate on which the upper plate rests and is cemented.

The operation of our micro-EDM apparatus is similar to that of all EDM machines in that a current is made to flow between an oscillating, electrically conducting tool and a material susceptible to EDM in a dielectric liquid. Typical values for the voltage between the tool and the material to be machined range from approximately –12 to +12 V. Excitation frequencies have ranged from about 200 Hz to 1.5 kHz.

The mode of oscillation of the tool can be controlled by choosing an appropriate excitation frequency for the micromachining operation. For instance, to drill a hole the size and shape of the tool, the tool must be made to oscillate in line with the axis of the hole to be produced. To perform slotting operations, it is desirable to choose a mode where the tool oscillates in a plane determined by the tool and the slot to be cut. End milling operations seem to do best where the tool is made to oscillate in a plane perpendicular to the direction of cut. Additionally, elliptical holes can be produced by choosing an excitation frequency that causes the tip of the tool to describe the desired elliptical pattern.

4.1.3. Patterned-Surface Target Films

We have provided a series of sin(x) sin(y) foil targets on polycarbonate mounts for both the NIKE laser program at NRL and the OMEGA laser program at UR/LLE. A list of those patterned substrates that we have available is shown in Table 4–1.

We have other substrates which were produced by precision micromachining of gold, copper, silver, or aluminum blanks. The surfaces of some of these have eroded to the point where they are no longer usable. With difficulty, we can sometimes release small pieces of films cast on the eroded metal substrates but they are not useful for larger sized films, *i.e.*, pieces larger than a few millimeters in lateral extent. Additionally, we have found that micromachined molds with large patterns, for example a step-ramp pattern with P-V amplitude of 5 μm, tend to adhere to polystyrene films cast on them making it very difficult to remove the films.

TABLE 4–1
PATTERN SUBSTRATES

Substrate Number	Surface Function	P-V Amplitude (μm)	Wavelength (μm)
Gentec #01	sin(x)	0.23	12.0
Gentec #03	sin(x)	0.10	60.0
Gentec #04	sin(x)	0.25	60.0
Gentec #05	sin(x)	0.10	20.0
Gentec #06	sin(x)	0.25	20.0
Gentec #07	sin(x)	0.10	30.0
Gentec #08	sin(x)	0.25	30.0
Gentec #09	sin(x)	0.50	30.0
Gentec #10	sin(x)	0.50	20.0
Gentec #11	sin(x)	1.00	20.0
Gentec #12	sin(x) sin(y)	0.10	30.0
Gentec #13	sin(x) sin(y)	0.10	60.0
Gentec #14	sin(x)	0.47	60.0
Gentec #15	sin(x)	0.23	20.0
Gentec #16	sin(x)	0.26	30.0
Gentec #17	sin(x)	0.23	60.0
NPL01	sin(x)	0.94	30.8

4.1.4. NIKE Low-Density Foam Targets

Several versions of NIKE targets were assembled that had low-density Resorcinol-Formaldehyde (RF), polystyrene, or carbonized RF foams as integral parts of the targets.

RF foams and polystyrene foams are made at Schafer and Sandia National Laboratory (SNL) by the Schafer foam team. Foams are cast between glass slides or other appropriate materials that are separated by spacers so as to give the resulting foam the desired thickness. Dried foams are then cut to desired lateral dimensions and mounted on targets.

RF foams were carbonized by heating in flowing argon for several hours. Because the surfaces of machined foams are not smooth enough for NRL targets, we have been attempting to carbonize thin pieces of RF foam that will not need further cutting or machining. This technique has not been entirely successful because the foams tend to stick to the flat substrates on which they are carbonized. We have tried carbonizing free-standing-RF foams, but found that these thin pieces tend to curl, evidently due to uneven contraction during carbonization. Raising the temperature of the foams in the carboniza-

tion furnace very slowly helps reduce the curling, but has not eliminated it entirely. We have also tried methods of heating the foams against a substrate using a release agent such as polystyrene. Typically, the release agent interacts with the foam during carbonization and renders it useless for NRL targets. During FY00, we will continue to refine our procedure for carbonizing foam until we can routinely produce high-quality foams that are flat and have smooth surfaces.

4.2. OMEGA LASER TARGETS

OMEGA laser targets are similar in nature and specifications to some NIKE laser targets. However, a large fraction of the OMEGA laser targets are multilayer films of at least two different polymers: polystyrene (CH) and silicon-doped polystyrene (SiCH). We have found the two polymers behave quite differently when they are processed to provide target films. The regular CH (nominal molecular weight = 250,000) forms films which have good lateral strength and can be easily manipulated when they are used for target foils. The SiCH material has a much lower molecular weight. Films made from the SiCH material which we have available are very fragile and tend to crumble and require very careful handling. However, General Atomics has developed SiCH material that has a relatively high molecular weight and is monodisperse. This material casts well and is routinely made into films for the OMEGA laser. The films are subsequently cut into much smaller discs and mounted for use as OMEGA laser targets.

Many of the films used for the OMEGA targets are required to have a sinusoidal pattern imposed on one face, a layer of polymer, a smooth interface, and another layer of a different polymer. If the layer with a sinusoidal pattern on one face is very thin, there is a tendency for the pattern to also appear on the obverse face. To avoid this "bleed-through" phenomenon, we have developed an air brush technique to apply very thin layers of the polymers. During FY99, we have improved these techniques to the point where the bleed-through is nearly always negligible.

OMEGA targets that consisted of a layer of one polymer with a layer of a different polymer overlaid on the first provided some interesting and somewhat difficult problems of fabrication. The composite films were nominally 20–μm thick and were usually made up of two layers, one of normal CH and the other of SiCH. Either of the two layers could be 4 to 16-μm thick and the other layer would be thick enough to add up to 20 μm for the total thickness of the film. The interface between the layers was specified to be flat, smooth, and parallel to the two outer surfaces of the layered film. The first layer of a film was cast on an appropriate substrate, either a smooth silicon wafer, quartz plate, or the sinusoidal patterned surface of a fused quartz substrate. As discussed in a previous paragraph, if a thin layer was to be applied to a patterned surface, it was applied successively in very thin layers to avoid "bleed-through" of the pattern to the interface surface. After

the first layer was completed, it was thoroughly cured and the second layer was applied. To avoid mixing the two polymers at their interface, we often applied the second layer of the film by airbrush techniques or cast in very thin layers to build up to the final thickness without disturbing the first layer. The SiCH we were using would not form smooth layers when we tried to cast it on CH and vice versa. Research showed this to be a common problem. We altered our airbrushing technique so that the new layer did not have to "wet" the underlying layer. This resulted in much better films for UR/LLE than we were able to provide previously. When the films were complete and thoroughly cured, they were characterized, *i.e.*, surfaces and thickness measured over the entire film area. The characterization data was recorded and mapped onto a 1:1 diagram of each film.

For further information, please contact T. Walsh (Schafer Corporation).

4.3. REFERENCES FOR SECTION 4

[4–1] Project Staff, "Inertial Confinement Fusion Target Component Fabrication and Technology Development Support, Annual Report to the U.S. Department of Energy, October 1, 1997 through September 30, 1998," General Atomics Report GA–A22995 (1998), p. 4-4.

5. CRYOGENIC SCIENCE AND TECHNOLOGY DEVELOPMENT

The OMEGA laser at the University of Rochester/Laboratory for Laser Energetics (UR/LLE) and the National Ignition Facility (NIF) at Lawrence Livermore National Laboratory (LLNL) will need cryogenic targets. We devoted effort in support of the Inertial Confinement Fusion (ICF) laboratories to understand and control various solid fuel layer smoothing processes for both D_2 and deuterium-tritium (DT) fuel. We designed equipment and test pieces for laboratory work in development of cryogenic targets for NIF, and we carried out design and planning activities for the NIF Cryogenic Target System (NCTS). This chapter reports some of the interesting technical results from these efforts in FY99.

5.1. CRYOGENIC LAYERING DEVELOPMENT

Natural beta-layering, where the heat from tritium decay provides the energy to redistribute and smooth the DT ice layer, will provide a uniform and smooth DT ice layer inside a cryogenic ICF capsule. Research and development is underway at the ICF laboratories to explore techniques to enhance this process. Deposition of energy in the DT ice or DT gas by infrared (IR) or microwave illumination offers the potential to accelerate the beta-layering process, to achieve smoother DT ice surface finish, and to achieve layering in DD or HD ice that does not have the tritium decay heat source of DT.

5.1.1. IR Heating

Figure 5–1 shows the current layout for the IR heating experiments at LLNL. We have changed our IR injection method. Instead of injecting the IR beam through a view port, the beam is directly injected into the integrating sphere using an optical fiber. A small hole was drilled into the integrating sphere for inserting the fiber. Making the vacuum seal required modifying the copper adapter which attached the integrating sphere base to the cold tip. The adapter was modified and a stainless tube, aligned with the hole in the integrating sphere, was soldered to the adapter. Next, the optical fiber was slid inside a stainless tube and potted in epoxy. The fiber was inserted through the adapter's stainless tube into the integrating sphere. Finally, epoxy was applied to seal the space between the two stainless tubes.

The first experiments conducted, after installing the optical fiber and fixing some leaks, were time-constant measurements. These measurements are used to determine how well we are coupling the IR into the integrating sphere. Based on our calculations,

we are coupling into the integrating sphere with about the same efficiency as with injection through the view ports. This is not unreasonable. There are fewer interfaces in this current injection scheme, but none of the optics are antireflection (AR) coated for 3 µm IR light. On the other hand, the cryostat windows are all AR coated.

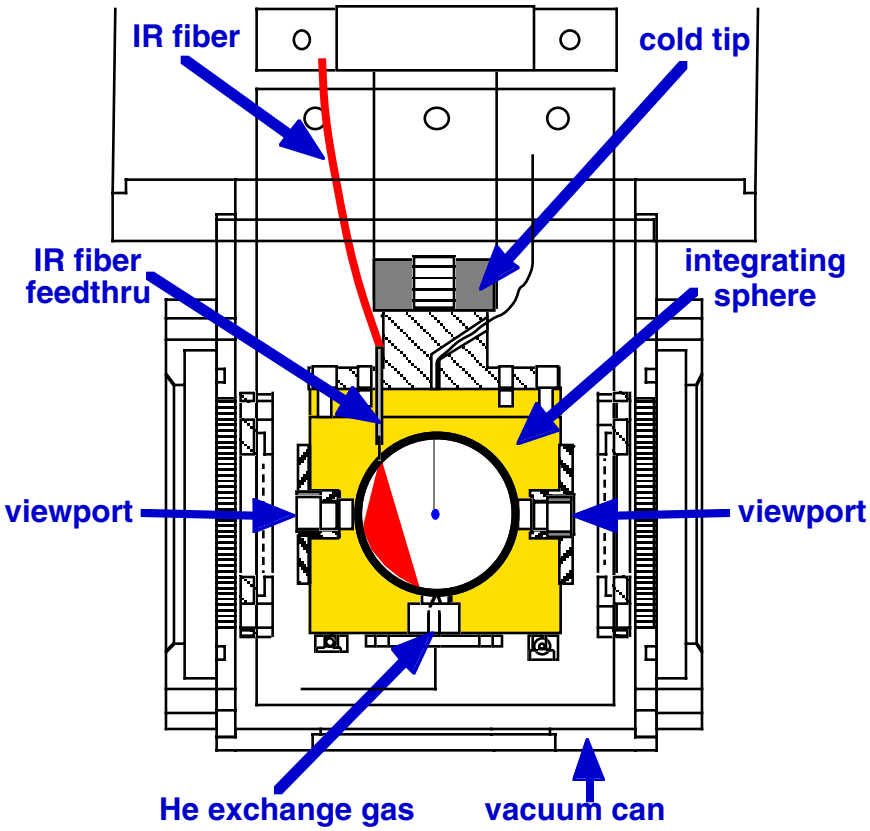

Fig. 5–1. Schematic diagram of IR optical fiber injection technique.

Apparent Versus Actual Layer Thickness. The shadowgraphy technique is used to study the ice layer uniformity inside cryogenic ICF capsules. In general, a bright band (ring) is observed in the shadowed region of a capsule image when a uniform ice layer coats the inside of a capsule. The bright band is formed by rays experiencing total internal reflection at the ice solid/vapor interface. An analytical correlation was developed to estimate the actual ice thickness formed inside a capsule from the apparent ice thickness measured on the capsule image. The apparent ice thickness is the distance from the outer edge of the capsule image to the bright band center. The results are shown in Fig. 5–2.

Based on our calculations and ray trace analysis [5–1], capsules can be separated into two categories: thin wall capsules and thick wall capsules. For a 1-mm o.d. capsule with a wall thickness greater than 75 µm, the apparent ice thickness appears thicker than the actual ice thickness. In this case, the apparent ice thickness is actually the measurement

of the wall thickness plus the ice thickness. Here, the width of the bright ring (apparent bright band) is also a function of the wall thickness and the ice thickness. For a wall thickness less than 75 μm, the width of the bright band is nearly independent of the wall thickness and the apparent ice layer thickness is less than the actual ice layer thickness. Figure 5–3 shows how bright bands are formed for these two categories.

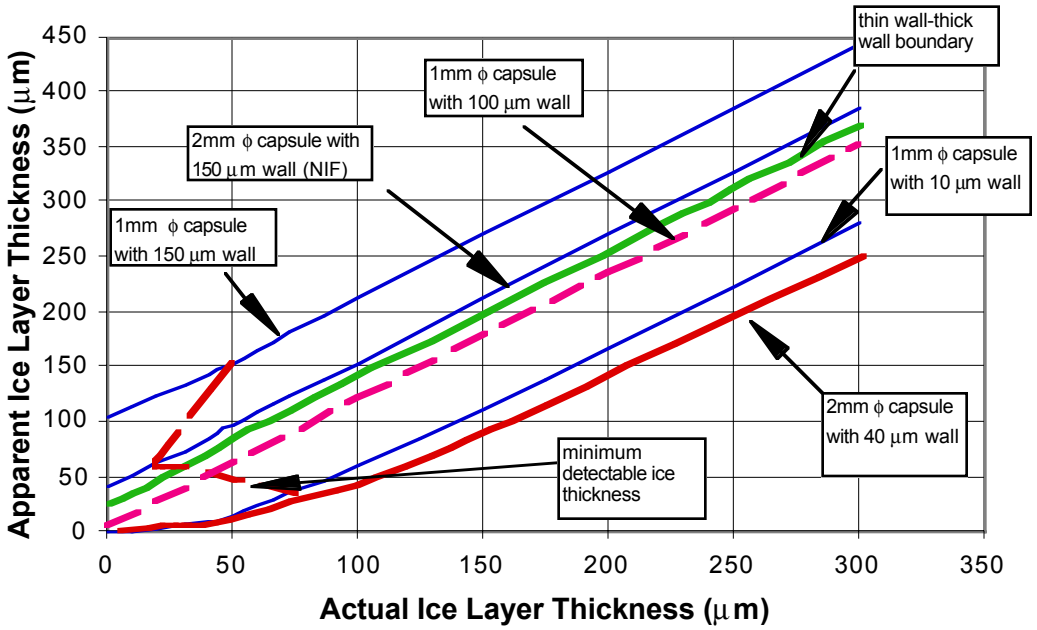

Fig. 5–2. Relationship between the actual ice thickness and the apparent ice thickness for 1 and 2-mm o.d. capsules with various wall thicknesses.

As indicated in Fig. 5–2, there is a minimum detectable ice thickness. In general, the minimum detectable ice thickness increases as the wall thickness increases for thin wall capsules. The reason is that as the wall thickness increases, the bright band is formed farther away from the capsule edge so that a clear band image can be obtained. On the other hand, the minimum detectable ice thickness decreases as the wall thickness increases for thick wall capsules. In this case, a much thicker ice layer is required to allow ray refraction to occur within the ice layer to form the bright band.

IR Illumination in a Hohlraum. Modeling has commenced for determining the illumination profile needed to generate a uniform D_2 layer inside a hohlraum. We have developed a protocol and run a base illumination case. The basic procedure is to perform a ray trace of a shell inside a hohlraum to determine the energy absorbed in the ice, capsule, and hohlraum. The data is then reduced to a format which can be inserted in to the finite element code, COSMOS, and a thermal analysis performed. The goal is to determine the illumination profile needed to produce a thermal profile commensurate with a uniform

layer. Figure 5–4 shows the hohlraum model and the relative energy absorbed in the layer.

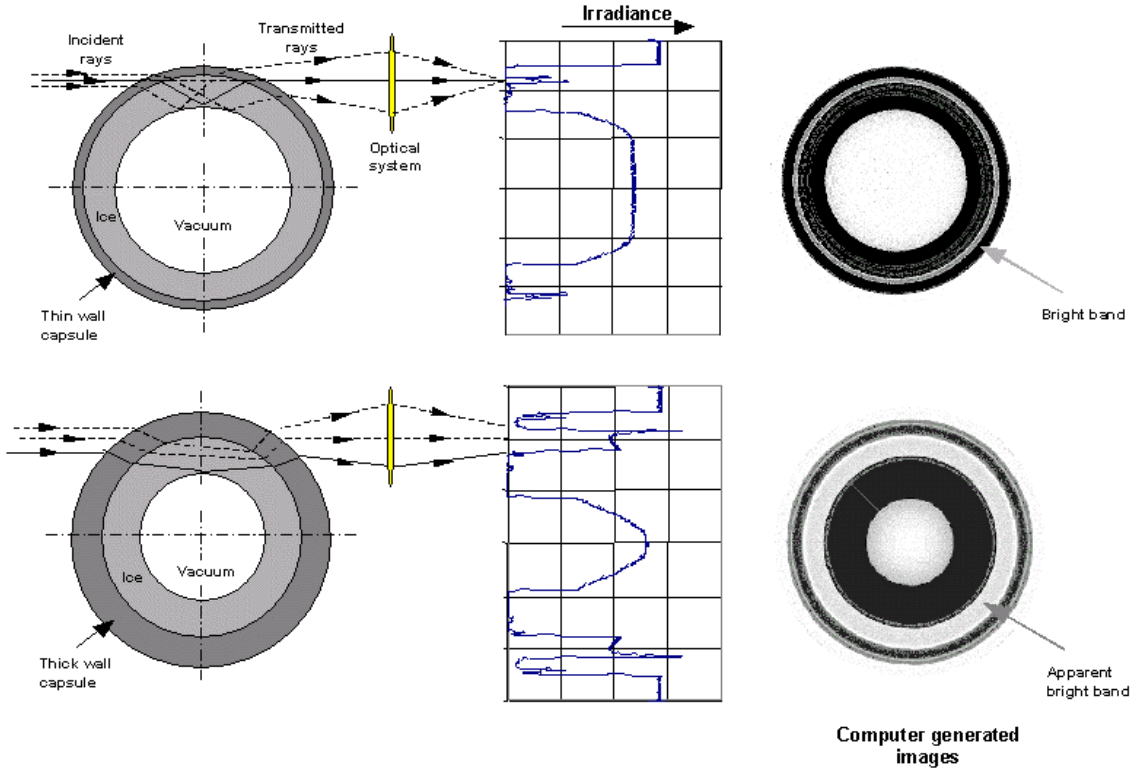

Fig. 5–3. Comparison of images from thick wall versus thin wall capsules.

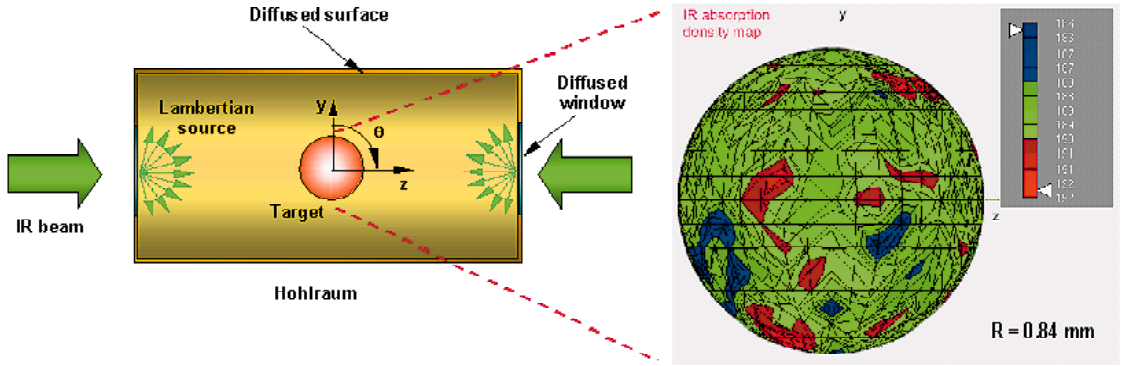

Fig. 5–4. Schematic showing IR illumination in a hohlraum and the resultant energy deposited in the D_2 ice.

With a simple diffuse source installed at both laser entrance holes (LEHs), the ice layer is found to be illuminated uniformly to within 1%. This slightly nonuniform IR deposit does not create a significant temperature gradient along the inner ice surface to form a P1 defect. Both the heat flux profiles on the hohlraum wall and on the ice layer

are also determined for the base case. From the energy balance calculation, it is estimated that the ice absorbs about 9% of the IR energy. The IR absorption coefficient of D_2 ice is 0.4 mm^{-1}. The capsule is treated as a perfect transmitted material for the IR. The hohlraum wall, assuming a diffuse white surface with 1% IR absorption, absorbs about 14% of the IR energy. The remaining 77% of IR energy escapes through the perfectly transmitting windows. To provide a 50 mW/cc volumetric heating in the ice, a 0.4 mW IR laser is needed. An average of 2.8×10^{-4} mW/mm^{-2} heat flux will be deposited along the cylindrical hohlraum wall that should not impose a considerable heat load on that surface. In this model, there was no absorption in the shell or the hohlraum windows.

5.1.2. Shadowgraphy and Spherical Capsules

Shadowgraphy, observing a capsule that is backlit, is the technique most used to study DT ice layers in ICF capsules. The capsule, however, acts as a lens, distorting the image. We have done modeling to understand this distortion.

Shadowgraphic Measurement of Surface Imperfections on an Ice Layer. We have modeled idealized surface defects on ice layers. We use spherical bumps and holes with variable height and base diameter (Fig. 5–5). A parallel light source back-illuminates the capsule. Rays are collected by a simple two-lens system to form the image. Other assumptions for the modeling are:

1. No absorption in the capsule wall or ice layer.
2. A vacuum exists inside the ice cavity.

A parametric study of the effects of defect height and base diameter on the radial position of the bright band has been carried out for a selection of capsule sizes and ice thickness. The results have been divided into two classifications for thick-walled and thin-walled shells. The distinction is the same as that discussed in Section 5.1.1. The demarcation in behavior occurs at a thickness of about 75 μm.

Defects in Thin Wall Capsules. In this study, a 1-mm diameter capsule is used with a 10-μm thick wall and an ice layer of 100 μm. In general, for a fixed height defect, the radial displacement of the bright band center position is dependent on defect base diameter (Fig. 5–6).

For bumps there are four distinct regions of relative displacement behavior. In the high mode region, there is no band shift from a defect. Shadowgraphy cannot detect high mode defects on an ice surface. With moderate modes, the height of the defect seems to be magnified compared to that of low mode defects. If the majority of the defects on the ice surface are in this mode, the RMS surface roughness will overestimate the actual value. Between the high and moderate defect modes, a transition region exists where the

position of the bright band is not easy to locate. For low mode defects, the displacement of the bright band is directly proportional to the height of the defect. There is a rapid transition between the moderate and low defect mode boundaries because of the changing surface curvature of the defects. Since the height of the defect is fixed to generate the curve in Fig. 5–6, the bump starts with a convex lens shape on the ice surface when its diameter is small. As the diameter increases, the surface gets flatter and eventually the curvature changes sign forming a concave shape on the ice surface. Figure 5–7 shows the computer results of the relative bright band center position for difference size bumps on the ice surface.

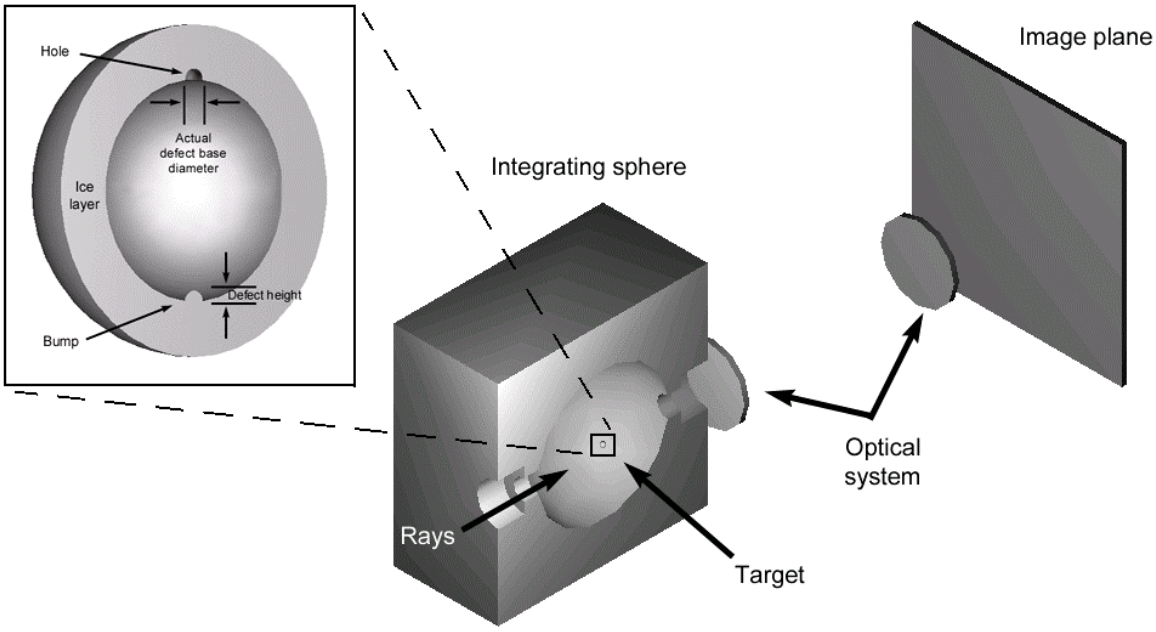

Fig. 5–5. Model of idealized ice surface defects with spherical bumps and holes.

Holes in the high mode region also cannot be detected by shadowgraphy. In the moderate and low mode regions, the displacement of the bright band is directly proportional to the height of the defect (Figs. 5–6 and 5–7).

Effects of the ice layer thickness and the wall thickness on the bright band displacement were examined. A 1-mm diameter capsule was used with defects having a fixed height (3 μm) but different base diameters on a wall ranging from 10 to 50 μm and an ice layer ranging from 75 to 200 μm.

Bump defects have a small effect ($\pm$2 μm difference) on the bright band radial displacement for the given ice thickness range and wall thickness range on well-defined defect mode regions (Fig. 5–8). A smaller effect ($\pm$1 μm difference) is observed for holes within the same range.

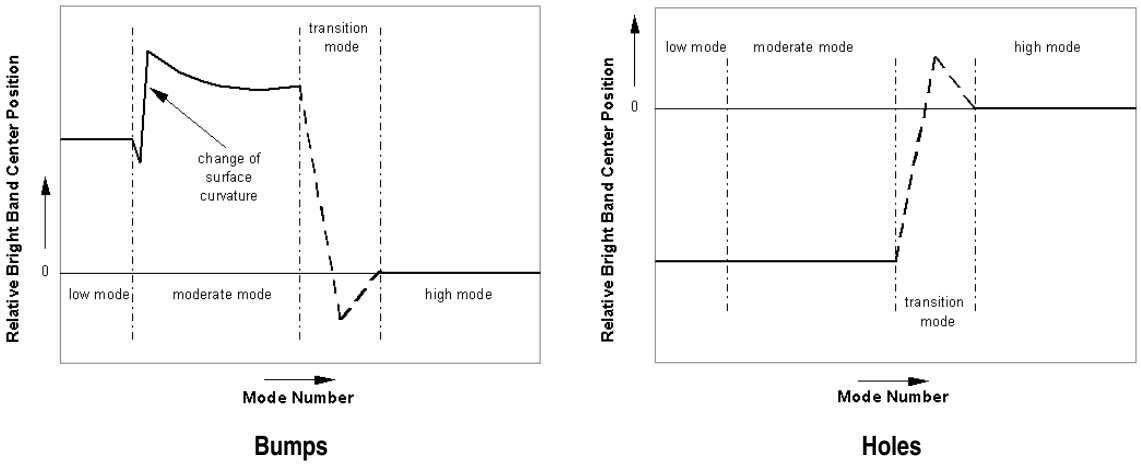

Fig. 5–6. Relative bright band center position with a fixed height defect. Base diameter decreases as mode number increases.

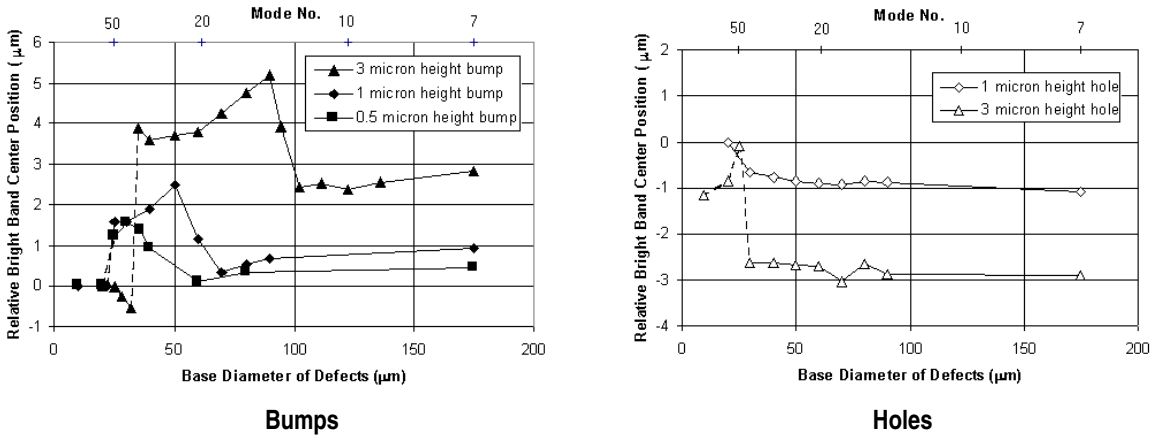

Fig. 5–7. Relative change of the bright band center position due to the presence of different sizes of defects on the ice surface.

For a 1-mm diameter capsule, the apparent defect base diameter (both bumps and holes) was modeled for different sizes of defects on an ice layer thickness (ranged from 75 to 200 μm) and a wall thickness (ranged from 10 to 50 μm). The results are plotted against the actual defect base diameter (Fig. 5–9). The slope of Fig. 5–9 is about 1.3 indicating that there is a small optical magnification of defect diameter.

Defects in Thick Wall Capsules. As shown in Fig. 5–3, the exact position of the bright band is not easy to locate for thick wall capsules. A possible alternative is to measure the inner edge position of the bright band. It is important to keep in mind that the measurement only provides a rough estimation of the actual bright band position. The uncertainty of the measurement may lead to errors in ice layer thickness on the order of several microns.

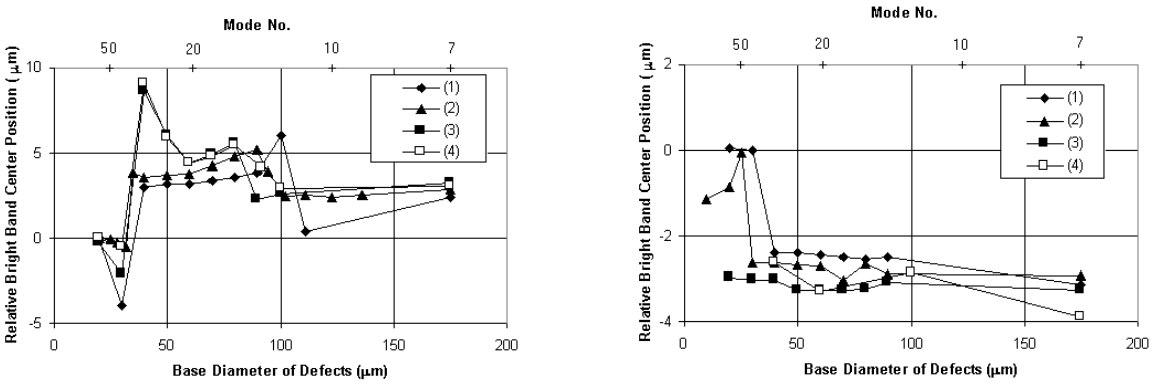

1. **75 μm ice layer for a 1-mm diameter capsule with a 10 μm wall thickness.**
2. **100 μm ice layer for a 1-mm diameter capsule with a 10 μm wall thickness.**
3. **200 μm ice layer for a 1-mm diameter capsule with a 10 μm wall thickness.**
4. **100 μm ice layer for a 1-mm diameter capsule with a 50 μm wall thickness.**

Fig. 5–8. Effects of the surface defects on various ice layer thickness and wall thickness.

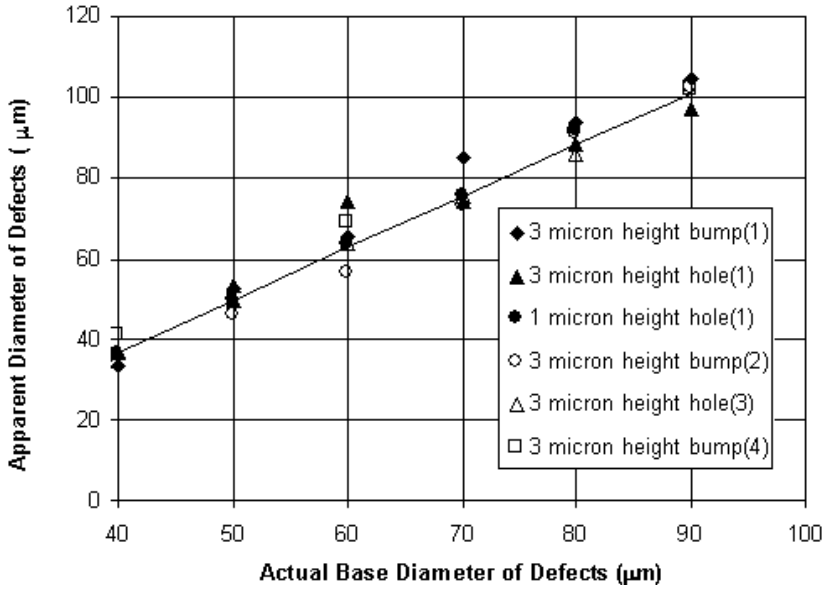

1. **100 μm ice layer for a 1-mm diameter capsule with a 10 μm wall thickness.**
2. **75 μm ice layer for a 1-mm diameter capsule with a 10 μm wall thickness.**
3. **200 μm ice layer for a 1-mm diameter capsule with a 10 μm wall thickness.**
4. **100 μm ice layer for a 1-mm diameter capsule with a 50 μm wall thickness.**

Fig. 5–9. The apparent defect base diameter is proportional to the actual base diameter.

We modeled a 1-mm diameter capsule with a 100-μm thick wall and an ice layer of 100 μm. Unlike thin wall capsules, the position of the apparent bright band inner edge as a function of defect diameter (or mode number) is relatively simple (Fig. 5–10). How-

ever, three distinct regions are still observed for bumps. In the low mode region, the slope is relatively flat and proportional to the defect height. This indicates that the shift of the inner edge of the apparent bright band is not sensitive to the defect diameter. In the high mode region, the shadowgraphy method is not able to detect the presence of defects. In the moderate mode region, a smooth transition connects the low and high mode regions. If the majority of defects on the ice surface are in this mode, the RMS surface roughness will underestimate the actual value of the defects in contrast to the magnification of the effect seen for thin wall capsules. For holes on a thick wall capsule, the shift of the apparent bright band inner edge is directly proportional to the height of the defect and is independent of the defect base diameter.

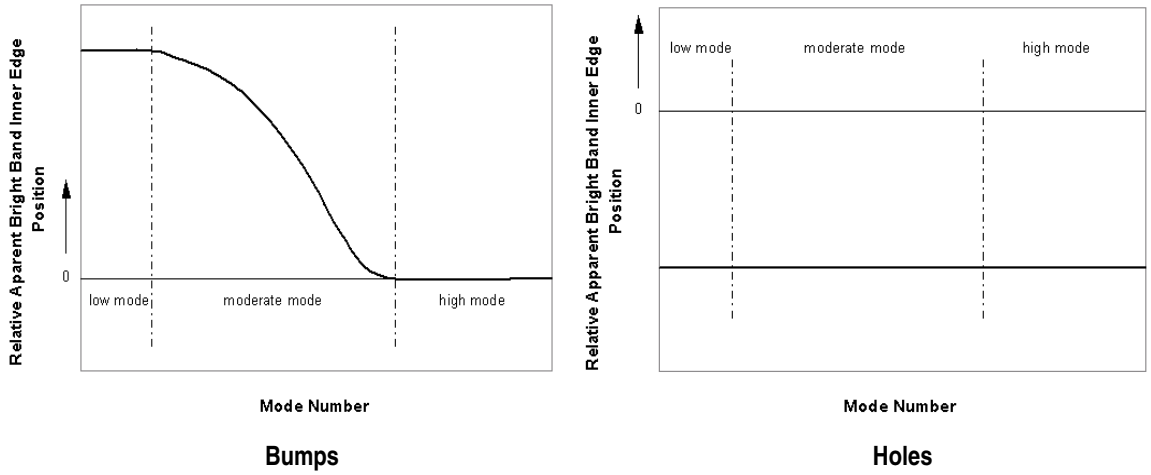

Fig. 5–10. General characteristics of the relative apparent bright band inner edge position when a fixed height defect presents on the ice surface.

Figure 5–11 shows modeling results for different size defects on a 1-mm diameter capsule with a wall thickness of 100 μm and an ice thickness of 100 μm.

Results of a parametric study on a 1-mm diameter capsule with defects having a fixed height (3 μm) but different base diameters, a wall thickness between 100 and 200 μm, and an ice layer between 50 and 150 μm are plotted (Figs. 5–12 and 5–13).

Effects of Different Illumination Schemes on Shadowgraphic Images. A parallel light source was used in the computer simulations just described in order to simplify the modeling process and reduce computational time. Current experiments at LLNL use a diffuse light source. We examined five different setups of light sources to study the effect on the bright band position and the cross section profile (Fig. 5–14). The intensity of each ray from the light source is the same regardless the direction of the ray. The shift in the bright band for each of the five cases is shown in Fig. 5–15.

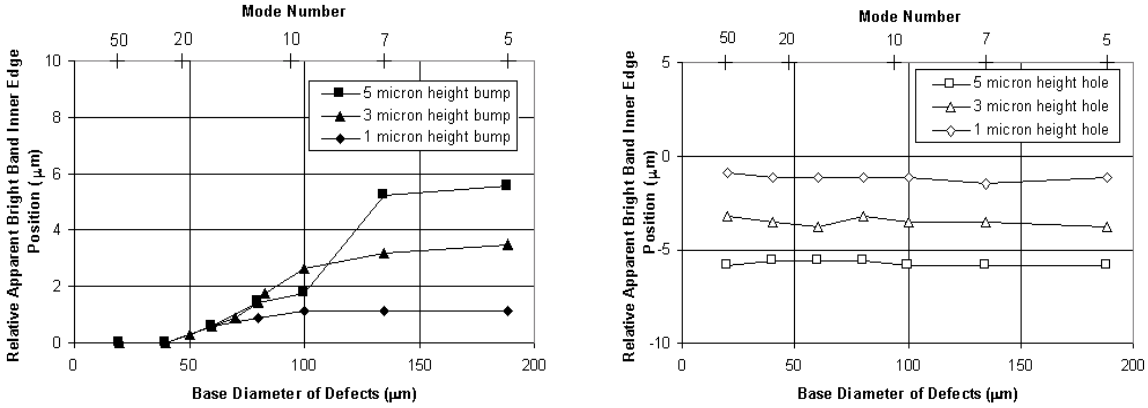

Bumps **Holes**

Fig. 5–11. Relative change of the apparent bright band inner edge position due to the presence of different sizes of defects on the ice surface.

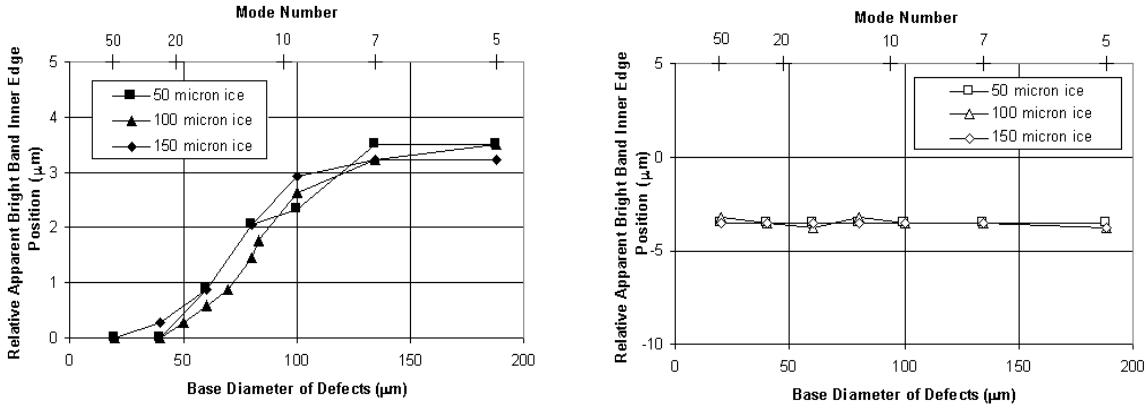

Bumps **Holes**

Fig. 5–12. Effects on the relative apparent bright band inner edge position due to defects on different ice layer thicknesses.

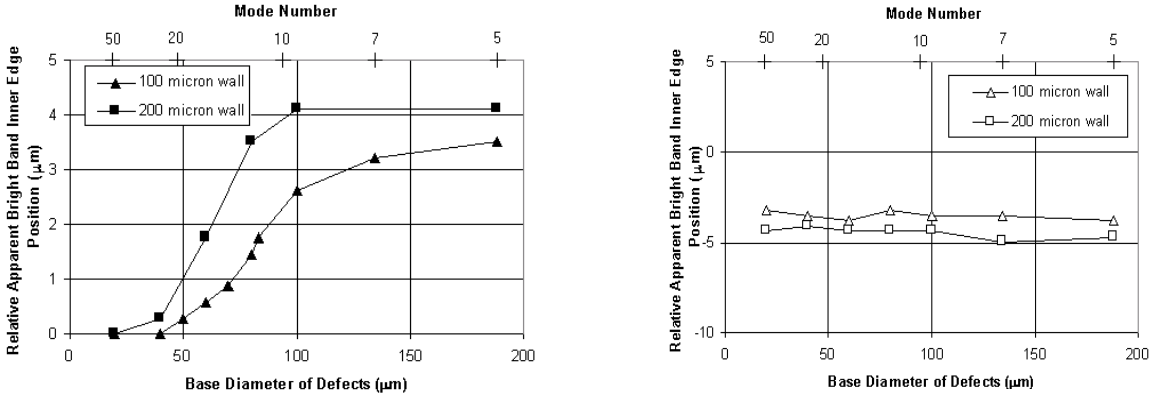

Bumps **Holes**

Fig. 5–13. Effects on the relative apparent bright band inner edge position due to defects on different capsule wall thicknesses.

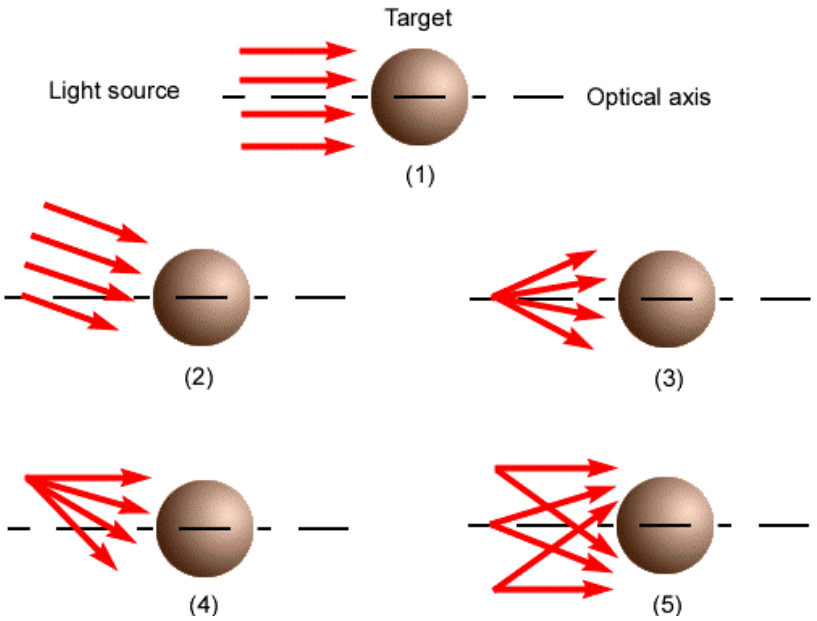

1. **A parallel light source along the optical axis (z-axis) used as the reference setup.**
2. **A parallel light source with an angle (~5 deg) with respect to the optical axis.**
3. **A single 0.05 NA light source on the optical axis (z-axis).**
4. **A single 0.05 NA light source with an angle (~3 deg) with respect to the optical axis.**
5. **Multiple 0.05 NA light sources parallel to the optical axis.**

Fig. 5–14. Different light source configurations used in the computer simulation.

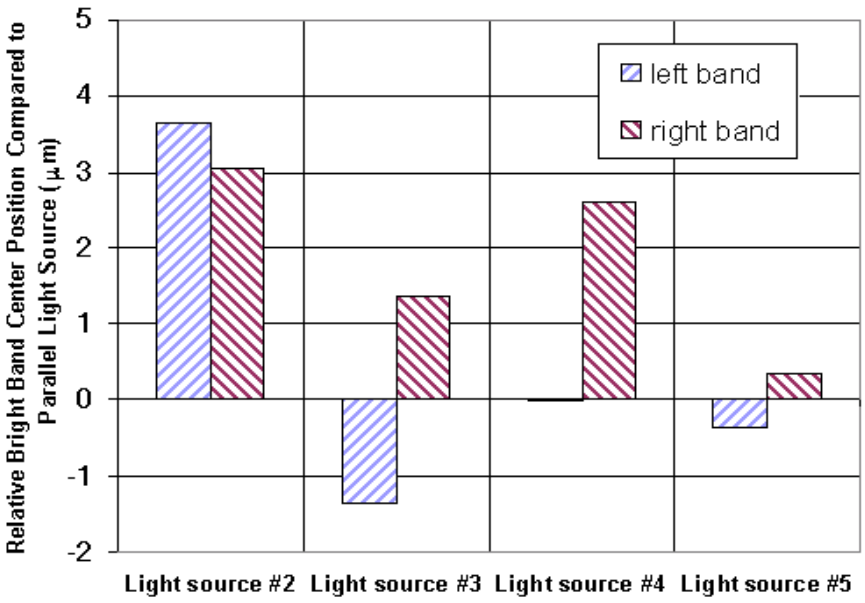

Fig. 5–15. Bright band displacement for various light source configurations.

For off axis light sources configurations (2) and (4), the bright band on one side will move towards the image center while the opposite side will move away from the image center. The measured surface roughness is affected by use of off-axis light sources. Also, the capsule image has an off-center bright spot (Fig. 5–16).

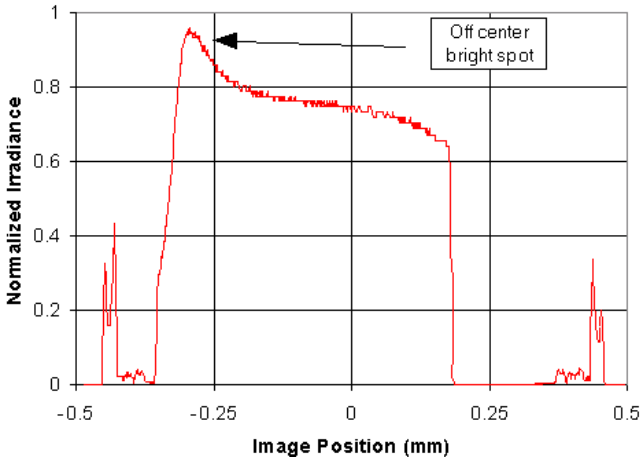

Fig. 5–16. A typical cross-sectional irradiation profile of the capsule image formed by a tilted light source.

For diffused light source configuration such as (3) or (5), the band moves evenly outward from the image center because the incident rays act as a diverging light source.

Of the cases examined, configuration (5) most closely resembles existing experimental setups. The bright band has a less well-defined edge as shown (Fig. 5–17). Also, the width of the bright band is about 1 μm wider than the band formed by the parallel light source. However, the center positions of the bright bands for both light sources are the same. As a result, modeling results using the parallel light source are valid.

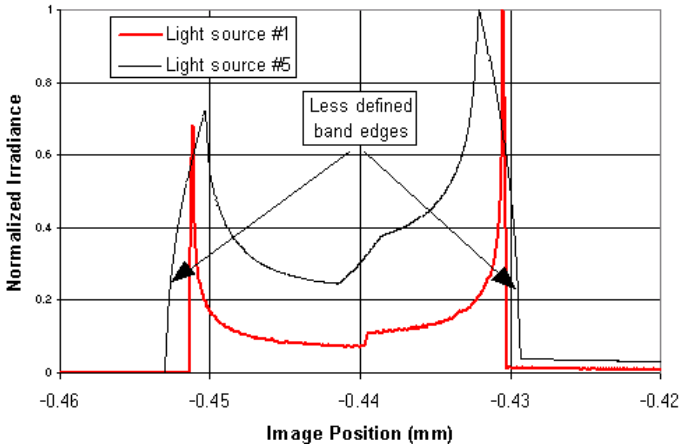

Fig. 5–17. A zoom-in view of the bright band formed by the multiple-parallel diffused lights (Configuration 5) compared to a parallel light source.

For further information, please contact Dr. J. Sater or D. Bittner (Schafer Corporation).

5.2. BETA-LAYERING SUPPORT AT LOS ALAMOS NATIONAL LABORATORY (LANL)

Beta-layering studies, to date, have been done in cylindrical experiments or in spherical capsules with fill tubes. To study cryogenic targets under fully prototypical conditions, LANL is building an apparatus to permeation fill capsules with high pressure (up to 1000 atm) DT, cool the capsules to cryogenic conditions and perform layering experiments on the capsules. This apparatus is called the cryogenic pressure loader (CPL). The design, fabrication, and testing of all components of the CPL data acquisition and control systems were completed in FY99. This system will control the target insertion and layering sphere mechanisms as well as the optical system x-y-z stage positioners. The system will also acquire DT cell image data as well as cell and cryostat temperature data.

An upgrade and testing of the motion sync system electronics was completed in FY99. The system synchronizes image acquisition to layering cell motion, using an off-the-shelf triaxial accelerometer and custom-designed signal processing electronics. Utilizing this technique minimizes the effects of cryostat motion on image quality (image defocusing and blur).

Setup and testing of the beta-layering experimental apparatus was also completed during FY99 in preparation for upcoming experiments using a newly designed beryllium torus cell. This cell has been designed to have a surface-to-volume ratio nearly identical to that of a sphere and will be used to perform DT aging experiments.

5.2.1. Design and Testing of the CPL Data Acquisition and Control Systems

The CPL system is a target-filling and β-layering apparatus designed to test permeation fill operations with DT, as well as measure tritium migration from the permeation cell apparatus to other regions within the cryostat and associated plumbing. The CPL will also permit the study of native β-layering in a permeation-filled ICF target under actual field conditions. The CPL cryogenic apparatus includes: a permeation cell, in which targets are inserted and filled; a layering sphere into which filled targets are inserted and positioned for β-layering operations; numerous temperature sensors; and an optical system that monitors the DT-filled cell and acquires image data at specified intervals once the cell is positioned in the layering sphere apparatus.

The data acquisition and control system for the CPL apparatus is designed to provide automated control of the target insertion and layering sphere apparatus, automated control of the optical apparatus used to position image acquisition optics, and automated computer acquisition of temperature and image data. Figure 5–18 is a block diagram schematic of the data acquisition and control system showing all of the components currently designed into the system. This system will be interfaced within a LabView integrated

software environment running in MicroSoft Windows NT™. (LabView is produced by National Instruments, 6504 Bridge Point Parkway, Austin, Texas. 78730-503.)

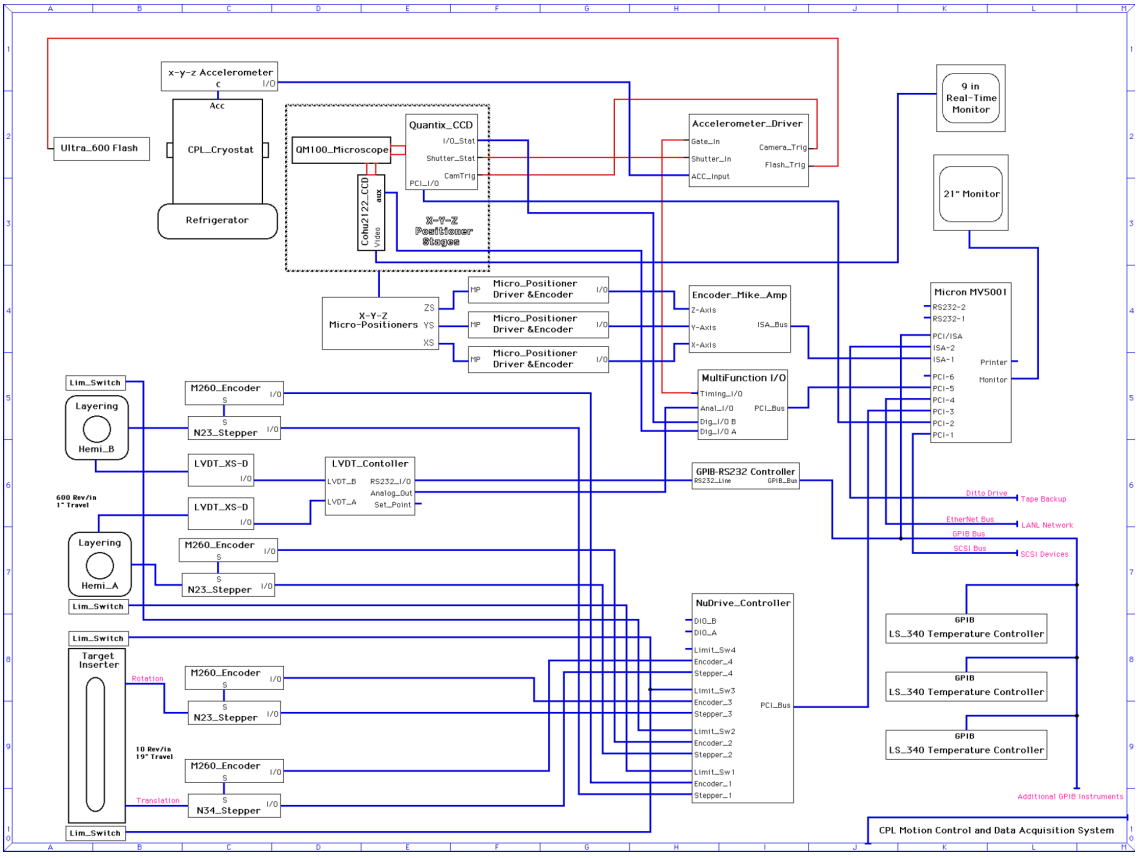

Fig. 5–18. Block diagram of the CPL data acquisition and control system. The controlled devices are the target insertion mechanism, layering sphere mechanism, cryostat temperature controllers, and the x-y-z positioning stages and flash illuminator for the target imaging system. Data is acquired from temperature sensors, position sensors and shaft encoders and cryostat motion accelerometer.

The Windows NT-based data acquisition/control computer set up and testing was completed during FY99, and all the necessary hardware and software installed and operating. The computer system is interfaced with a Photometrics Quantix CCD camera system that performs image acquisition at rates up to 3 frames/sc. The computer system will also control the automated positioning of optical components, as well as the positioning of targets within the CPL cryostat, and the control of beta-layering operations in general. The Photometrics Quantix camera system, Cohu real-time camera, imaging optics, computerized micropositioners, and Linear Variable Displacement Transducers (LVDTs) were all tested during an actual cooldown of the CPL cryostat. All are functioning well, and we are now able to acquire CPL target images, as well as monitor the target processes in real time. Figure 5–19 is an image of the 1-mm plastic sphere mounted on three

spider web fibers, which was acquired using the Quantix CCD camera and acquisition/ control computer.

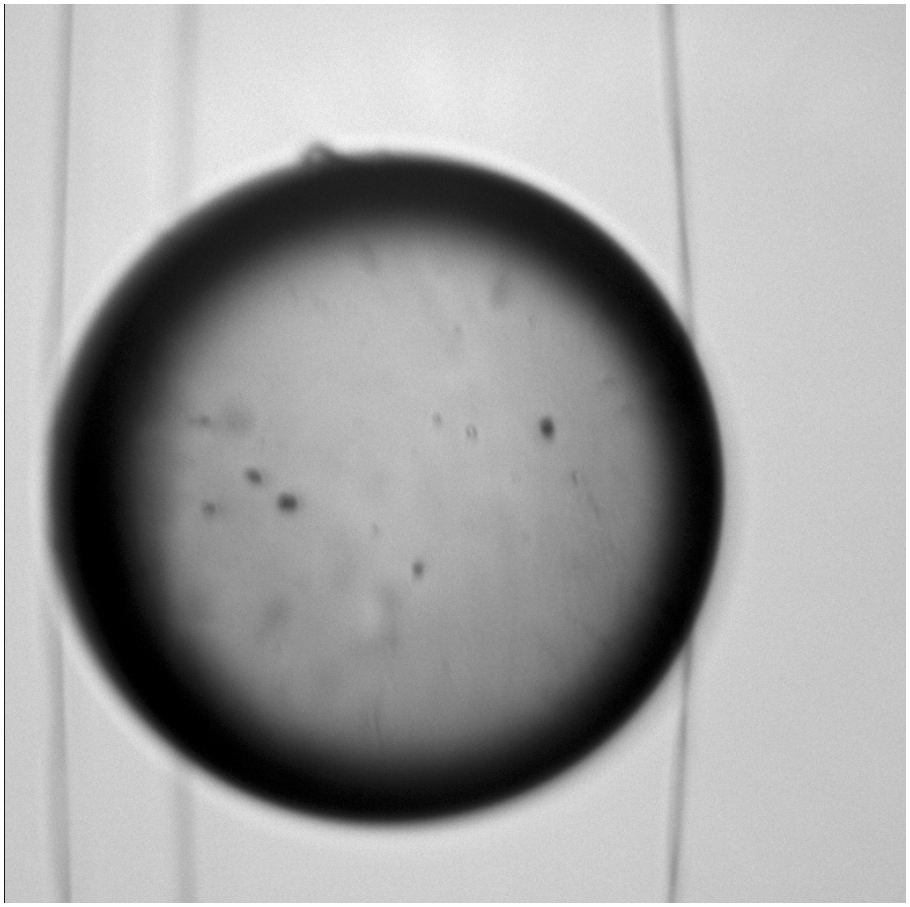

Fig. 5–19. Image of a 1-mm diameter plastic sphere, mounted on three spider fibers (visible as vertical lines in the image). This image was acquired using a Photometrics ***Quantix*** CCD camera with a flash illumination system.

The LVDTs that monitor the position of the layering hemispheres inside the cryostat were thoroughly tested at cryogenic temperatures during FY99. The LVDTs operated well at 15 K for three weeks, with high linearity over the 25-mm operating range. Using the LVDTs, we are able to determine layering hemisphere position with a resolution of about 2 μm. An LVDT is attached to each layering hemisphere to measure and indicate the translation distance of each. Figure 5–20 is a plot of LVDT readout signal (millimeter) as a function of shaft encoder positions (counts). (Graph and data courtesy of P. Ebey, LANL.) Both front and rear LVDT readouts are plotted, for both the closing and opening of the layering hemispheres. A small amount of hysteresis is present, which is probably due to drive train backlash, but the signal is very linear over the entire travel length of each layering hemisphere. In addition, the LVDT signals were not degraded by operation at cryogenic temperatures for as long as 3 weeks.

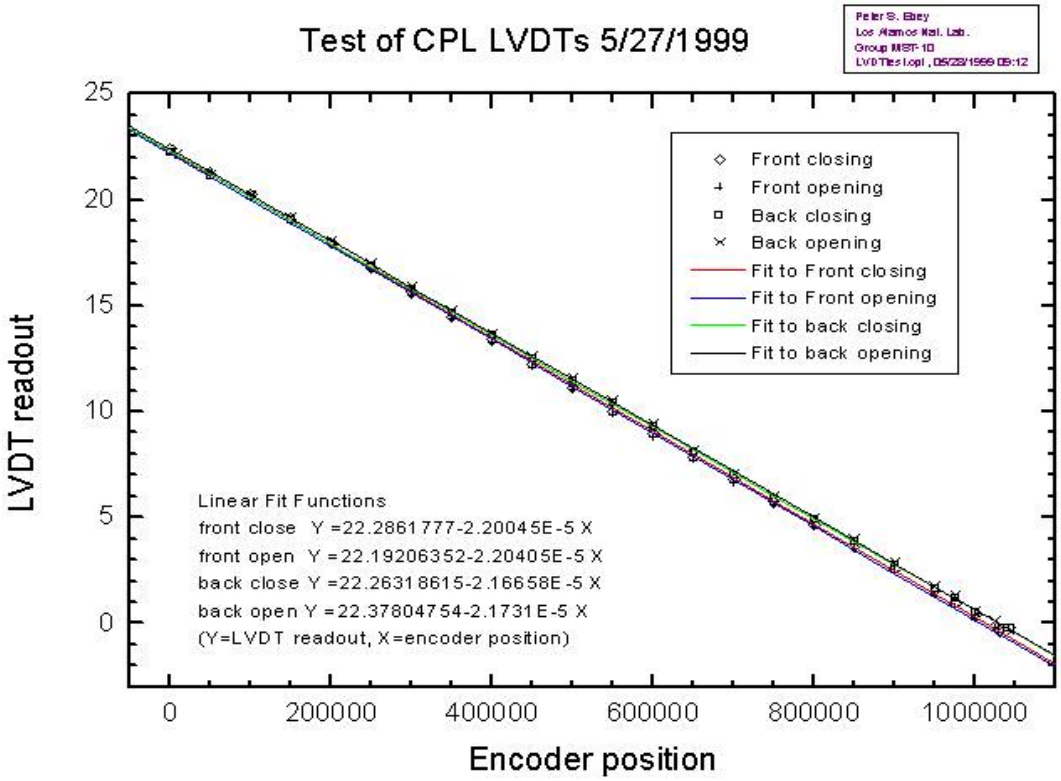

Fig. 5–20. Plot of LVDT readout signal (calibrated in millimeters) versus shaft encoder position of the layering sphere positioning stepper motors. This graph shows that the LVDT signals are a very linear function of layering sphere position (shaft encoder reading), even when operated at 15 K for 3 weeks.

The motorized x-y-z (Oriel) positioning stages have also been tested using Oriel-supplied software packages, and our Windows NT-based computer system. All three micropositioners are functioning, and give us automated submicron positioning capability for cell image position (x-y) and focus (z-position).

5.2.2. Motion Sync Electronics Upgrade and Testing

The cryostat motion sync system is used to compensate for the image motion and blur due to the mechanically induced motion of the DT layering cryostat. The system synchronizes image acquisition to layering cell motion, using an off-the-shelf triaxial accelerometer and custom-designed signal processing electronics. Motion sync electronics were upgraded with the addition of filter and phase lock loop circuitry. This upgrade extracts a "simple harmonic motion" signal from a very noisy and vibration dominated accelerometer signal. The accelerometer is mounted on the beta-layering cryostat to monitor cryostat motion and vibration. Cryostat motion causes frame-to-frame images of the cell, and layer inside, to move around the frame as well as in and out of focus. When the accelerometer signal is processed, a simple harmonic motion signal is extracted, which is then used to produce a trigger signal synchronized to a specific position in the

cryostat motion cycle. This signal then triggers the image acquisition system so that variations in frame-to-frame image position and focus are greatly reduced or eliminated.

5.2.3. Setup and Testing of DT β-Layering Apparatus

The optical system, data acquisition system, motion sync system, and image analysis systems for the beta-layering apparatus have been reconfigured and tested. This is in preparation of the upcoming series of DT aging experiments in a newly designed beryllium torus cell. All systems are functioning properly and ready for experiments to begin once we have received our fresh DT sample. This toroidal cell has a surface-to-volume ratio that is nearly identical to that of a spherical cell. These experiments will be studying the effects of DT aging on solid surface roughness and layering times.

For further information, please contact John Sheliak (GA/LANL).

5.3. CRYOGENIC TARGET SYSTEM DEVELOPMENT FOR NIF

The deuterium test system (D_2TS) will fill prototypical NIF target assemblies with D_2 or HD fuel, cool the target to cryogenic temperatures, and then permit layering studies to be conducted in the actual NIF target geometry. The target assembly capsule is filled via permeation in a high-pressure cell, thereby eliminating the fill tube which was a major source of thermal asymmetry in previous experiments. The D_2TS design provides optical access to the capsule for IR layering experiments and includes electrical connections to the hohlraum to allow temperature shimming. The high-density fill capability will produce thick fuel layers which are accessible for characterization in the cylindrical geometry of the hohlraum. The system also functions as a partial prototype for the NIF Cryogenic Target System (NCTS). It allows key concepts of the NCTS to be tested including permeation filling of capsules inside of hohlraums with sealed laser entrance hole (LEH) windows, investigation of the effects of the cryostat cooling method on the vibration of the target, target transfer from the filling system to the insertion system, and cold transport of filled targets over extended distances.

The D_2TS is designed to fill, transport, and layer one target assembly at a time. These typically consist of a hohlraum attached to a robust cylindrical base by two sapphire rods. A fine capillary tube for hohlraum gas control extends from the hohlraum to the base. A thermal shroud, with windows aligned with the hohlraum windows, can be installed over the target and be mechanically and thermally attached to the target base. The D_2TS consists of eight main subsystems as shown in Fig. 5–21. They are: the main cryostat, the cryogenic target gripper, the permeation cell, the permeation cell housing

and motion system (PCHMS), the permeation cell cooling and support system (PCSCS), the permeation cell plug remover (PCPR), the cryostat sliding mount, and the gate valves.

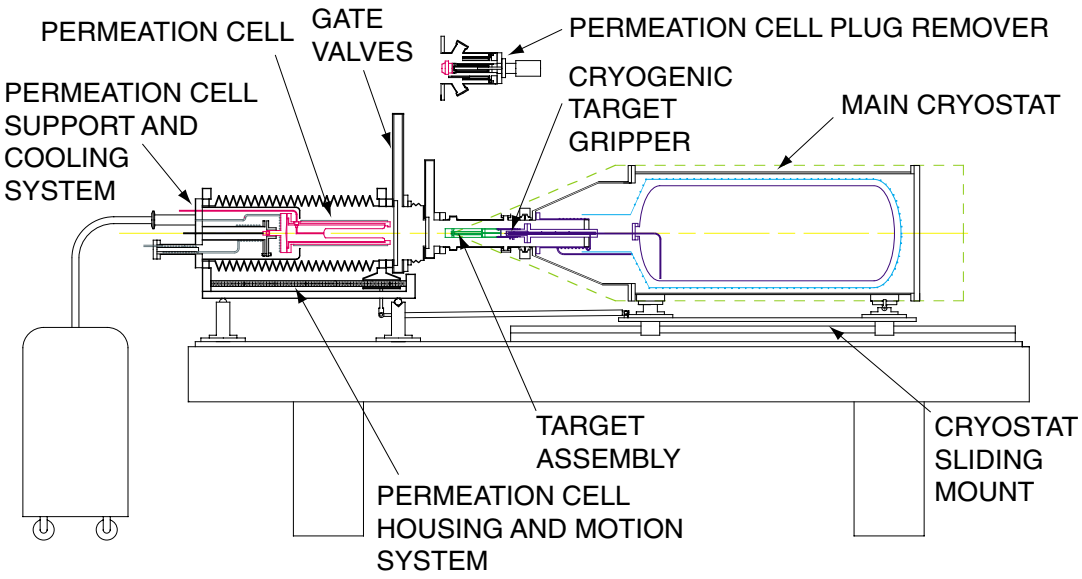

Fig. 5–21. The main cryostat of the D_2TS retrieves a target assembly from the permeation cell, once the target has been filled and cooled.

The following operations would be performed to permeation fill a target in the permeation cell and retrieve the target with the main cryostat in preparation for further investigations with the filled target.

1. With the main cryostat slid back on its slide, the gate valve (Gate Valve A) to the PCHMS is opened, and the target assembly is placed into the cell.
2. Gate Valve A is closed.
3. The PCPR is bolted onto Gate Valve A.
4. The PCPR and PCHMS are evacuated.
5. Gate Valve A is opened.
6. The PCHMS moves the permeation cell plug (held by the PCPR) into the cell breech-lock.
7. The PCPR rotary stage rotates the plug inside of the permeation cell breech-lock to the closed position (the +60-deg position).
8. The cell diaphragm is pressurized, sealing the cell plug closed.
9. The PCPR stays attached to the cell during D_2 filling of the cell, the cooling of the cell, the removal of the excess D_2 from the cell, and addition of a low pressure of helium exchange gas into the cell and, hence, into the target's hohlraum.

10. The cell diaphragm is evacuated.
11. The PCPR rotary stage rotates the cell plug to the open position (the 0-deg position).
12. The PCHMS moves the plug (still held by the PCPR) away from the cell.
13. Gate Valve A is closed. The PCPR is unbolted from Gate Valve A and removed.
14. The main cryostat is slid towards the PCHMS and connected to the PCHMS's traveling flange carriage by a jointed shaft. At this time, the main cryostat's gate valve (Gate Valve B) is attached to Gate Valve A.
15. The space between the Gate Valves A and B is evacuated and the valves are opened.
16. The PCHMS moves its travelling flange back, pulling the main cryostat with it, until the vacuum shroud of the main cryostat envelopes the end of the permeation cell and the cryogenic target gripper has contacted the target assembly base.
17. After the cryogenic target gripper has engaged the target assembly, the PCHMS moves its travelling flange forward pushing away the main cryostat from the cell. This continues until the Gate Valve A is forward of the permeation cell.
18. Gate Valves A and B are closed and then disconnected from each other.
19. The shaft coupling the main cryostat to the PCHMS is disconnected. The main cryostat is slid back on its slide to the appropriate location for layering experiments or removal from its carriage. For layering experiments, the carriage is also locked to the rails once in position.

A key feature which allows this concept to work is that the capillary tube is very long compared to its inside diameter. It will take a long time for the helium exchange gas in the hohlraum to leak out of the hohlraum to such a level that a DT-filled capsule would lose thermal contact with the hohlraum (at which point it could heat up and burst). For a typical capillary geometry, 15-cm long and 51-μm inside diameter, it was calculated that the time required for helium or deuterium to go from molecular flow in the capillary to molecular flow in the hohlraum was 2.3 h. The capsule will still be in thermal contact (have a temperature less than 10 K above the hohlraum) at this lower pressure. Additionally, the mass flow exiting the capillary upon initiation of molecular flow in the capillary was calculated to be so small that even a modest pump («1 ℓ/s) could maintain the vacuum surrounding the target assembly and permeation cell. Thus, the 2.3 h represents the minimum time allowable to transfer the target assembly from the cell to the main cryostat once the cell has been opened. During actual operation, this step should take approximately 0.5 h, leaving a comfortable safety margin.

Another key feature of this concept is that when the cryogenic target gripper engages the target assembly, it must make good mechanical, electrical, and thermal connections. It must also seal the gas line that allows helium gas to be added to the hohlraum for thermal connection of the capsule and for studying the effects of tamping gas addition to the target. The concept for the gripper is shown in Fig. 5–22 and the gripper's current stage of assembly shown in the photograph in Fig. 5–23. The gas seal between the gripper and the target base will be provided using either an indium O-ring or foil. The force needed to make the seal and the thermal contact required is expected to be 450 to 670 N (100 to 150 lb). The two electrical connectors provide for a total of 32 wires to be connected to the target assembly. Twenty four wires are allocated for heaters and temperature sensors on the hohlraum. The remaining wires may be used to heat the capillary tube in the event that hydrogen is used in the tamping gas mixture, thereby preventing the hydrogen from freezing and plugging the capillary.

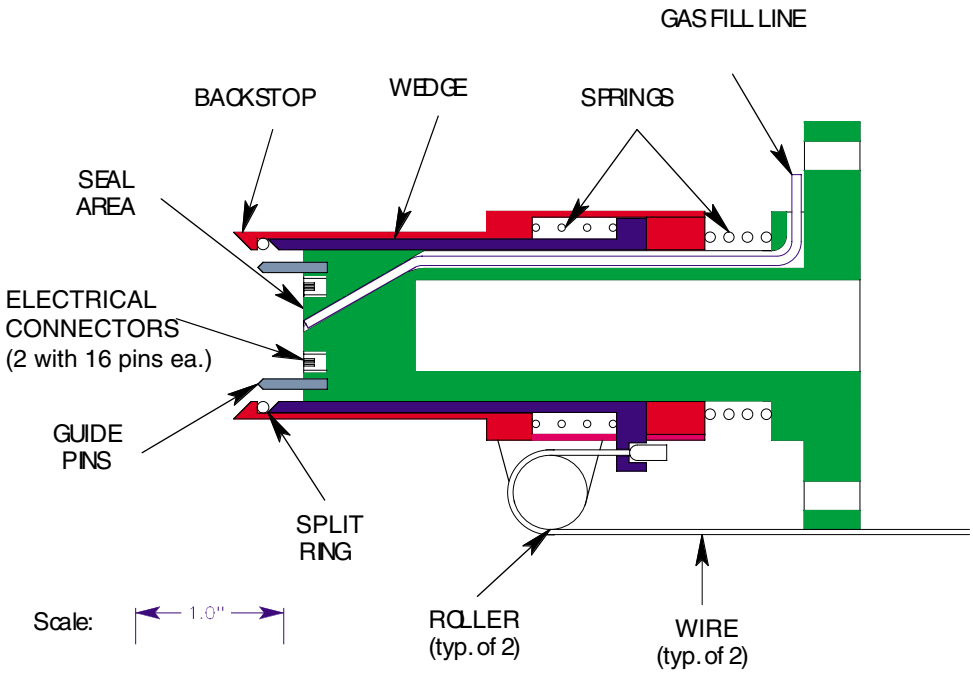

Fig. 5–22. In the concept for the cryogenic target gripper, pulling on the wire causes the split ring to be forced inwards by motion of the wedge towards the backstop. This reduces the split ring's inner diameter so that it enters a groove on the target assembly's base (not shown). Further pulling on the wire seats the target assembly base against the seal area.

The operation of the gripper is as follows. The gripper is inserted over the target assembly base so that the split ring is aligned with the groove on the base. At this point, guide pins on the gripper have engaged matching holes on the base, providing sufficient alignment to allow the electrical connectors to engage (the connectors contain two sets of

alignment pins as well). Next, the gripper actuating wire is pulled, causing the wedge to move towards the backstop and forcing the split-ring to move inward into the groove on the base. Pulling on the wire further bottoms out the wedge on the backstop, so that both the split ring and the target assembly base are pulled in the direction of the main cryostat. This continues until the target assembly base is bottomed out against the seal area. A test apparatus has been designed so that the thermal, electrical, and gas-sealing performance of the gripper can be tested early in FY00.

Fig. 5–23. The parts of the cryogenic target gripper have been machined. The gripper is shown partially assembled.

The D_2TS permeation cell is based upon the permeation cell developed for the OMEGA Cryogenic Target System. The D_2TS permeation cell has a maximum allowable working pressure of 117 MPa (16,900 psi). It was designed to the intent of the ASME Boiler and Pressure Vessel code and will be proof tested at 125% over the maximum allowable working pressure. A draft stress report has been prepared and distributed for comments.

The concept described above is known as Concept IA. It is a modification of the first concept, known as Concept I, developed in early FY99. Concept IA was developed to overcome limitations of Concept I which will arise when the system is upgraded to a NCTS. In Concept IA, the target assembly is a separate entity from the cryostat. In

contrast, the Concept I target assembly is always attached to the main cryostat even during filling in the permeation cell. Thus, a portion of the target assembly base must function as part of the pressure boundary, known as the cell plug, during target filling. Since the Concept I cell plug is attached to the main cryostat, it would be activated by an ignition shot. The only material found with a suitably low neutron activation was beryllium. (LLNL personnel performed the neutron activation analysis according to the procedure outlined in Ref. 5–3 using the concept geometry and material compositions supplied by General Atomics.) However the strength of beryllium is insufficient for the stress applied during target filling. Materials with sufficient strength were susceptible to activation and had too low a thermal conductivity to allow the target to be cooled, especially with IR layering techniques applied to the target. No material was found for the Concept I cell plug that could handle all of the constraints for NIF. Concept IA solves these problems by directly connecting the target assembly to the main cryostat without an intervening cell plug. Thus, mechanical strength, thermal conductivity and neutron activation are not issues for the Concept IA cell plug. Concept IA additionally removes the need for high-pressure electrical feedthroughs, used for heaters and temperature sensors on the target, in the cell plug.

Concept IA, however, does present several technical complications. The target assembly must now be remotely retrieved from the permeation cell after filling and cooling. In addition, thermal, electrical and gas connections must all be remotely made, at cryogenic temperatures, between the main cryostat and the target assembly base. This key issue will be addressed in the gripper tests. Since Concept IA is more prototypical of the NCTS, it has been selected as the baseline D_2TS concept.

For further information, please contact Dr. N. Alexander (GA).

5.4. REFERENCES FOR SECTION 5

[5–1] Project Staff, "Inertial Confinement Fusion Target Component Fabrication and Technology Development Support, Annual Report to the U.S. Department of Energy, October 1, 1996 through September 30, 1997," General Atomics Report GA–A22816 (1998) p. 5-11.

[5–2] Ray tracing was performed using the TracePro™ commercial optical modeling program. For further information, contact Lambda Research Corp., Littleton, Massachusetts 01460.

[5–3] J.F. Latkowski, J.J. Sanchez, and L.C. Pittenger, Fusion Technology Vol. **35**, 255 (1999).

6. OMEGA TARGET SYSTEM ENGINEERING

During the past year, the team of the University of Rochester/Laboratory for Laser Energetics (UR/LLE), Los Alamos National Laboratory (LANL), and General Atomics (GA)/Schafer made great progress toward completion of the OMEGA Cryogenic Target System (OCTS). All equipment was delivered to UR/LLE. Installation and system integration work is in progress at UR/LLE. The following major achievements took place during FY99: (a) procurement of all remaining components was completed; (b) the fill/transfer station (FTS) cryostat was shipped to UR/LLE during 11/98; (c) GA personnel supported the first FTS cryostat cooldown at UR/LLE and performed thermal analyses in support of the FTS cryogenic testing; (d) the gloveboxes for the FTS and for the deuterium-tritium (DT) high pressure system were shipped to UR/LLE during 1/99 (LANL); (e) the DT high pressure compressor was shipped to UR/LLE during 2/99; (f) the lower pylon (LP), surrogate tank (ST), chain locker (CL), and moving cryostat transport cart (MCTC) No. 2 were installed at GA's Bldg. 35 test facility and successfully used with the upper pylon (UP) in target placement and moving cryostat (MC) shroud removal tests (equipment returned to UR/LLE during 5/99); and (g) MC and MCTC No. 1 assembly work and cryogenic testing were completed successfully (shipped to UR/LLE during 6/99).

GA's remaining task consists of providing services as requested by UR/LLE to support the system installation and integration effort. These services will include consulting support and preparation of project closeout documentation.

Scheduling problems resulting from late delivery and rework of some MC shroud components forced technical compromises to maintain the overall schedule of shooting cryotargets in early FY00. The primary compromise made was to reduce the degree to which integrated system testing was performed at GA with the MC/MCTC and the shroud pulling system. The testing work was replanned to totally separate the MC cryogenic testing schedule from the shroud pulling system test schedule. This made it possible for the UP, LP, CL, and MCTC No. 2 to be shipped to UR/LLE during mid-May so that some components could be installed during a scheduled maintenance shutdown there. The MC assembly work was performed in parallel with the shroud pulling tests. The MC cryogenic tests concluded during early June, several weeks after the shroud puller system was shipped to UR/LLE. Therefore, no shroud pulling tests were performed with the shrouds at cryogenic temperatures at GA. Shipping a series of complex subsystems to the customer without performing fully integrated system tests is very undesirable and required UR/LLE to perform much of the necessary system integration work. However,

to the extent that subsystem testing and system integration work was performed at GA, it was very successful.

6.1. FILL/TRANSFER STATION

After component testing at GA, the FTS internal equipment and cooling module were packed and shipped to UR/LLE in September 1998. Due to delays in locating and repairing leaks in the helium circulation tubing at the vendor, the FTS cryostat was shipped directly from the vendor to the UR/LLE in November 1998.

GA personnel supported the final assembly and initial cryogenic test of the FTS system at UR/LLE during late February and early March. In many aspects, the test results were successful. The vacuum spaces all reached the required 10^{-6} to 10^{-7} torr range. All eight cryocoolers reached their specified value of approximately 9 K with no load. The steady-state temperatures reached were 10 K for the internal equipment and 16 K for the dome, both as predicted by thermal analysis. The steady-state temperatures of the cryostat were the same for operation under vacuum or 50 mtorr helium gas, showing that convective heat transfer is small, as predicted.

The average steady-state temperature of the cryostat base, however, was 32 K, which is much higher than the predicted 16 K and the required 26 K. Over the next few months, GA personnel supported UR/LLE in an attempt to explain why the base temperature was out of specification and to find ways to lower it. UR/LLE implemented several modifications including adding radiation baffles to the penetrations, changing the instrumentation wiring to low conductivity wire, and reversing the base helium circulation flow direction. A second cryogenic test in May resulted in an average base temperature of 26 K.

The second cryogenic test of the FTS cryostat included additional instrumentation designed to locate the root of the problem. Using thermal models developed during the design phase, GA personnel looked at many possible scenarios. The only scenario in which the test results matched the analytical results is when the base liquid nitrogen tank is not connected to the liquid nitrogen intercept ring. Due to the all-welded design of the cryostat, this area is nearly inaccessible and cannot be easily inspected or repaired.

Further modifications to the cryostat base were made by UR/LLE prior to the third cryogenic test. These included adding material to thermally short the cryostat dome intercept ring to the base intercept ring. Another change was to divert some of the helium circulating gas from the internal equipment loop and use it to help cool the base. In the third cryogenic test, the base reached an average temperature of 24 K, which is cold enough to allow the filling and transfer of thin-wall (1 μm) capsules. During this third

test, OMEGA cryogenic targets were successfully filled to 100 MPa (1000 atm), cooled to cryogenic temperatures, and transferred cold to the MC docking port.

For further information, please contact C. Gibson (GA).

6.2. CRYOGENIC TARGET POSITIONING SYSTEM (CTPS)

The CTPS comprises about half of the OCTS. It receives a filled cryogenic target from the FTS (Section 6.1), transports it to the target chamber center, and precisely positions it in preparation for the laser shot. As part of this operation, the CTPS maintains the target at temperature and provides the environment required for target layering. A cryogenic cooling shroud is removed at high speed to expose the target milliseconds before the laser shot. This system consists of five subsystems: the MC, MCTC, LP, CL, and UP. UR/LLE was responsible for the design, fabrication, and assembly of the LP and CL.

Procurement, assembly, and subsystem tests were completed successfully during the year. Limited system integration work was also completed successfully. Scheduling and budget constraints prevented performance of a fully integrated test of the entire CTPS at GA. The details of this work are described in the following sections.

6.2.1. Moving Cryostat

The MC consists of cooling shrouds (upper and lower), a cryocooler, fine positioner, and frame. One complete MC (No. 1) was assembled for use in cryogenic tests. A second set of MC cooling shrouds (MC No. 2) was assembled. MC No. 2 was used only for mechanical tests with the shroud puller system (Section 6.2.3).

Figure 6–1 shows MC No. 1's cooling shrouds and the cryocooler cold head connections before multilayer insulation was installed. Figure 6–2 shows the upper cooling shroud with the outer and intermediate caps removed to expose the layering sphere cap. Inside this cap is a spherical cavity that provides an isothermal environment for the target during transport from the FTS to the OMEGA target chamber center. The mounted target protrudes into the layering sphere cavity from below through a small hole in the bottom of the sphere. The target mount is on the end of a 0.75-m (29-in.) long stalk that can be moved by the four-axis fine positioner.

Assembly of MC No. 1 was completed during May 1999. It was installed in the MCTC, and cryogenic testing began immediately. A full battery of cryogenic tests was completed during early June and all were successful. The results obtained showed that the MC easily satisfies all temperature operating requirements, both for baseline and

augmented beta-layering conditions. Parametric tests were performed to assess the MC's performance under various operating conditions.

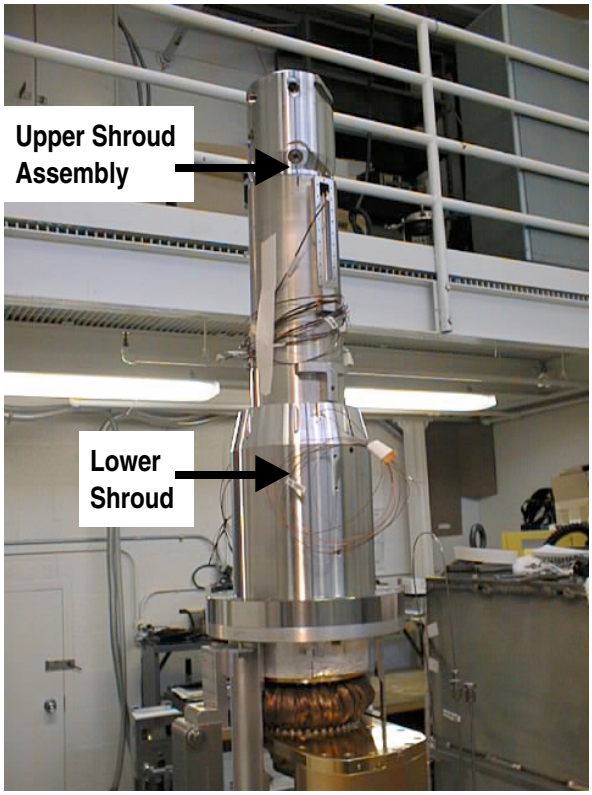

Fig. 6–1. MC thermal shroud assembly.

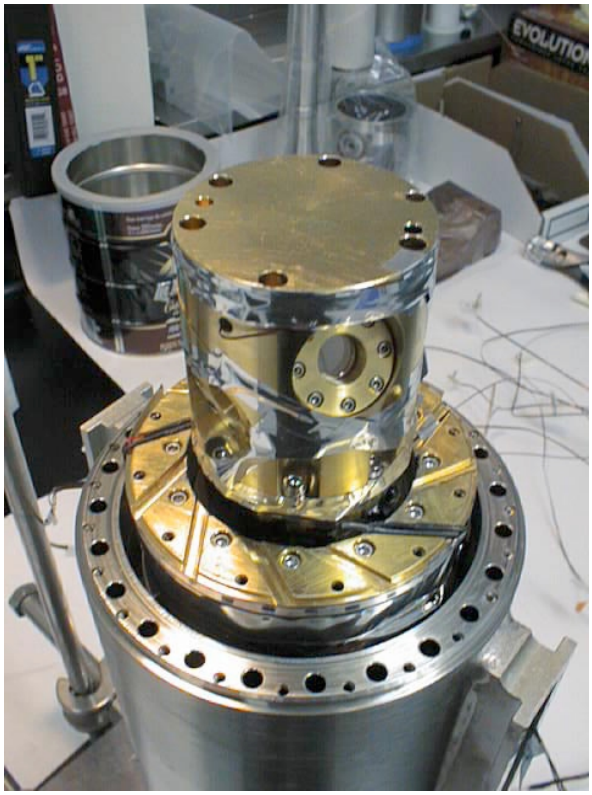

Fig. 6–2. Layering sphere.

Figure 6–3 shows the results of the cooldown from ambient test. It took about 4 h and 20 min for the layering sphere to reach 63 K, and then the temperature plunged to ~12.7 K during the next 30 min. The ultimate layering sphere temperature attained was 11.8 K. Under the design basis operating condition (50 mtorr helium at the layering sphere, 10^{-5} torr in the MCTC vacuum chamber), the layering sphere temperature was 13.7 K.

Figures 6–4 and 6–5 show the results of two of the parametric tests. Figure 6–4 shows the variation of the layering sphere temperature as a function of heat input to the layering sphere. The layering sphere temperature was 18 K when 3 W of external heat load was applied directly to the layering sphere. This demonstrated that the system has plenty of capacity to handle the ~0.3-W heat load that will be imposed by infrared layering. Figure 6–5 shows the variation of layering sphere temperature as a function of helium gas pressure inside the MC shrouds. This demonstrated that the gas pressure can vary significantly from the 50 mtorr nominal design basis without causing the layering sphere to exceed 18 K. A test was also performed to check the temperature stability of

the layering sphere. The layering sphere was stable within ±5 mK during this test. The design requirement was ±50 mK.

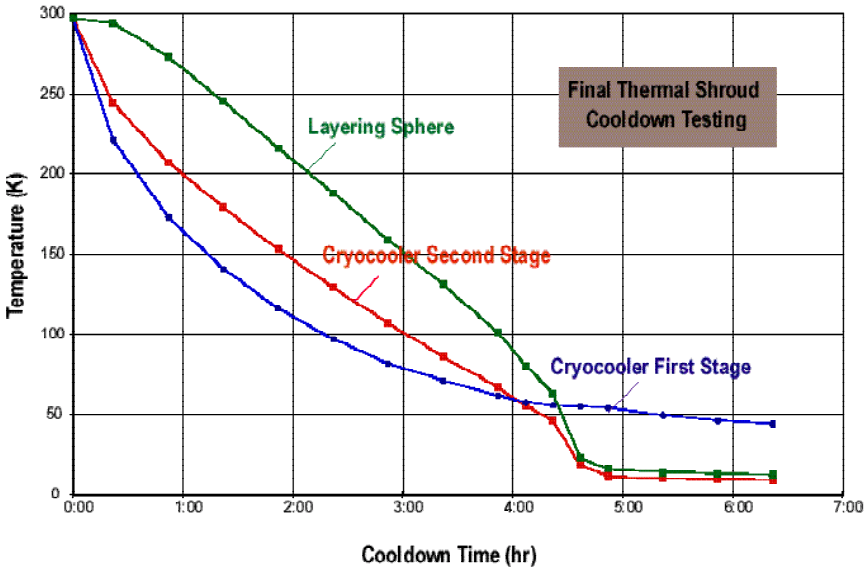

Fig. 6–3. MC cooldown test.

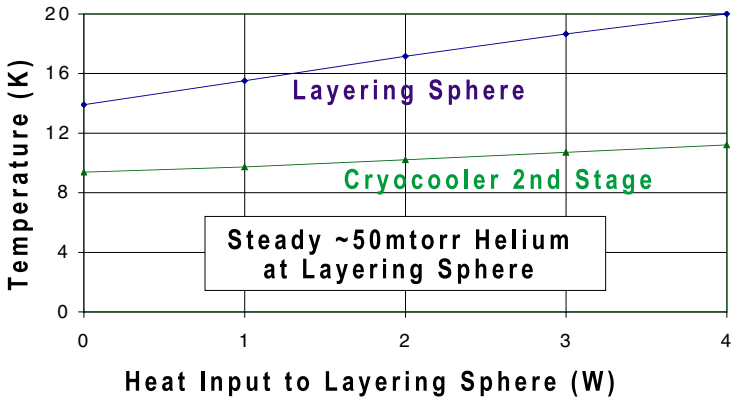

Fig. 6–4. Layering sphere heating versus temperature test results.

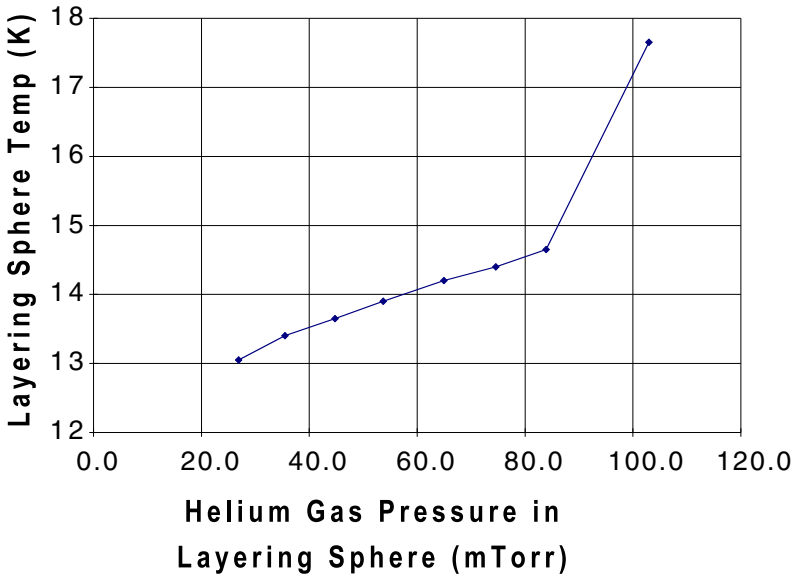

Fig. 6–5. Layering sphere exchange gas pressure versus temperature test results.

6.2.2. Moving Cryostat Transport Cart

The MCTC contains all support equipment required for the MC to function properly. Its major subassemblies include a vacuum chamber (which encloses the MC), piping manifolds, and a spooler which deploys and recoils electrical and pneumatic lines as required when the MC is elevated 6 m (20 ft) into the OMEGA target chamber. The MCTC weighs about 1800 kg (4000 lb) and must be moved and precisely positioned at four process stations within the UR/LLE facility. These are the FTS, characterization station, prep station, and LP (target chamber). Four air casters are mounted under the vacuum chamber, and compressed air is used to float the MCTC on a thin cushion of air when it needs to be moved. Tooling balls are mounted to the MCTC which dock against locating surfaces when the cart is positioned at each process station.

Assembly of an MCTC (No. 1) was completed at GA. This unit was used during the MC cryogenic tests. UR/LLE provided a full control system for this unit. Figures 6–6 and 6–7 show the fully assembled MCTC.

A second MCTC (No. 2) was partially assembled at UR/LLE and was used at GA during the shroud pulling tests (Section 6.2.3). This unit was repeatedly positioned and docked with the LP successfully using the air caster/docking plate system.

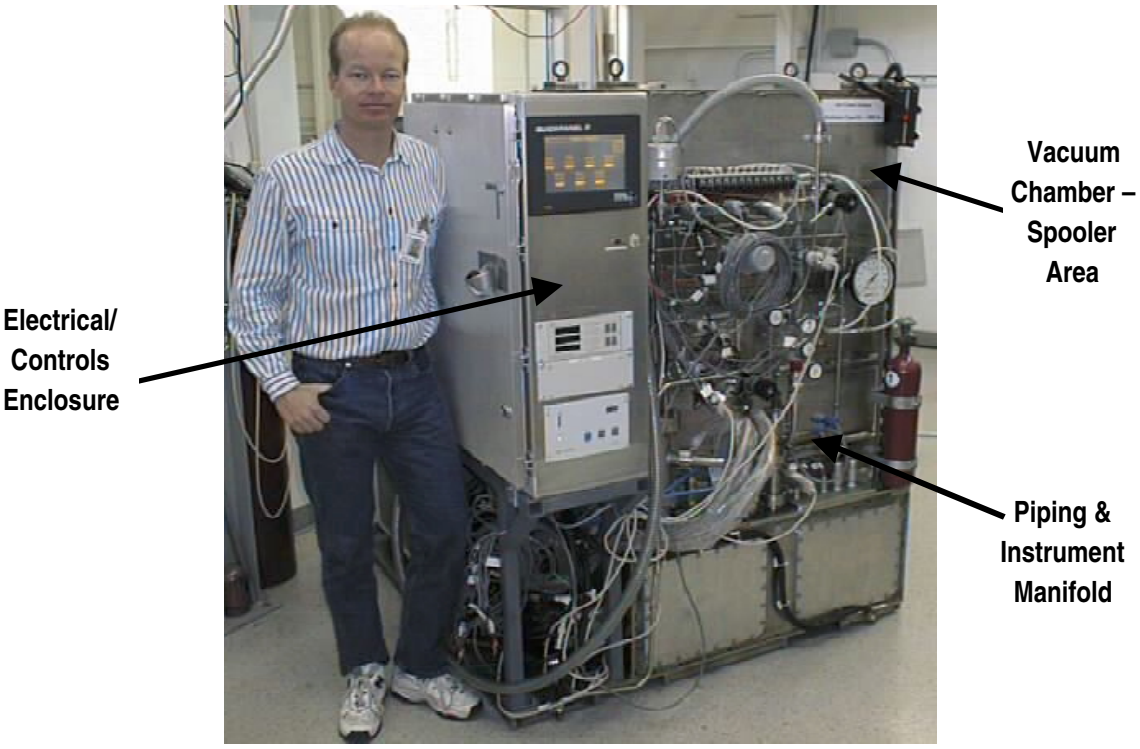

Fig. 6–6 MCTC — front view.

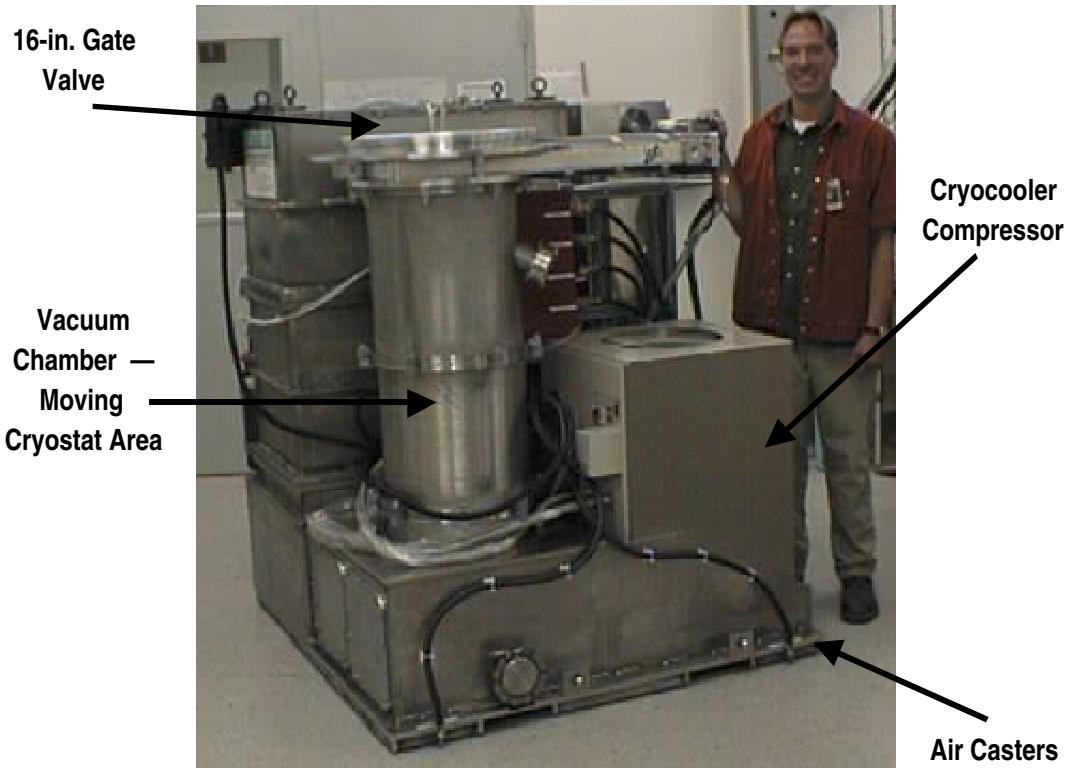

Fig. 6–7. MCTC — rear view.

6.2.3. Upper Pylon/Shroud Puller System

The UP consists of a linear motor, housing, vacuum feedthrough, and shroud gripper. Its function is to remove the MC's upper cooling shroud, exposing the target so that the laser's beams have unobstructed access to it. After the laser shot, the UP replaces the shroud onto the MC in the same location and orientation that it was in when it was removed.

The equipment that performs the shroud handling and cryostat transport functions was installed and tested at GA from March through May 1999. The test apparatus closely represented the OMEGA installation. UR/LLE provided much of the equipment that was used, including the LP, CL, ST, and MCTC No. 2. The LP provides the pathway for the MC to traverse from UR/LLE's La Cave to the target chamber center. At its lower end, it provides a flanged connection to the MCTC and an air-lock valve. At its upper end, it provides the primary positioning reference of the MC relative to the target chamber center. The CL is a vacuum chamber that contains a "push chain" drive made by Serapid Corp. This drive system is used to push the MC from its home position in the MCTC and elevate it to the top of the LP. The ST is a 3-m (10-ft) long cylindrical vacuum chamber. It simulates the OMEGA target chamber. The ST was equipped with a target viewing system and a high-speed camera capable of capturing 500 frames/s. Figures 6–8 and 6–9 show the equipment installation in the Bldg. 35 test facility. The entire installation was about 9 m (30 ft) tall. To provide a suitable environment for the equipment, enclosed rooms were built within Bldg. 35, and a climate control system was installed to provide temperature and humidity control.

During the test period, all system operational functions were repeatedly performed successfully. The MC was elevated from MCTC No. 2 into the LP and locked into place. The MC fine positioner was used to position the target. Video recordings of the target's motion during shroud removal and replacement events were made. The shroud pulling system was used to remove the MC's upper shroud at full speed and replace it. Twenty shroud retraction cycles were performed with a target in place. Numerous shroud retractions were also performed without a target. The target was never dislodged during the trials, and the cooling shrouds did not incur significant signs of wear. The ST, MCTC, and CL vacuum chambers were operated at 2×10^{-5} torr during the testing activity. All tests were performed with the MC at ambient temperature.

The testing activity concluded during early May 1999. The test apparatus was disassembled, and all equipment was shipped to UR/LLE on May 17.

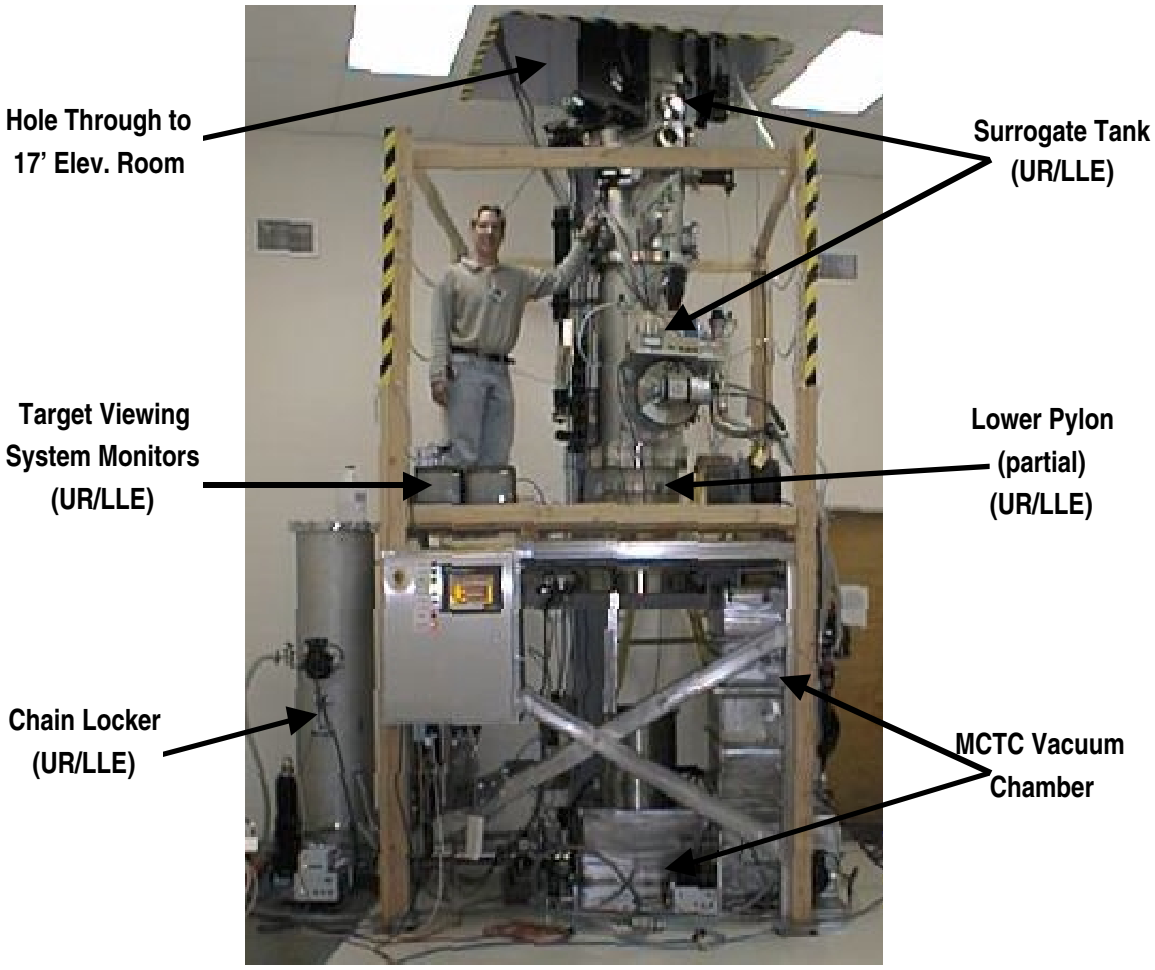

Fig. 6–8. Bldg. 35 shroud pulling test facility — ground floor.

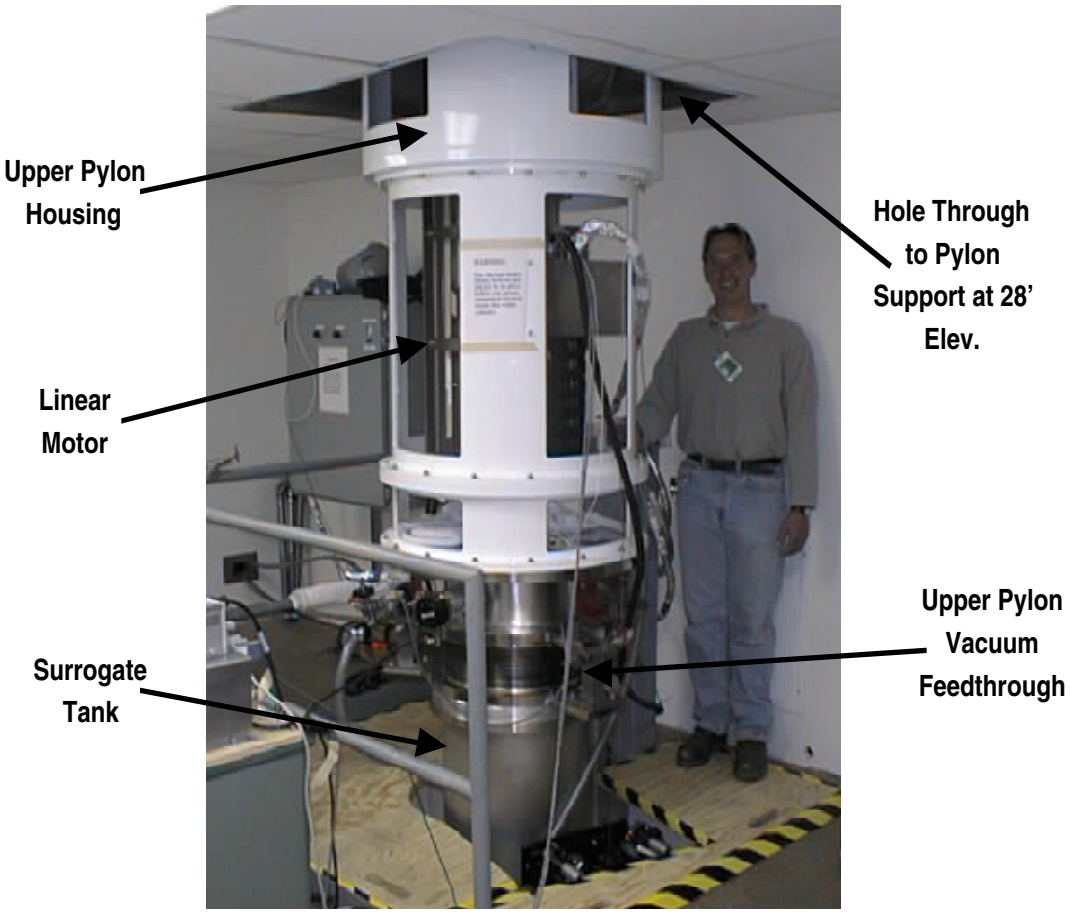

Fig. 6–9. Bldg. 35 shroud pulling test facility — 17-ft elev. room.

For further information, please contact K. Boline (GA).

7. PUBLICATIONS

Besenbruch, G.E., Alexander, N.B., Baugh, W.A., Bernat, T.P., Collins, R.P., Boline, K.K., Brown, L.C., Gibson, C.R., Goodin, D.T., Harding, D.R., Lund, L., Nobile, A., Schultz, K.R., and Stemke, R.W., "Design and Testing of Cryogenic Target Systems," to be published in Proc. Int. Conf. on Inertial Fusion Science and Applications, September 12–17, 1999, Bordeaux, France.

Bittner, D.N., Bernat, T.P., Burmann, J., Collins, G.W., Kozioziemski, B., Letts, S., Mapoles, E.R., Monsler, E., Pipes, J., Saculla, M., Sater, J.D., Unites, W., "Forming Uniform Deuterium Hydride and Deuterium-Tritium Layers in Shells," Lawrence Livermore National Laboratory Inertial Confinement Fusion Quarterly Report **8**, 131 (1998).

Bittner, D.N., Collins, G.W., Monsler, E., and Letts, S., "Forming Uniform HD Layers in Shells Using Infrared Radiation," Fusion Technology **35**, 244 (1999).

Cook, R.C., McEachern, R.L., Stephens, R.B., "Representative Surface Profile Power Spectra from Capsules Used in NOVA and OMEGA Implosion Experiments," Fusion Technology **35**, 224 (1999).

Elsner, F., "Thickness Distribution for Gold and Copper Electroformed Hohlraums," Fusion Technology **35**, 81 (1999).

Gibson, C.R., Alexander, N.B., Del Bene, J.V., Goodin, D.T., and Besenbruch, G.E., "Cryogenic Target System for Z-Pinch Machines," Cryogenic Engineering Conf. and Int. Cryogenic Materials Conf., July 1999, Montreal, Canada, and to be published in Advances in Cryogenic Engineering; General Atomics Report GA–A23188 (1999).

McQuillan, B.W., Elsner, F.H., Stephens, R.B., "The Use of $CaCl_2$ and Other Salts to Improve Surface Finish and Eliminate Vacuoles in ICF Microencapsulated Shells," Fusion Technology **35,** 198 (1999).

McQuillan, B.W., Greenwood, A., "Microencapsulation Process Factors which Influence the Sphericity of 1 mm O.D. Poly(-Methylstyrene) Shells for ICF," Fusion Technology **35,** 194 (1999).

Nikroo, A., Steinman, D.A., "Enlargement of Glass and Plastic Shells to 2 mm in Diameter by Redropping Through a Short Heated Tower," Fusion Technology **35**, 220 (1999).

Nikroo, A., Steinman, D.A., "Thin Sputtered Glass as a Permeation Barrier for Plasma Polymer Shells," Fusion Technology **35**, 212 (1999).

Nikroo, A., Woodhouse D., "Bounce Coating Induced Domes on Glow Discharge Polymer Coated Shells," Fusion Technology **35**, 202 (1999).

Olsen, R.E., Chandler, G.A., Derzon, M.S., Hebron, D.E., Lash, J.S., Leeper, R.J., Nash, T.J., Rochau, G.E., Sanford, T.W.L., Alexander, N.B., and Gibson, C.R., "Indirect-Drive ICF Target Concepts for the X-1 Z-Pinch Facility," Fusion Technology **35,** 260 (1999).

Sater, J., Kozioziemski, B., Collins, G.W., Mapoles, E.R., Pipes, J., Burmann, J., Bernat, T.P., "Cryogenic D-T Fuel Layers Formed in 1 mm Spheres by Beta-Layering," Fusion Technology **35**, 229 (1999).

Sheliak, J., Hoffer, J., "Surface Roughness Statistics and Temperature Step Stress Effects for D-T Solid Layers Equilibrated Inside a 2 mm Beryllium Torus," Fusion Technology **35**, 234 (1999).

Silke, G.W., Gibson, C.R., "Remote Handling of Cryogenic Targets for the OMEGA Laser System," to be published in Proc. 8th Int. Top. Mtg. on Robots and Remote Systems, American Nuclear Society, April 25–29, 1999, Pittsburgh, Pennsylvania; General Atomics Report GA–A23039 (1999).

Steinman, D.A., Nikroo, A., Woodhouse, D., "Strengthening Large Thin Glass Shells by Overcoating with GDP," Fusion Technology **35**, 216 (1999).